Experimental Characterization of Failure Mechanisms in Carbon Fiber Laminated Joints

Alastair M. Croxford

A dissertation
submitted in partial fulfillment of the
requirements for the degree of

Master of Science in Aeronautics & Astronautics

University of Washington

2017

Reading Committee:

Anthony Waas, Chair

Jinkyu Yang

Program Authorized to Offer Degree:
Aeronautics and Astronautics

University of Washington

Abstract

Experimental Characterization of Failure Mechanisms in Carbon Fiber Laminated Joints

Alastair M. Croxford

Chair of the Supervisory Committee:
Anthony Waas
Aeronautics and Astronautics

Experimental data for carbon fiber composite joints is presented along with the characterization of failure mechanisms. These failure mechanisms are observed in three sets of testing: (1) Simple Pin Loading, (2) Window tests (pin loading with transparent out-of-plane constraints), and (3) Double Shear Bolted Joint. The first two test setups involve a unique fixture that allows the collection of far-field strain visualization via Digital Image Correlation, providing a better understanding of the laminate's response to the load in real time. These results are subsequently compared to one another and work done in previous publications.

TABLE OF CONTENTS

Page

LIST OF FIGURES

LIST OF TABLES

Table Number Page

ACKNOWLEDGMENTS

First, I would like to thank my adviser, Professor Anthony Waas for welcoming me into his research group and allowing me to gain significant knowledge and experience in structural engineering and composites, both from him and his students and postdoctoral scholars. Second, I would like to thank Professor Jinkyu Yang for not only serving on my committee, but also for recommending me to Dr. Waas as a Graduate Research Student Assistant. Next, I would like to thank J. Sean Yeung for his endless help with all things CT scanning and my lab group members Jaspar, Solver, Paul, and Ashith for teaching me how to use various lab equipment and answering a multitude of theoretical questions. Finally, I would like to thank my family for all of their support and pushing me to succeed.

Chapter 1

INTRODUCTION

1.1 Introduction

The development of carbon fiber reinforced polymer (CFRP) composite materials has been the catalyst behind massive technological advancements in the aerospace industry. The material's high stiffness-to-weight and strength-to-weight ratios combined with the ability to tailor a part's performance to specific loads allows aircraft and spacecraft to lower their weights and maximize their capabilities. One of the biggest structural advantages of composites over metals is the ability to co-bond and co-cure individual parts, heavily reducing the need for mechanical fasteners. However, these bolts and rivets are still necessary in certain applications and the complex nature of composites can make it difficult to predict their interactions.

The purpose of this Masters thesis is to provide experimental data and the characterization of failure mechanisms in composite joints to aid in the future development of computational models. First, a simple pin loading test case is presented allowing us to focus on the isolated bearing response of the composite. Second, a transparent washer and window is used to apply an out-of-plane constraint to the composite around the pin. The transparencies enable us to see how the strain fields and failure mechanisms compare to the pin loading in real time. Finally, the third experimental test setup consists of a simplified, ASTM-Standard Double Shear Bolted Joint fixture. The use of an actual bolt and nut give us the ability to apply a specific torque and corresponding bolt pre-tension. All of this is preceded by a literature review of two publications used as primary references for my work.

1.2 Test Procedures and Specimen Dimensions

The carbon fiber composite used in these experiments is a 24 ply quasi-isotropic laminate with a layup of $[45/0/-45/90]_{3S}$. The material system used is IM7/8552 and the laminate had an average thickness of 0.178 in. The dimensions of all specimens used can be seen in Figure 1.1. All dimensions remained constant except for eccentricity of the hole. This dimension, E, is a scalar function of the diameter of the hole, D. This scalar value was set to 1.5 and 3.0 for all three test setups and added the cases 2.0 and 2.5 for the Double Shear Bolted Joint tests. All tests were performed at a quasi-static rate of 0.0004 in/sec, at room temperature and moisture levels, and with no pre-conditioning. The hydraulic grip pressure was set to 1500 psi; a pressure that neither crushed the specimens nor resulted in them slipping during any test performed.

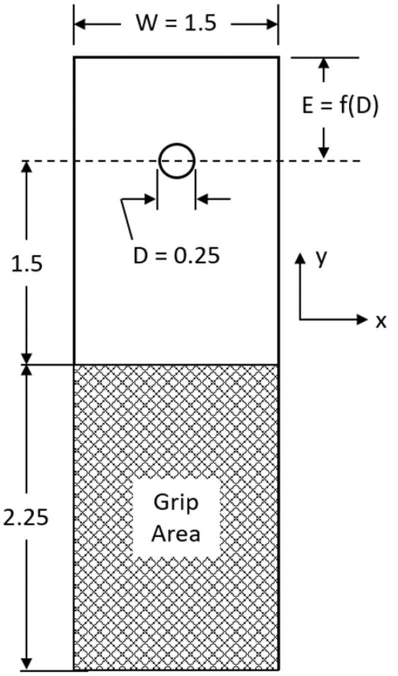

Figure 1.1: Diagram of test specimen. All units in inches. Distance from center of hole to edge of part, E, is a scalar function of the diameter of the hole, D.

1.3 Data Collected

The three forms of test data gathered and presented in this document are (1) load vs. displacement, (2) far-field strain plots, and (3) X-ray micro CT scans. For the first two items, Digital Image Correlation (DIC) is used to calculate displacements and visualize strains. Background information on DIC can be found in Appendix A. The load vs. displacement plots shown have had minor modifications made to better visualize the data. An explanation of how this data was processed can be found in Appendix B. Finally, the CT scans presented were done utilizing a NSI X5000 machine. Basic settings and setup for these scans can be found in Appendix C.

Chapter 2

LITERATURE REVIEW

This chapter will provide summaries of the two papers titling each section along with how certain pieces relate to the work presented in this document.

2.1 "Bolt-Bearing Fatigue of a Graphite/Epoxy Laminate" by John H. Crews Jr., July 1980, NASA

This particular document is a NASA Technical Memorandum written by John H. Crews, Jr., based out of NASA's Langley Research Center in Hampton, VA. The primary focus of his study was the effects of bolt clamp-up torque and water exposure on the bolt-bearing fatigue strength and life of a quasi-isotropic composite laminate. In the fatigue testing, specimens were cycled until failure with the hole elongation being monitored for the duration of the test. Static tests were also conducted to find a correlation between the strength and failure mode. The particular laminate used was a 16 ply specimen consisting of T300/5208 material.

Crews' work on static failures and clamp-up torques in this paper are the pieces most important to me and the work I am presenting in this document. In particular, his work creating the plot of Bearing Stress vs. Hole Elongation for several levels of clamp-up torque is what I based my test matrix and several of my plots on. This can be seen in Figure 2.1.

While Figure 2.1 only shows the bearing stress vs. hole elongation for four clamp-up torques, Crews ran these tests for an additional two clamp-up torques: 8.48 and 11.30 N-m. The bearing stresses seen at the onset of failure and at the ultimate strength for each clamp-up torque is shown in Figure 2.2.

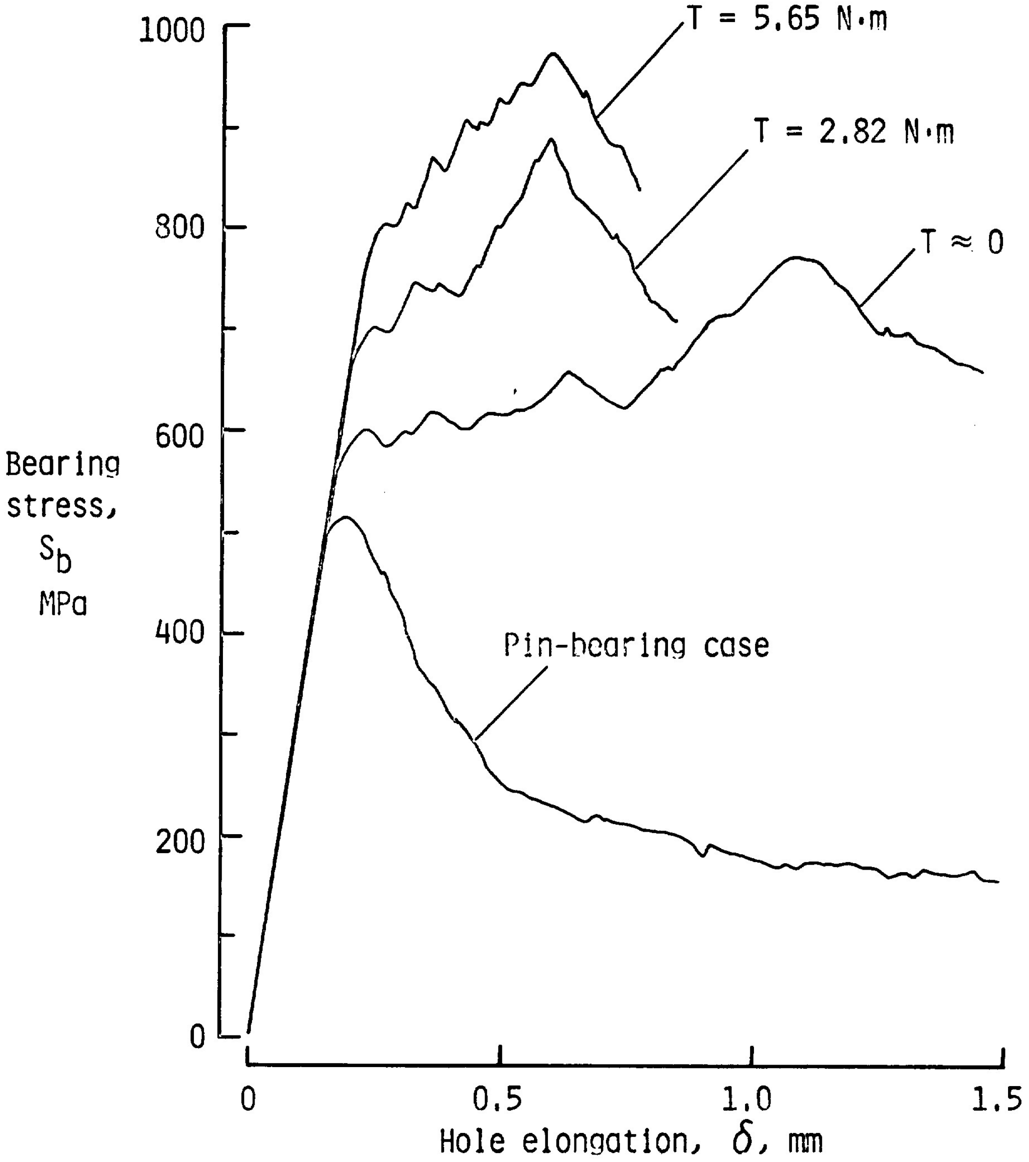

Figure 3.- Static hole elongation for several clampup conditions.

Figure 2.1: Figure 3 from Crews' NASA Tech. Memo. Static Bearing Stress (MPa) vs. Hole Elongation (mm) for four levels of clamp-up torque.

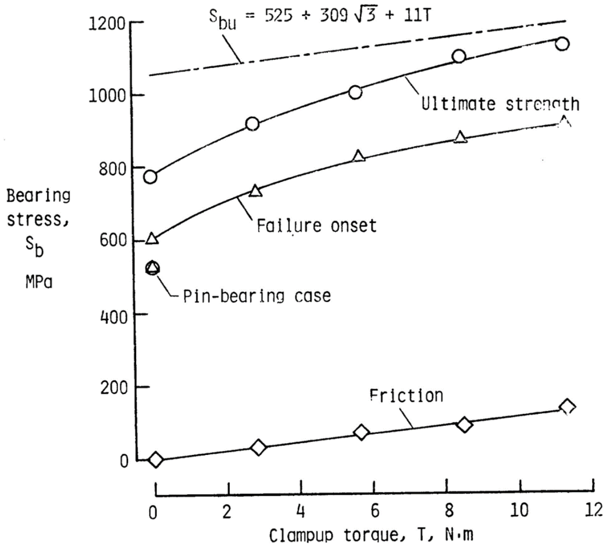

Figure 5.- Static bearing strength for range of clampup torque.

Figure 2.2: Figure 5 from Crews' NASA Tech. Memo. Bearing Stress vs. Clamp-Up Torque, specifying stresses onset of failure and the ultimate strength.

In place of altering the bolt clamp-up torques in the Double Shear Bolted Joint tests, I elected to adjust the eccentricity of the hole, or the distance from the center of the hole to the edge of the specimen for a single clamp-up torque. While Crews left this distance as four times the diameter of the hole, I used 1.5, 2.0, 2.5, and 3.0. As for the pin bearing case (no clamp-up) and $T \approx 0$ case, I designed a separate fixture to enable far-field strain measurements to be taken. This work can be seen in Chapters 3 and 4.

Because of Crews' method of measuring the hole elongation - a method that involves a stiff wire and slotted washers and a slotted bolt - along with specimen differences (dimensional and material), a direct comparison to his data is not possible. However, the failure modes and experiment trends observed can be compared; these comparisons are made in the following chapters.

2.2 *“Bearing Strength and Failure Behavior of Bolted Composite Joints (Part I: Experimental Investigation)” by Yi Xiao and Takashi Ishikawa, 2005*

This document was published by “Composites Science and Technology” in 2005 and is authored by Yi Xiao (correspoding author) and Takashi Ishikawa. The primary purpose this publication was to evaluate the effect of resin properties in a composite laminate on the bearing strength and failure mechanics of a double shear bolted joint. In order to do this, two different material systems were chosen: IM-7/PIXA, a graphite-polyimide, and IM600/Q133, a toughened graphite-epoxy. Both materials were fabricated into 16 ply quasi-isotropic laminates of nearly identical thicknesses (2.24 vs. 2.30 mm). While the mechanical properties of these two materials are very similar, the DCB fracture toughness of the IM-7/PIXA is more that four times greater than the IM600/Q133 (1400 vs 336.8 J/m^2).

While the fixture used by Xiao is very similar to the one I used in Chapter 5, there are a couple of important dimensional differences to note. Xiao uses a width-diameter ratio equal to eight ($W/D = 8$) and a bolt diameter of 4.8 mm - equivalent to a #10 fastener, 0.190 in. He does, however, use an eccentricity covered in my testing, $E = 3.0D$, allowing for easier comparison. Post-test analysis shown in this document include X-ray radiographs and Scanning Electron Microscope (SEM) photographs. These results are placed alongside mine for comparison in Chapter 5. Final conclusions by Xiao include (1) “through-thickness shear cracks and large-scale delamination are the major cause of final fracture” and (2) “toughness exerts remarkable influence on control of the damage mechanism.” The composite specimens with the PIXA matrix are much less susceptible to matrix cracking and delaminations due to the DCB fracture toughness noted earlier.

Chapter 3

SIMPLE PIN LOADING

3.1 Fixture Design and Test Setup

3.1.1 Original Fixture

Initially, this testing needed to be performed to aid in the validation of a computational model being constructed by students in Professor Waas's lab group. Because of a desire for quick results, an old fixture was modified to meet our needs. This fixture, with the modifications made, can be seen in Figure 3.1. When discovered, this fixture had three perpendicular walls welded together on a base plate. A cross brace was added (green rectangle in CAD model) with a semi-circular groove and hole was drilled in the back wall, aligned with the groove. These feature supported the pin.

There were several issues with this fixture, however the most obvious and most important one is the distinct difference in stiffness at the pin's reaction points. The cross brace in the front has a much lower stiffness than the solid wall, resulting in the pin no longer being perpendicular to the loading direction. This uneven loading will not provide an accurate representation of the specimen's bearing strength.

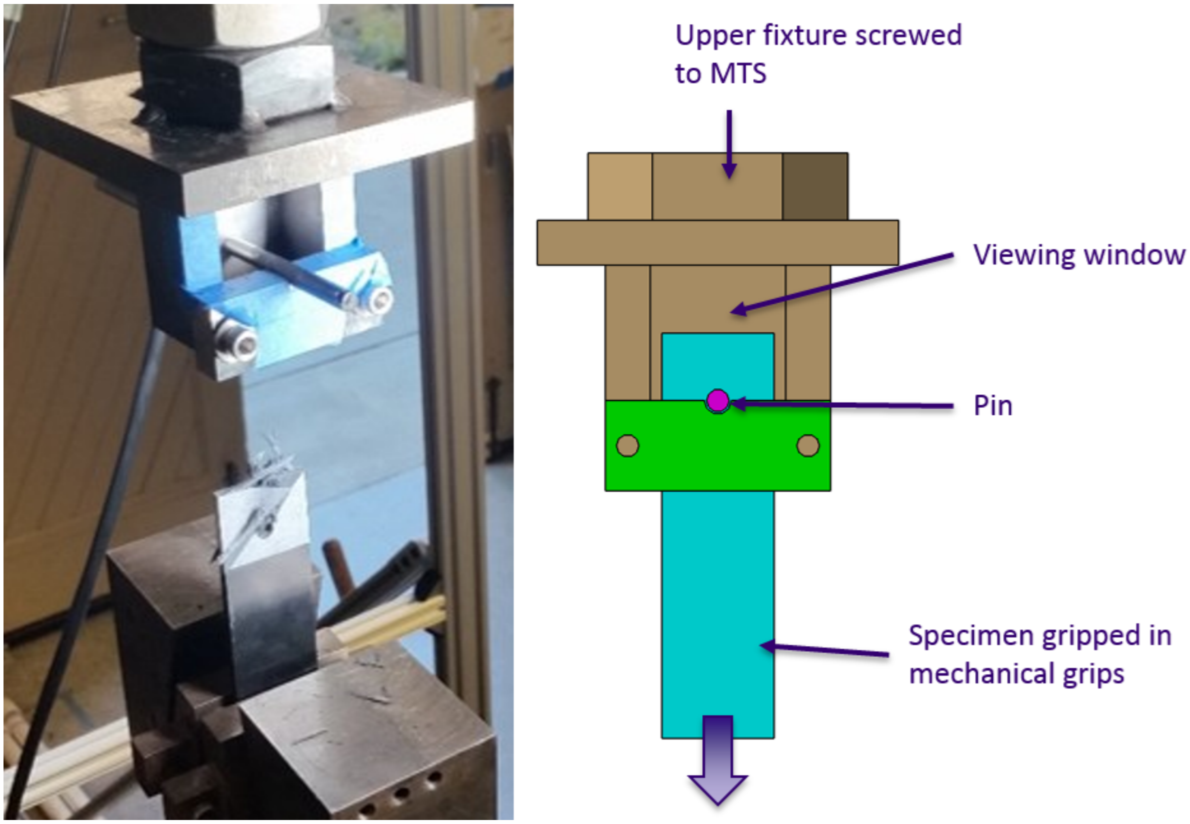

Figure 3.1: Original fixture design. Left image: Actual attached to MTS load frame. Right image: CAD model.

3.1.2 New Fixture Design

When redesigning this fixture, it was very important to fix the primary issue from the original fixture; this new design needed to be symmetrical. Figure 3.2 shows the actual fixture loaded into the testing frame on the left and a CAD drawing of the fixture on the right. The fixture consists of a thick, center tab that is clamped in the upper hydraulic grip of the testing frame and two identical, removable plates containing a viewing window. The plates are removable for several reasons: (1) Separate parts are easier to manufacture, (2) being able to remove the plates aides in the loading and unloading of the each specimen, and (3) transparent windows can be added underneath the plates to provide an out-of-plane constraint (Window tests, covered in the following chapter).

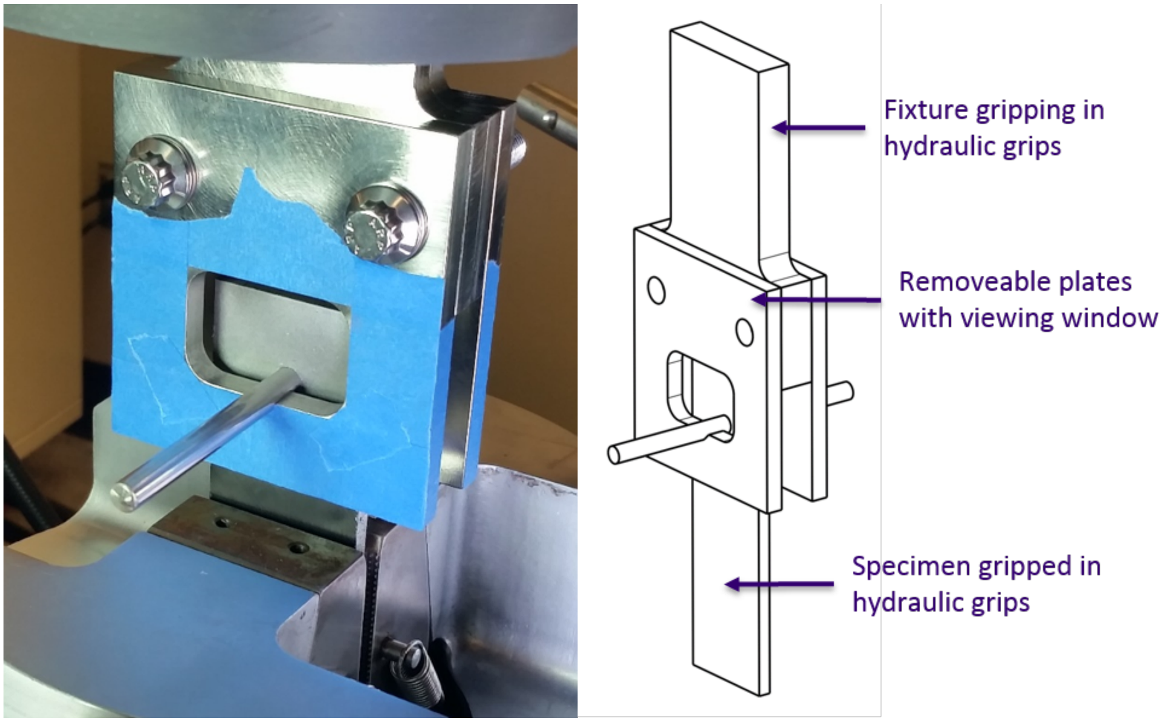

Figure 3.2: Redesigned fixture

3.1.3 Test Setup

The test setup for the Simple Pin Loading test uses two cameras to simultaneously capture DIC images. One camera collects images of the area around the hole while the other tracks the displacement of the specimen. The setup used for the tests covered in this document can be seen in Figure 3.3. The left camera provides a high resolution close-up of the fine speckle pattern painted around the hole as seen in the upper picture of Figure 3.4. This fine speckle pattern was painted with an Iwata-Medea brand airbrush and allows for higher fidelity in the DIC strain plots than can be obtained using a standard spray paint can. The right camera seen in Figure 3.3 is collecting images of the side of the fixture and specimen by way of a mirror reflection. The resulting images can be seen in the lower picture of Figure 3.4. The speckle patterns seen here were painted with standard spray paint as they are simply being used to track the displacement of the specimen. One point is chosen on the specimen and another on the block attached to the fixture. The difference in vertical (y) displacement is calculated and used in the Load vs. Displacement curves seen in the following sections.

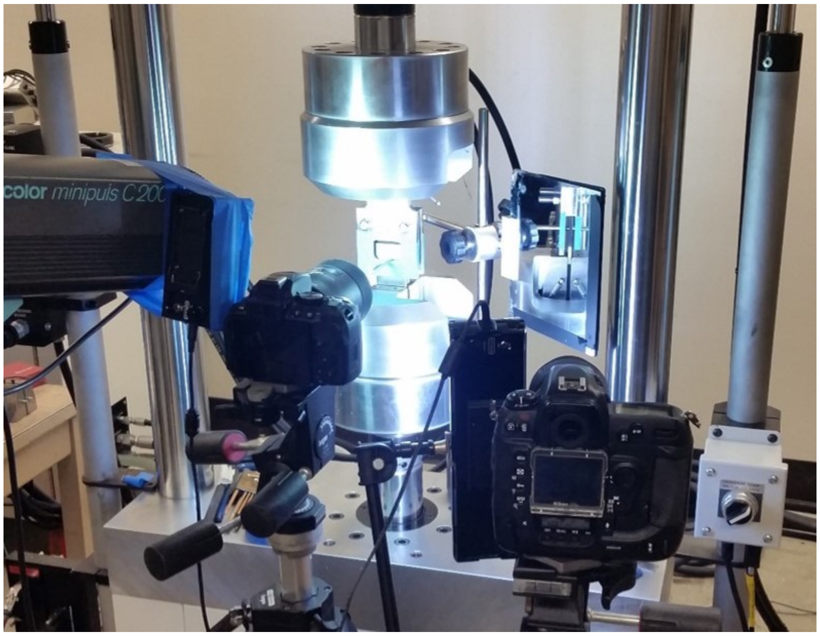

Figure 3.3: Setup of the Simple Pin Loading tests including camera locations.

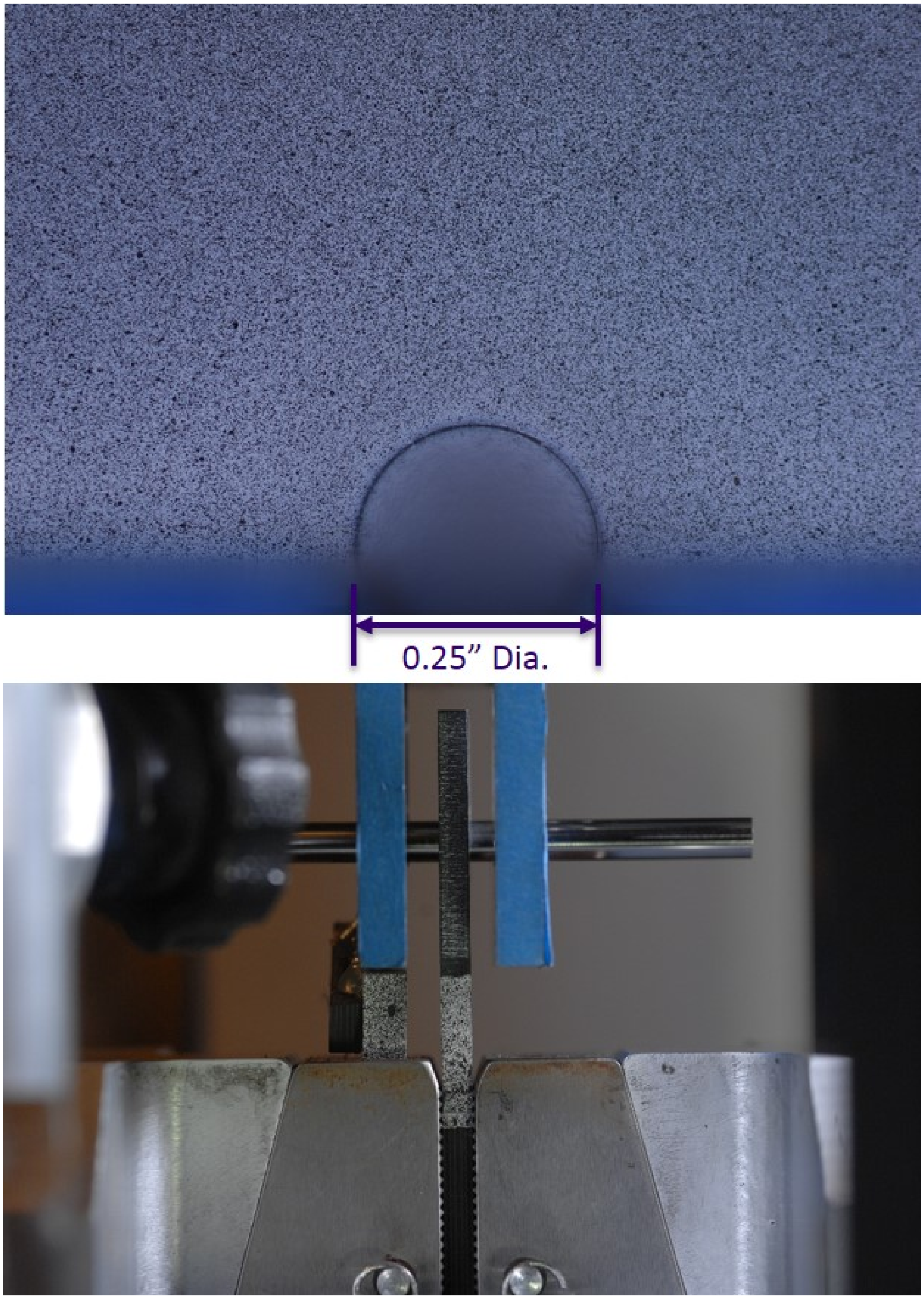

Figure 3.4: Raw images taken from the two cameras seen in Figure 3.3. Top image: Front facing camera. Bottom image: Side facing camera via the mirror reflection.

3.2 E = 1.5D, 17-4PH Pin

Initially, this testing was conducted using a 17-4PH Stainless Steel pin. This material was chosen for its availability and its relatively high yield strength (145 ksi). The load vs. displacement curves seen in Figure 3.5 and Figure 3.6 in the following subsection closely resemble Crews' Figure 3 plot for the pin-bearing case. [2]

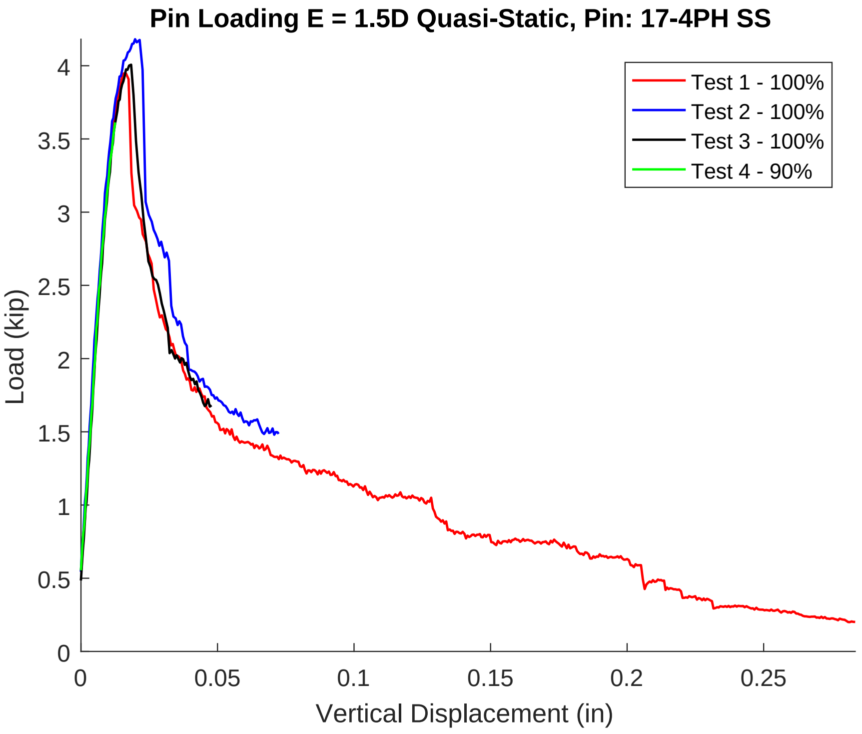

Figure 3.5: Simple Pin Loading, E = 1.5D, Pin: 17-4PH Stainless Steel.

3.3 E = 3.0D, 17-4PH Pin

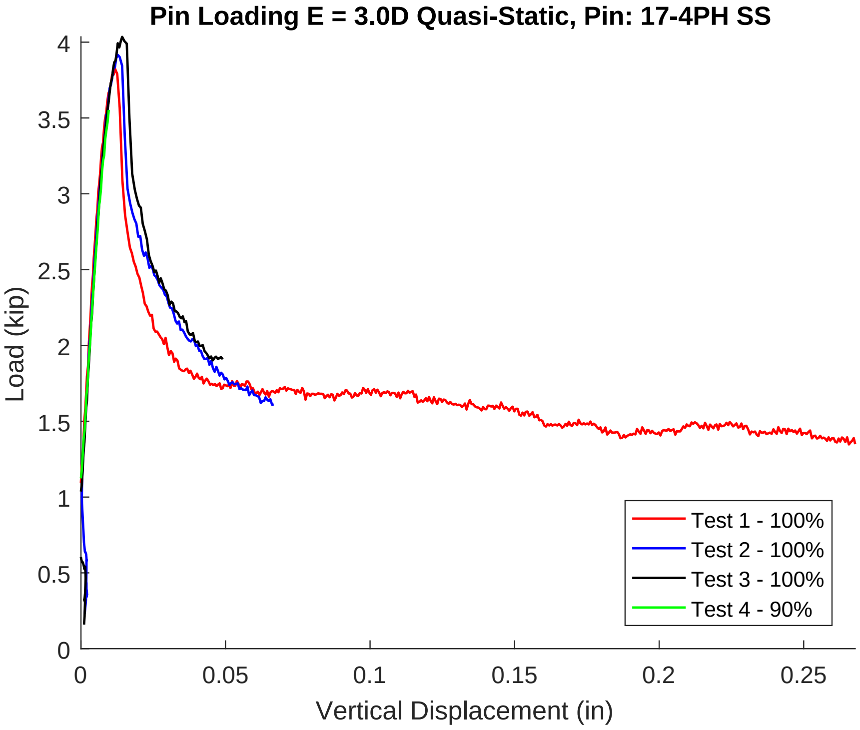

Figure 3.6: Simple Pin Loading, E = 3.0D, Pin: 17-4PH Stainless Steel.

3.4 Changing of the Pin Material

After the completion of each test in the previous two sections, slight yielding was observed in the 17-4PH Stainless Steel pins. It was initially decided that this problem was going to be accepted as just part of the test. The bending stress seen with this setup was quite high for a 1/4” pin to handle. However, as explained in the following chapter, the 17-4PH pin would not perform well enough in the Window tests and a stiffer Hardened Stainless Steel pin was acquired. All of the Simple Pin Loading tests were repeated with the new pin and their results can be seen in the following two sections.

3.5 E = 1.5D, Hardened Stainless Steel Pin

3.5.1 Test Results

Figure 3.7 shows the load vs. displacement curve for this test. As with Crews' paper and the previous tests using the softer pin, there is a single peak followed by a gradual decrease in load-carrying ability. This behavior indicates a pin bearing failure; these failures can be seen clearly in Figure 3.8. Each image shows the damage induced on the specimen after it has been unloaded and removed from the fixture. The label on each image indicates which curve in Figure 3.7 it corresponds to.

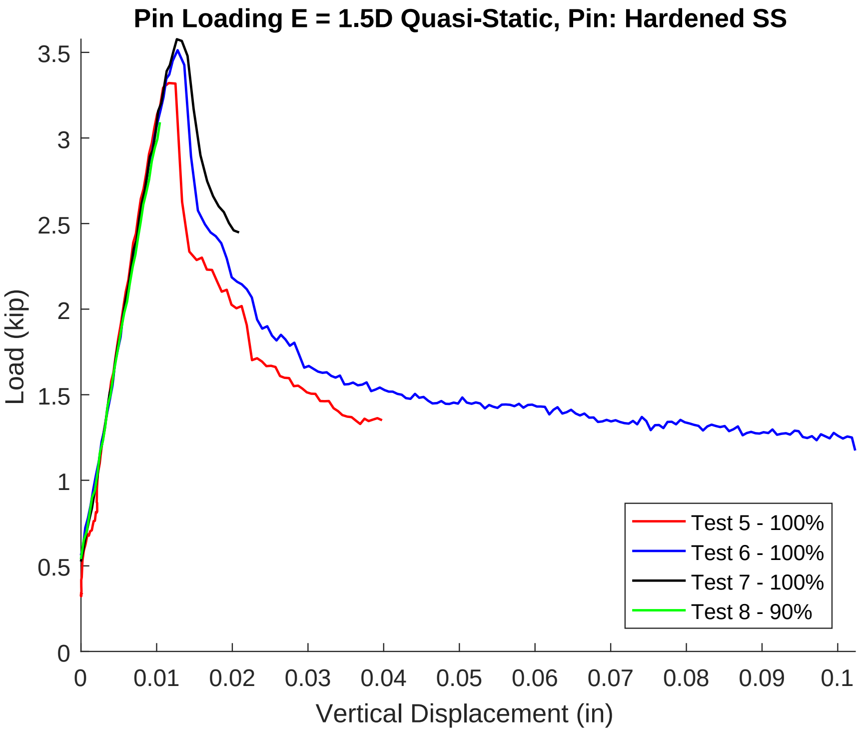

Figure 3.7: Simple Pin Loading, E = 1.5D, Pin: Hardened Stainless Steel.

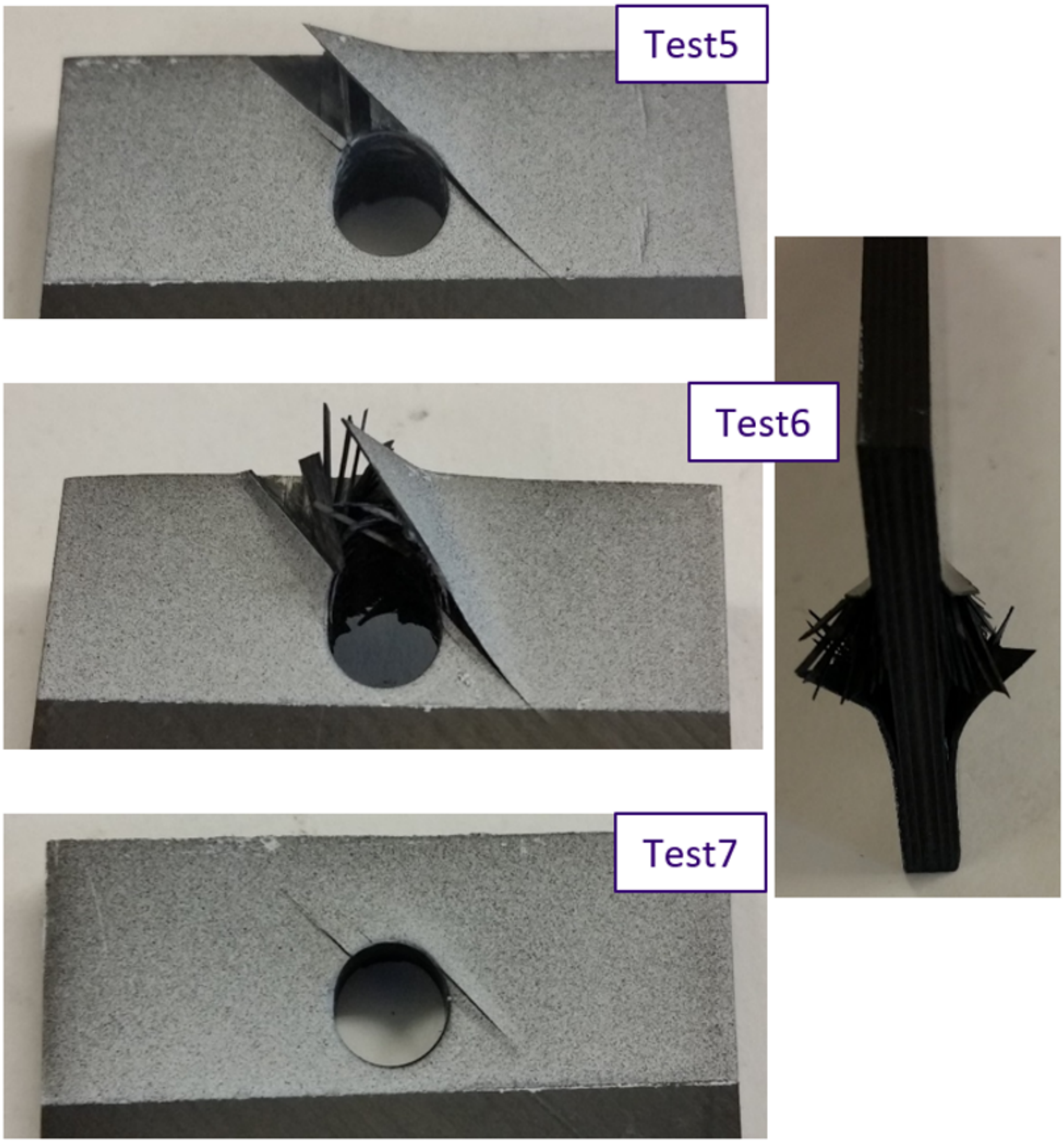

Figure 3.8: Post-test damage for the tests shown in Figure 3.7.

3.5.2 DIC

Figure 3.9 shows DIC strain plots for the normal strain in the loading direction, ε_{YY}, at distinct moments along with their locations on the load curve. At point A, just prior to the peak, a compression, ”cold” spot has formed at the top of the hole; this is indicated by the blue color. At point B, as the load plateaus slightly, this compression spot has grown and two red features have become more prominent. These red features indicate tension or elongation occurring. The the thin line to the left at a 45 degree angle, perpendicular to the hole is indicating matrix cracking or splitting between the fibers; these fibers are beginning to broom out of plane. The red area to the right of the hole is also at a 45 degree angle, but tangent to the hole. The fibers in the top half of this zone are beginning to broom outwards and upwards while the bottom half resists. At point C, these features have all expanded. Finally, point D is after the initial load drop. There are now two distinct cracks on the left side and a large uncolored portion in the center. This lack of color occurs because the DIC calculation has failed due to the material having come too far out-of-plane. This is another sign of brooming and a bearing failure.

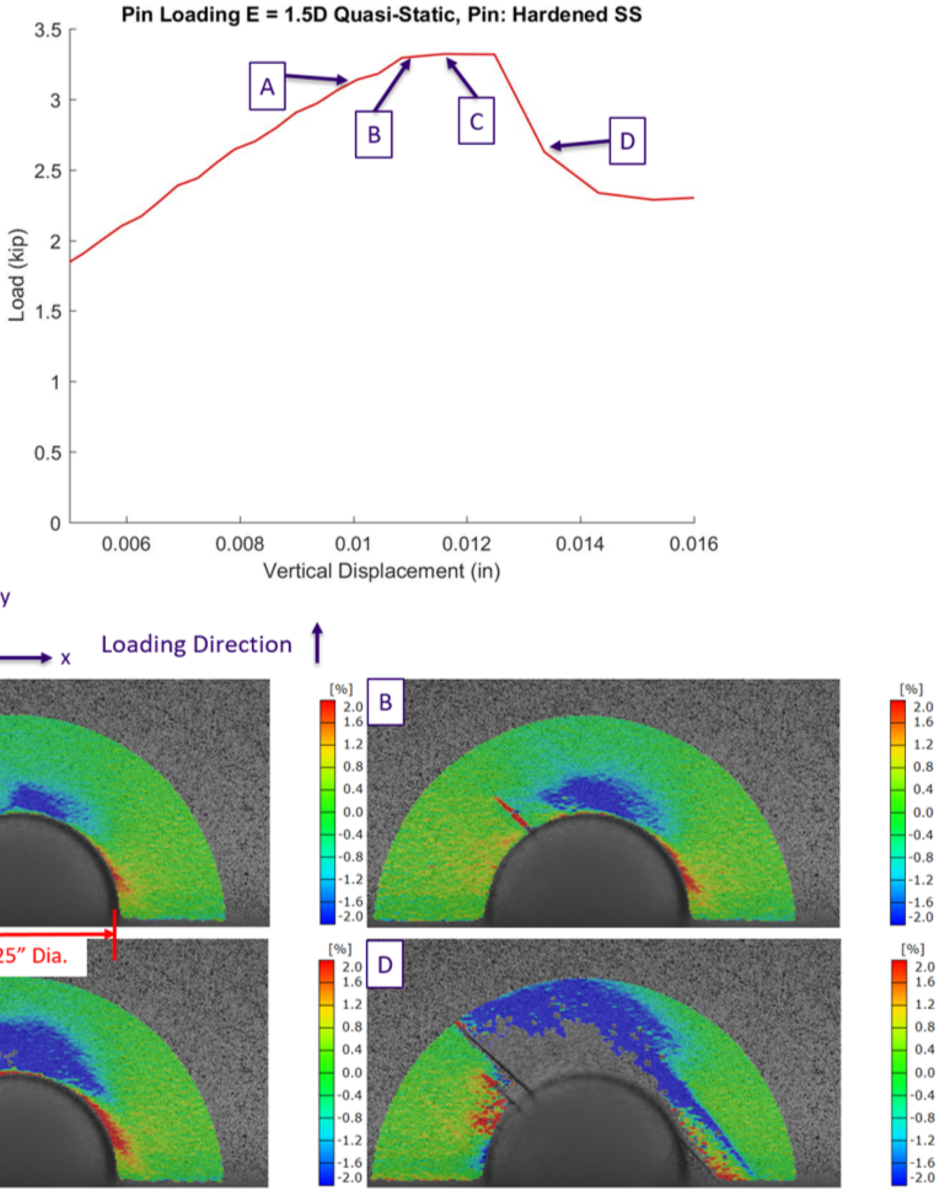

Figure 3.9: ε_{YY} DIC Strain Plots for Test 5. Peak region shown.

3.5.3 CT Scans

Figures 3.10 through 3.13 show CT images of Test 7. Figure 3.10 shows the CT scan form of what is seen in DIC in 2D and 3D along with an overlay of the post-testing damage image. Figure 3.11 shows 2D ”slices” of plies 2 and 3, the first -45 and 0 plies in the laminate. Because of the out-of-plane damage, some slices are showing failure in multiple directions. The large black spots often found bridging these different directions are delaminations between plies. Figure 3.12 shows the slice containing plies 3 and 4 and the slice at the center of the laminate. Figure 3.13 shows side slices, at the center and just inside the left and right edge of the hole. The brooming and consequential delaminations is very apparent in these images. Figure 3.14 shows the CT images of Test 8, the test taken to 90% of the peak load. Very minor matrix cracking is seen only in the outer plies.

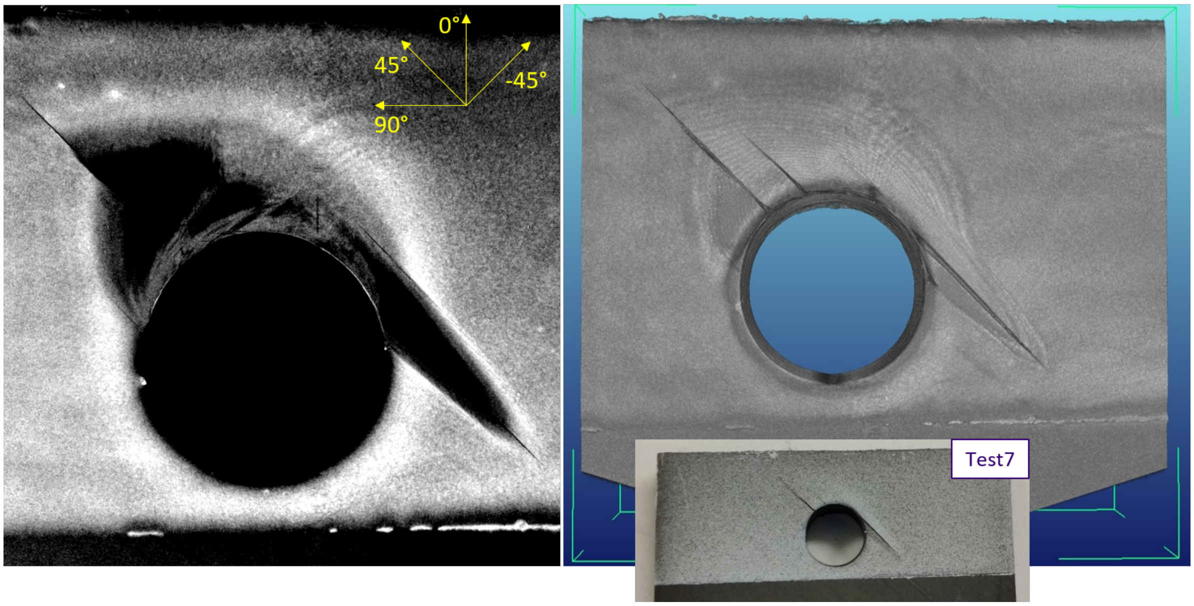

Figure 3.10: CT scan of Test 7. Left: 2D slice of ply 1. Right: 3D rendering of scanned area with overlay of image after testing.

Ply	1	2	3	4	5	6	7	8	9	10	11	12	13	14	15	16	17	18	19	20	21	22	23	24
Orien.	45°	0°	-45°	90°	45°	0°	-45°	90°	45°	0°	-45°	90°	90°	-45°	0°	45°	90°	-45°	0°	45°	90°	-45°	0°	45°

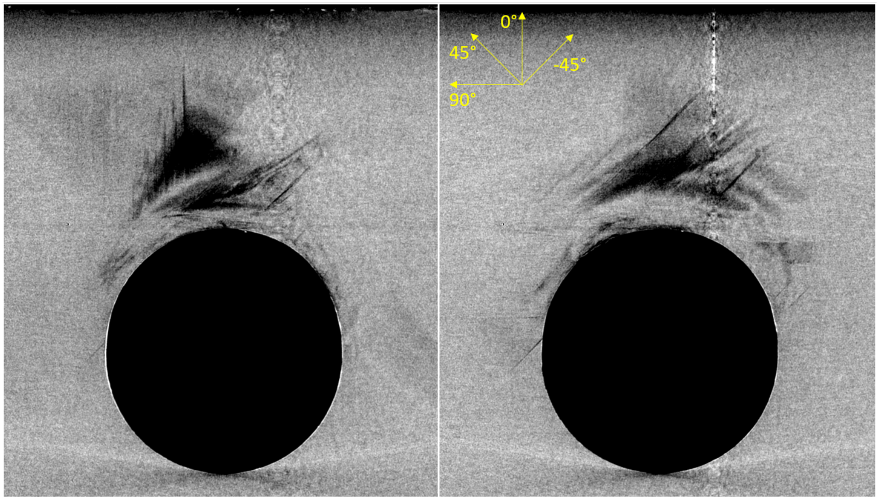

Figure 3.11: CT scan of Test 7. Left: Plies 2 and 3. Matrix cracking in 0 can be seen left of center, towards top. Matrix cracking in -45 can be seen right of center, closer to hole. Right: Ply 3, cracking in -45.

Ply	1	2	3	4	5	6	7	8	9	10	11	12	13	14	15	16	17	18	19	20	21	22	23	24
Orien.	45°	0°	-45°	90°	45°	0°	-45°	90°	45°	0°	-45°	90°	90°	-45°	0°	45°	90°	-45°	0°	45°	90°	-45°	0°	45°

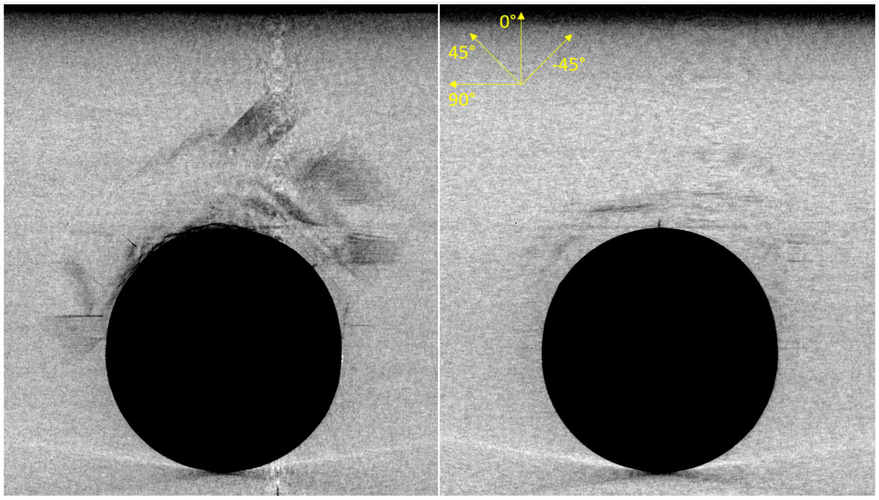

Figure 3.12: CT scan of Test 7. Left: Plies 3 and 4. Fiber cracking in -45, top-left of hole. Matrix cracking in 90, left (very clear) and right. Right: Plies 12 and 13, center of the laminate. Fiber cracking at top-center of hole.

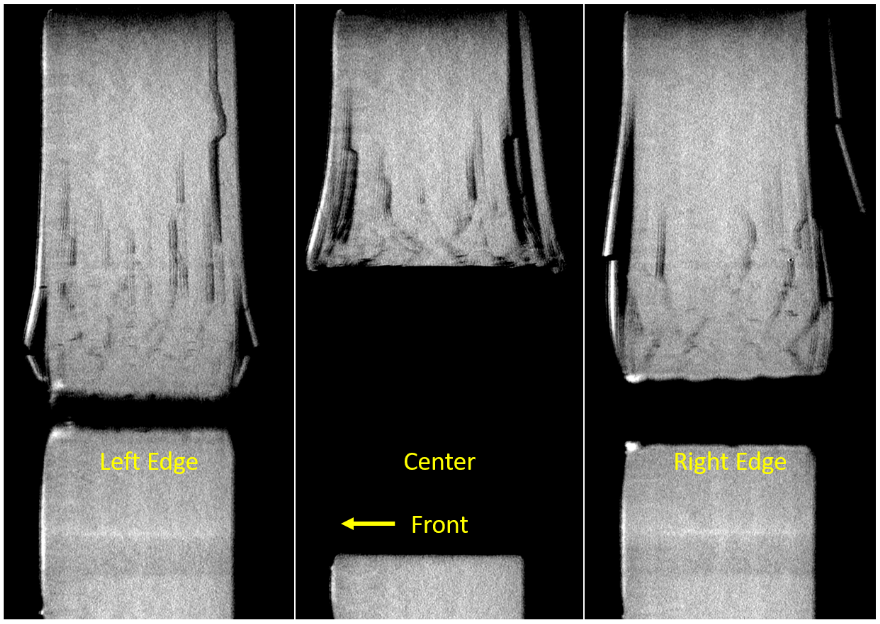

Figure 3.13: CT scan of Test 7. Side slices, loading direction: up. Brooming clearly seen in center image with damage clear in both outer images.

Ply	1	2	3	4	5	6	7	8	9	10	11	12	13	14	15	16	17	18	19	20	21	22	23	24
Orien.	45°	0°	-45°	90°	45°	0°	-45°	90°	45°	0°	-45°	90°	90°	-45°	0°	45°	90°	-45°	0°	45°	90°	-45°	0°	45°

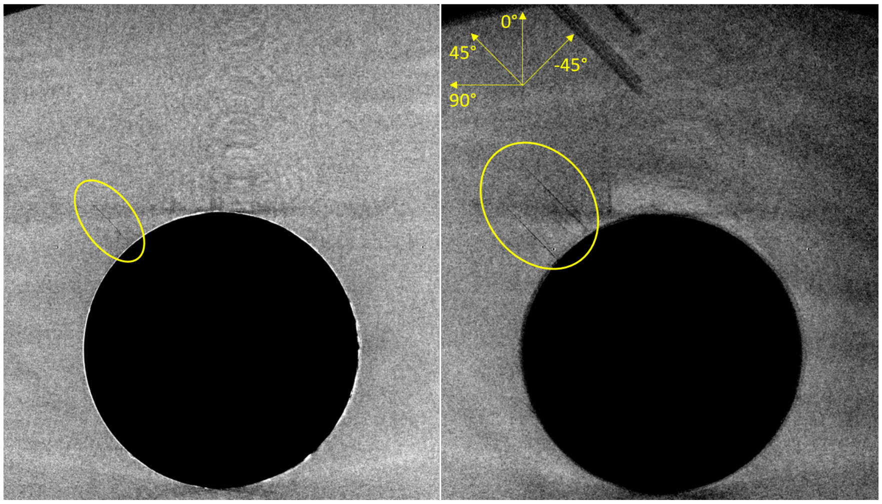

Figure 3.14: CT scan of Test 8. Left: Ply 1 shows minor matrix cracking along fiber direction, perpendicular to hole. Right: Ply 24 also shows minor matrix cracking, perpendicular to hole.

3.6 E = 3.0D, Hardened Stainless Steel Pin

3.6.1 Test Results

Figure 3.15 shows the load vs. displacement curve for this test case. The post-test damage images can be seen Figure 3.16. The results of this testing are nearly identical to the $E = 1.5D$ case.

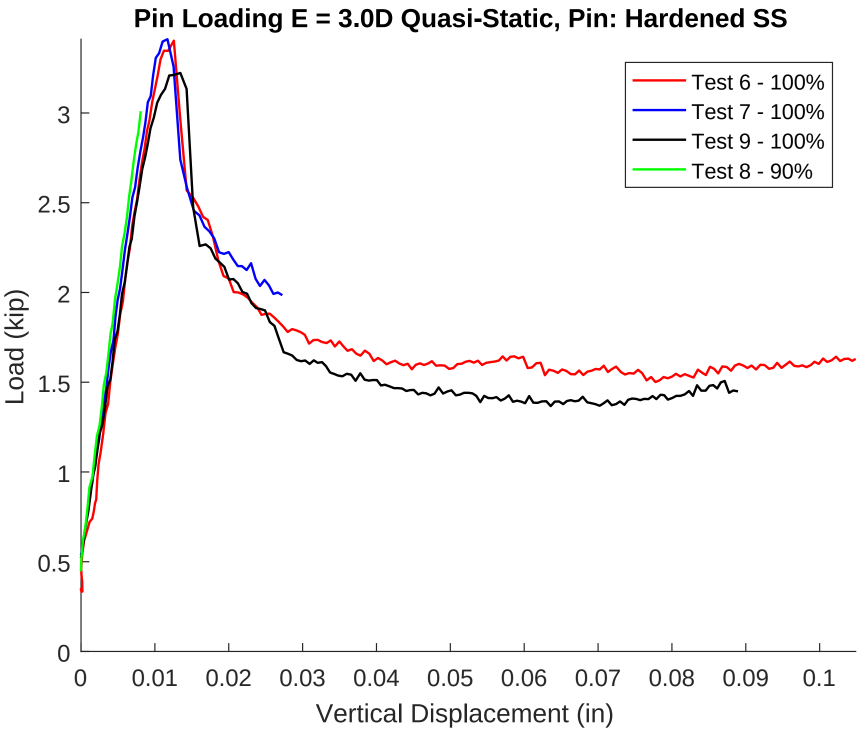

Figure 3.15: Simple Pin Loading, E = 3.0D, Pin: Hardened Stainless Steel.

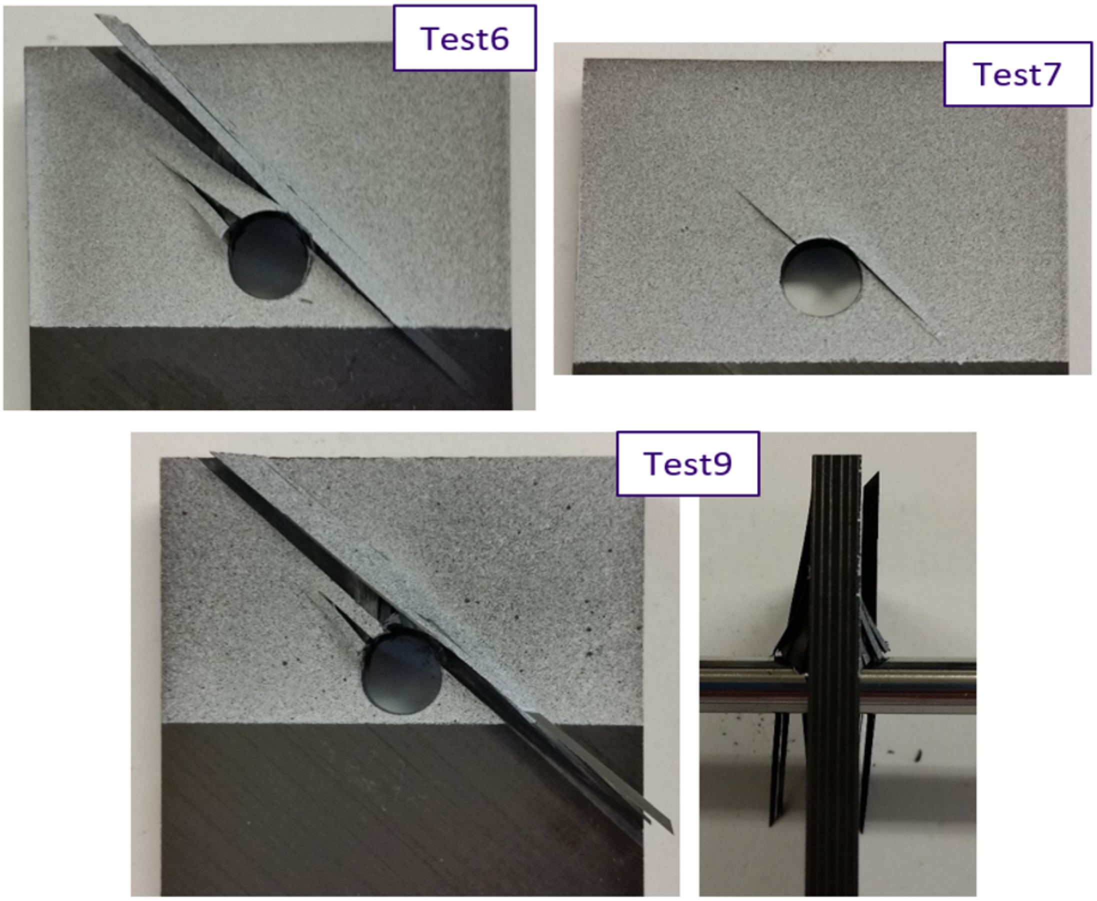

Figure 3.16: Post-test damage for the tests shown in Figure 3.15.

3.6.2 DIC

Figure 3.17 shows DIC strain plots for the normal strain in the loading direction, ε_{YY}, at distinct moments along with their locations on the load curve. These results are nearly identical as well to the $E = 1.5D$ case.

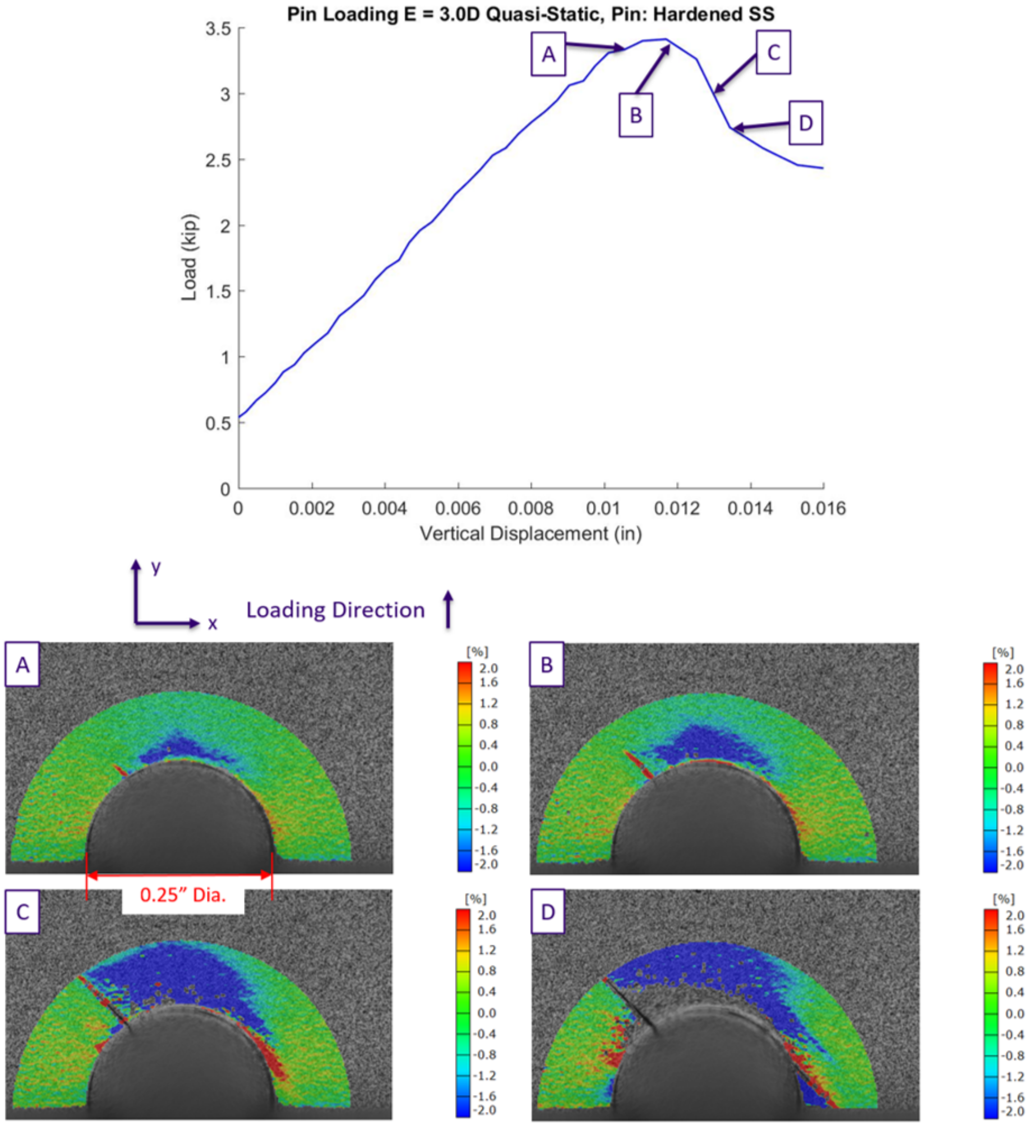

Figure 3.17: ε_{YY} DIC Strain Plots for Test 7. Peak region shown.

3.6.3 CT Scans

Figures 3.18 through 3.20 show CT images of test 7. Figure 3.18 shows slices through plies 1 and 2 and plies 2 and 3. Heavy out-of-plane deformation can be observed in both. Figure 3.19 shows slices through plies 4 and 5 and in the center of the laminate. Clear matrix cracking in the 90 plies is seen in both. Figure 3.20 shows side slices, at the center and just inside the left and right edge of the hole. As with the $E = 1.5D$ case, the brooming and consequential delaminations is very apparent.

Ply	1	2	3	4	5	6	7	8	9	10	11	12	13	14	15	16	17	18	19	20	21	22	23	24
Orien.	45°	0°	-45°	90°	45°	0°	-45°	90°	45°	0°	-45°	90°	90°	-45°	0°	45°	90°	-45°	0°	45°	90°	-45°	0°	45°

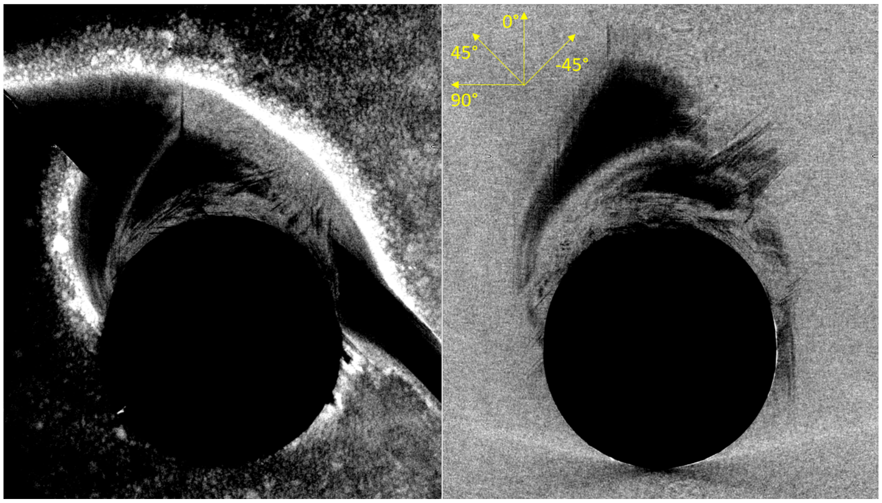

Figure 3.18: CT scan of Test 7. Left: Plies 1 and 2. To the edges, the 45 can be seen failing, while there is matrix cracking in the 0, above the hole, left of center. Right: Plies 2 and 3. Slight matrix cracking in the zero at the top of the image and to the right side of the hole. Matrix cracking in the -45 above the hole, right of center.

Ply	1	2	3	4	5	6	7	8	9	10	11	12	13	14	15	16	17	18	19	20	21	22	23	24
Orien.	45°	0°	-45°	90°	45°	0°	-45°	90°	45°	0°	-45°	90°	90°	-45°	0°	45°	90°	-45°	0°	45°	90°	-45°	0°	45°

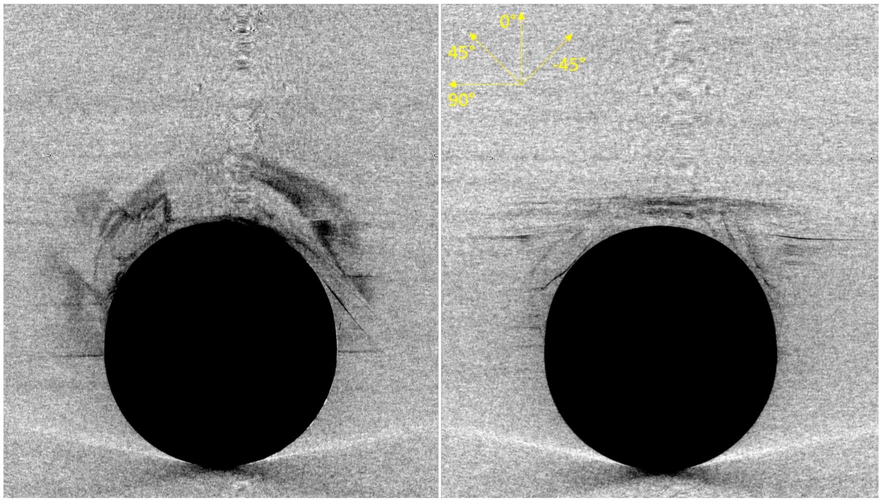

Figure 3.19: CT scan of Test 7. Left: Plies 4 and 5. Matrix cracking in the 90 to the left and right of hole. Matrix cracking in 45 upper left and right of hole, perpendicular to hole and tangent to hole, respectively. Right: Plies 12 and 13. Matrix cracking in 90, likely crushing at top of hole.

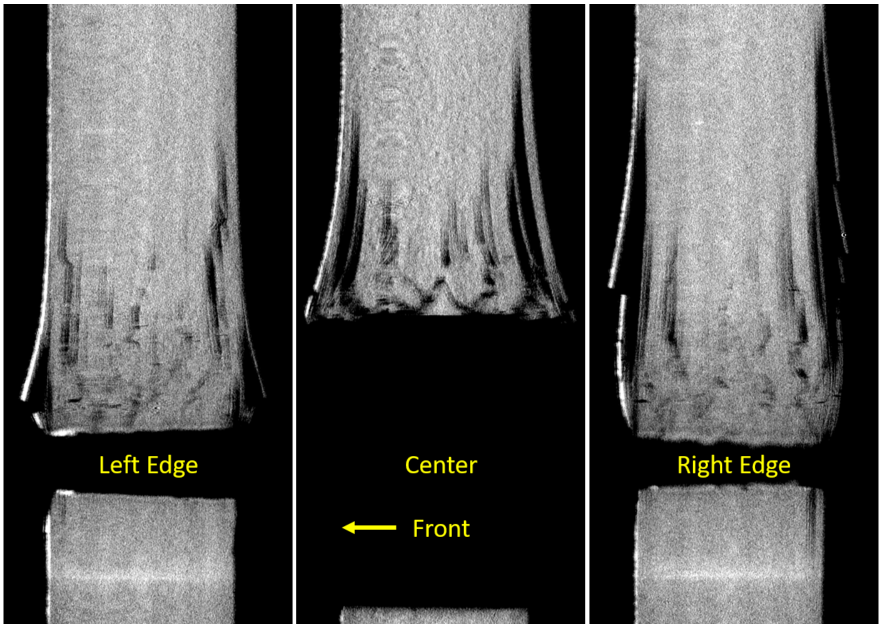

Figure 3.20: CT scan of Test 7. Side slices, loading direction: up. Brooming clearly seen in center image with damage clear in both outer images.

3.7 Comparison of Pins and Eccentricities

Upon switching to the stiffer pin, the peak loads seen in the second set of tests were noticeably lower than the original tests. The original, softer pin deflected more and absorbed more of the load, whereas the stiffer pin forces more of the load into the composite specimen, causing the joint to fail at a lower load. Figure 3.21 shows a comparison of the load vs. displacement curves, organized by pin material. The 17-4PH curves have more pronounced rounded curve before the peak due to the pin yielding, while the HSS curves are much more linear.

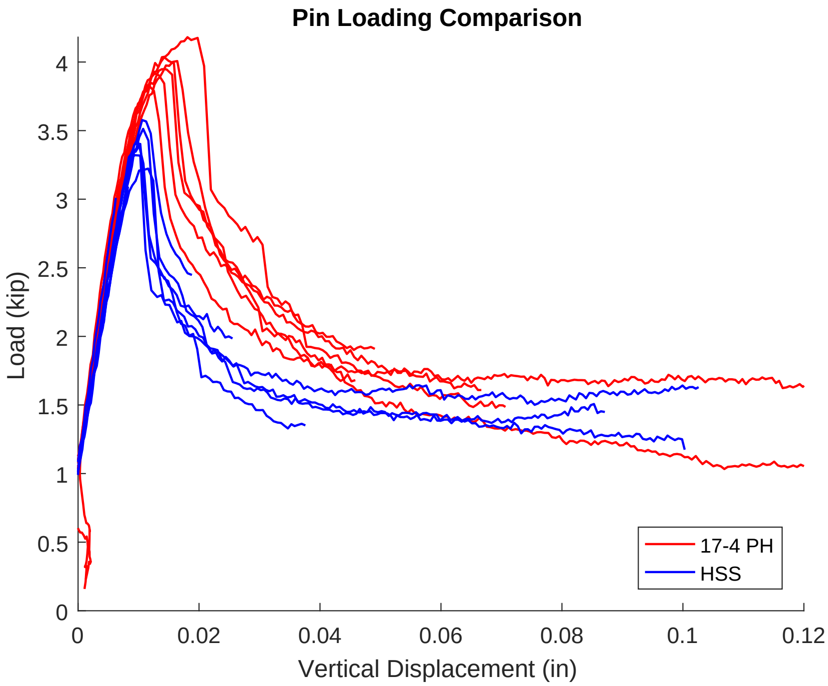

Figure 3.21: Comparison of pin material in Simple Pin Loading.

Table 3.1 tabulates the peak values reached for each test. The change in pin material causes a 14.5% drop in the average failure (100%) loads. This table also shows how the eccentricity of the specimen has no effect on the failure load. Figure 3.22 displays this visually by comparing the eccentricities for the Hardened Stainless Steel pin.

	17-4 PH		HSS	
	3.0D	**1.5D**	**3.0D**	**1.5D**
100%	3.82	3.95	3.40	3.32
	3.92	4.18	3.41	3.51
	4.04	4.01	3.22	3.58
90% Calc.	3.53	3.64	3.01	3.12
90% Act.	3.55	3.61	3.01	3.09
	Average	3.99	Average	3.41
		% Diff.	-14.5%	

Table 3.1: Table of maximum loads for Simple Pin Loading tests. Averages are of 100% values only.

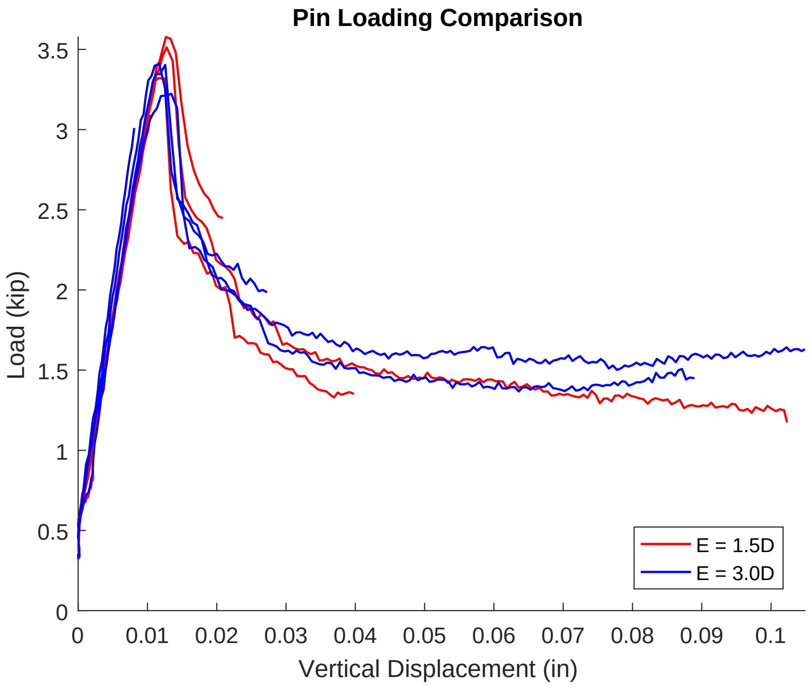

Figure 3.22: Comparison of eccentricity in Simple Pin Loading using Hardened Stainless Steel pins.

Finally, a simple visual inspection of the specimens, seen in Figure 3.23, shows the similarity in bearing failure that occurs.

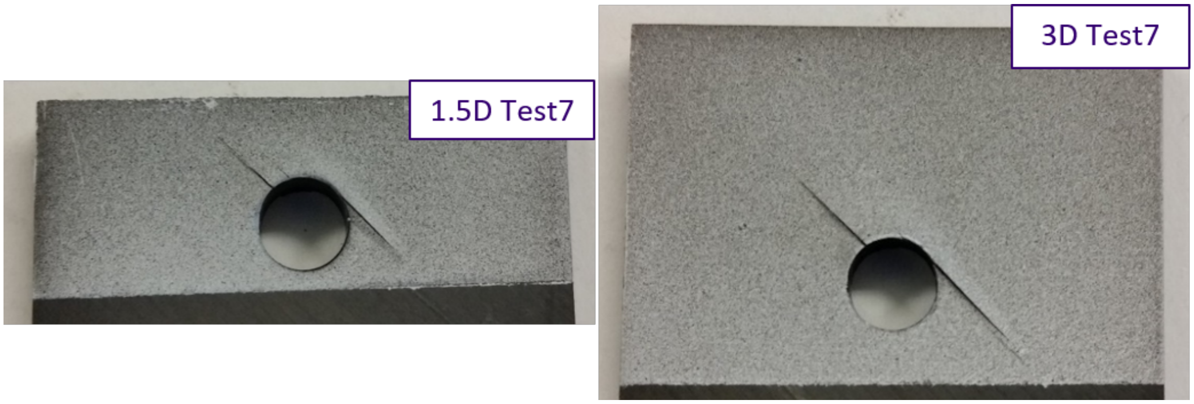

Figure 3.23: Visual comparison of failure mode in Simple Pin Loading specimens.

Chapter 4

WINDOW TESTS - PIN LOADING WITH TRANSPARENT OUT-OF-PLANE CONSTRAINTS

4.1 Fixture Modifications and Test Setup

4.1.1 Fixture Modifications

The fixture used for these tests is the same one used in the Simple Pin Loading tests seen in the previous chapter with slight modifications. As previously mentioned, this fixture was designed as three primary components: two outer, removable plates and one center tab to join them. This flexibility allows transparent components to be installed, applying an out-of-plane constraint to the laminate while maintaining the ability to gather strain field images around the hole. This modified fixture can be seen in Figure 4.1. The transparencies used are machined out of Plexiglas and consist of a washer and flat window on either side. The washer mimics a standard, metal washer and the window applies an even pressure. These transparent pieces can be seen in Figure 4.2.

The thickness of the center tab was determined with these Window tests in mind; the tab must be just under the thickness of the composite specimen and two transparent washers to ensure that when the windows and steel plates are bolted on, there is a slight compressive force on the composite laminate. While the equivalent bolt clamp-up torque is not calculated, it is safe to assume that it is greater than or equal to Crews' $T \approx 0$. [2]

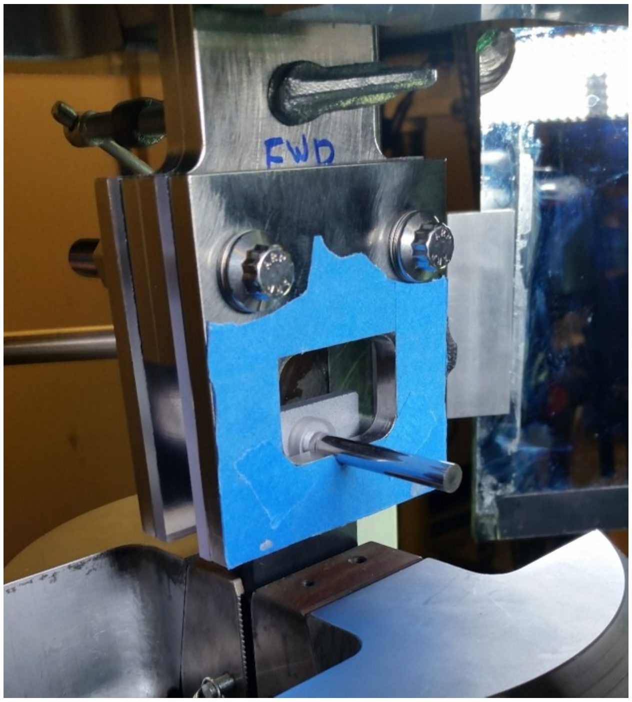

Figure 4.1: Fixture modified to include transparent windows and washers.

Figure 4.2: Transparent washers and windows used to apply out-of-plane constraint.

4.1.2 Test Setup

This test setup is nearly identical to the one used for the Simple Pin Loading tests with the only difference being the position of the lighting. With the added transparencies' thicknesses, it was important to have a light centered on the fixture as opposed to multiple lights, one to each side, which were causing shadows. The left camera seen in Figure 4.3 is focused on the fine speckle pattern on the front face of the specimen. As seen in the upper picture of Figure 4.4, the transparencies only allow the area under the washer to be in focus. While it might be useful to see the strain fields outside of this region, the area closest to the hole is certainly more critical. The right camera is, again, using a mirror reflection to track the vertical displacement on the side of the specimen. This view can be seen in the lower picture of Figure 4.4. The added transparencies are easily seen from this view.

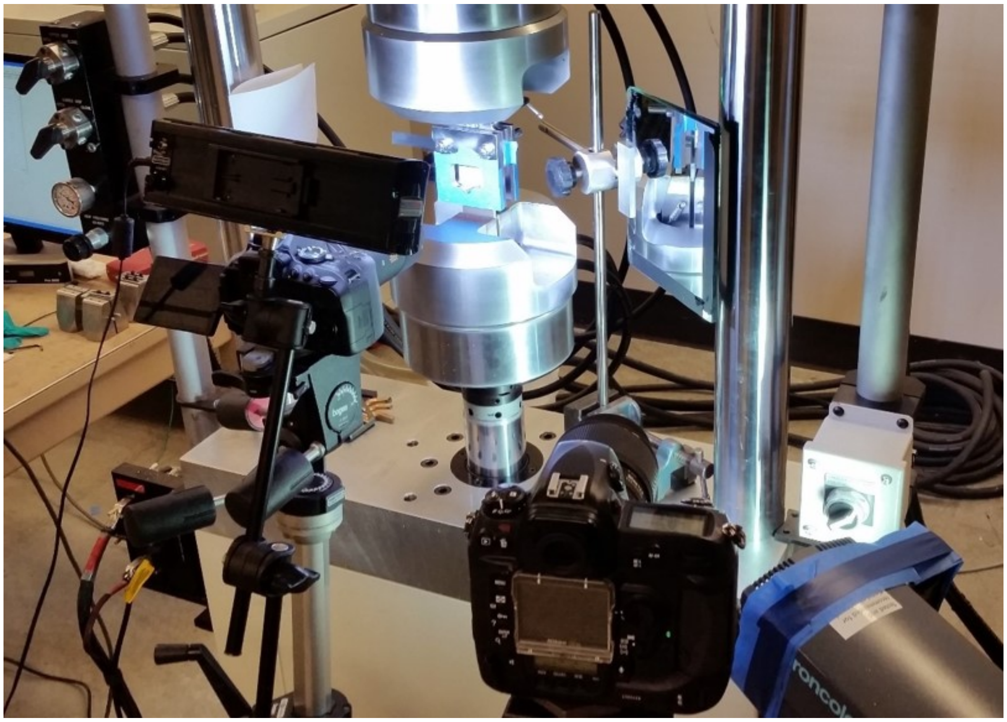

Figure 4.3: Setup of the Window tests including camera locations.

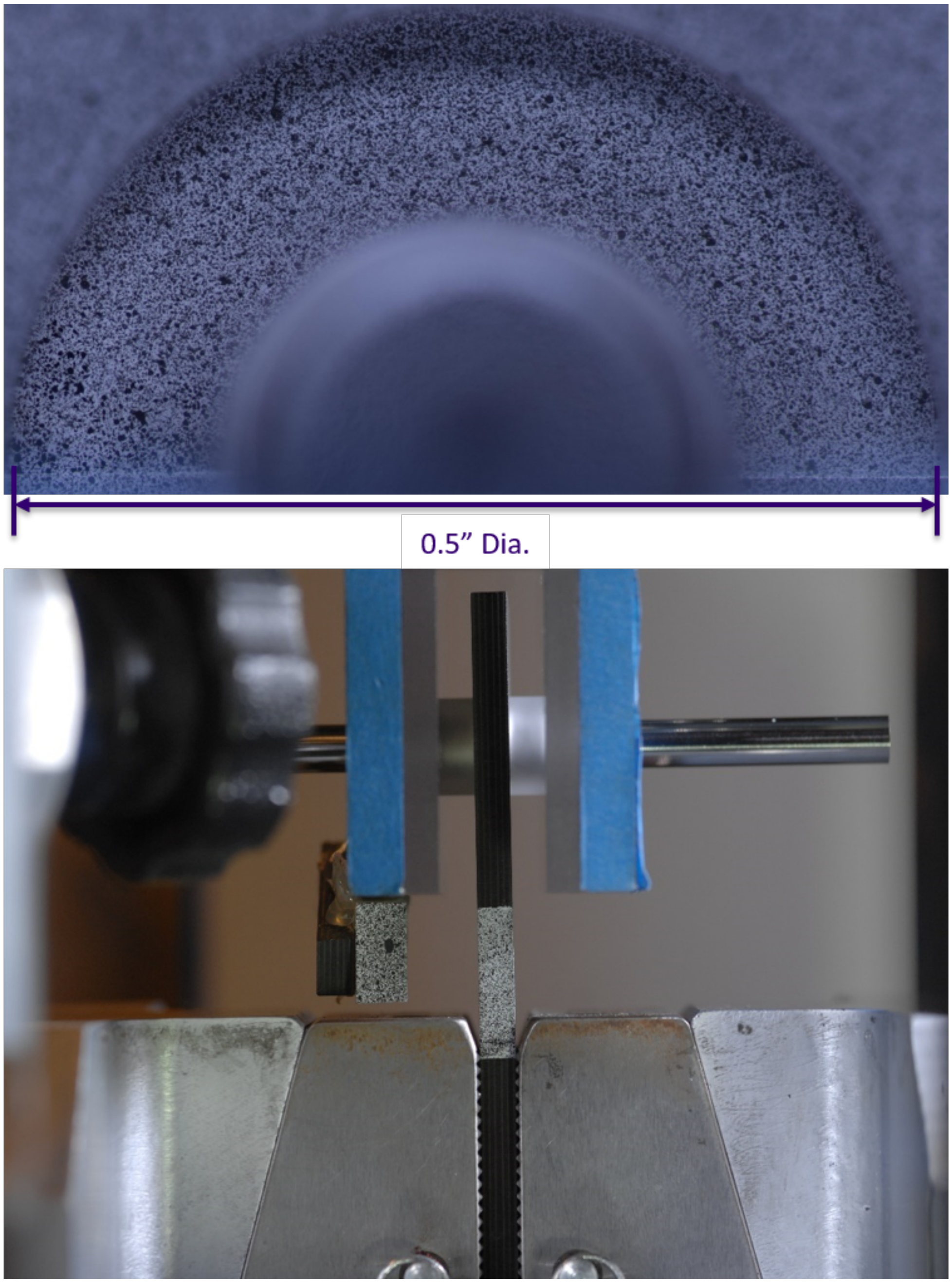

Figure 4.4: Raw images taken from the two cameras seen in Figure 4.3. Top image: Front facing camera. Bottom image: Side facing camera via the mirror reflection.

4.1.3 Failure of Initial Pin

As mentioned in the previous chapter, slight yielding was observed in the pins for the Simple Pin Loading tests and it was quickly realized that the 17-4PH Stainless Steel pin being used was not going to be stiff enough for the Window tests. This minimal yielding in the previous test setup was magnified with the increased effective pin length due to the added Plexiglas windows. The magnitude of the pin bending can be seen in Figure 4.5. The maximum pin bending as seen from the forward- and side-facing cameras can be seen in Figure 4.6. The extreme bending of the pin damaged both the washers and windows and prohibited the forward-facing camera from collecting useful DIC images.

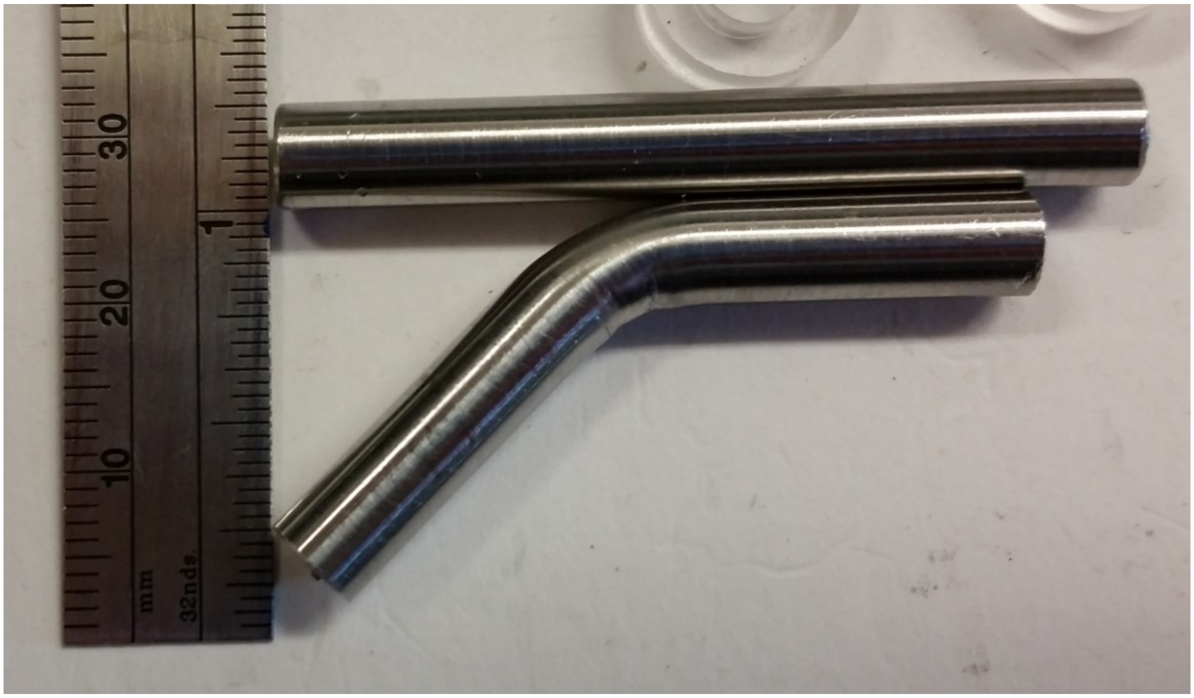

Figure 4.5: Significantly yielded pin shown next to untested pin.

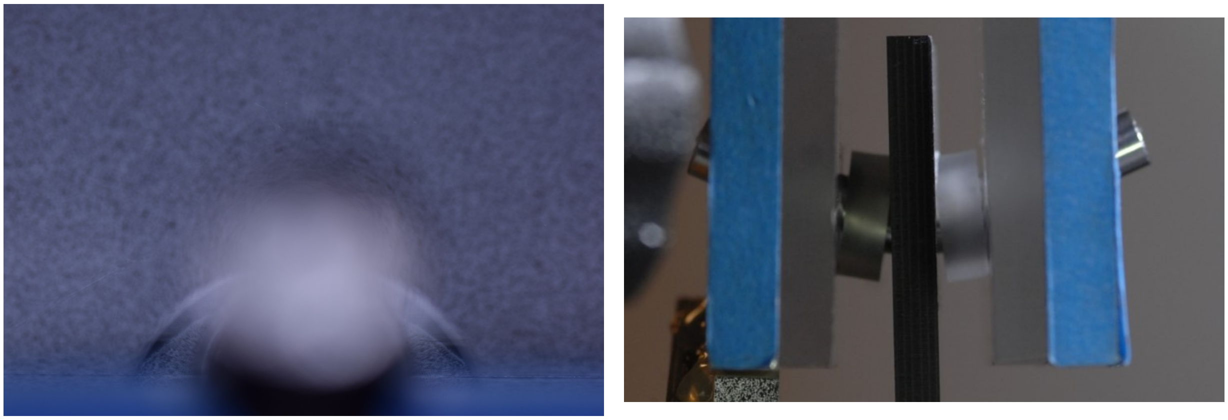

Figure 4.6: Bending of the pin as seen from the forward and side cameras.

No distinct load drop was observed during testing and a lack of significant damage to the specimen explains why. Figure 4.7 shows the damage around the hole of the specimen loaded in the Window test with the 17-4 PH Stainless Steel pin. On the front side, slight hole elongation is observed along with paint scratched away from the surface by the transparent washer digging into the specimen. On the back side, there is a slight bulge at the top of the hole where the fiber has begun to broom outwards along with a single, distinct line of matrix cracking. This brooming primarily occurs because of the stress concentration that develops on the very outer edge of the specimen due to the extremely bent pin.

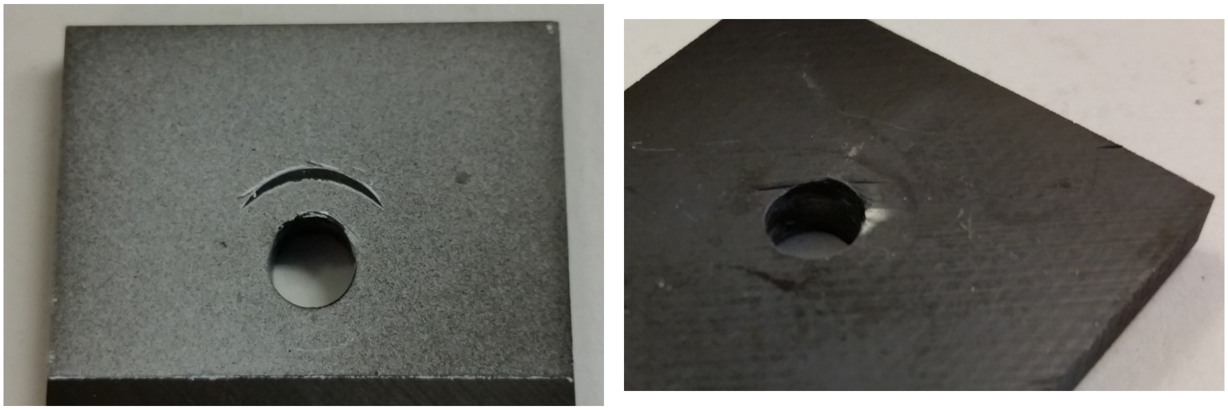

Figure 4.7: Damage incurred on the specimen loaded in the Window test with the 17-4PH SS pin.

4.1.4 Deflection of Steel Windows

A primary design flaw to this test fixture is its lack of out-of-plane displacement restriction. This is not as much of an issue in the Simple Pin Loading tests as the outer plates are closer together and the pin does not bend as much - leading to less of an outward reaction force. However, with the increased effective pin length and the transparencies reacting against the specimen's desire to fail out-of-plane, this outward reaction force increases. To aid future analytical models, the displacement was measure by comparing the distances between the inside, bottom edge of each plate at the start of the test (approximately zero load) and the point at which the maximum load is reached, as shown in Figure 4.8. A deflection of about 0.02 inches was measured.

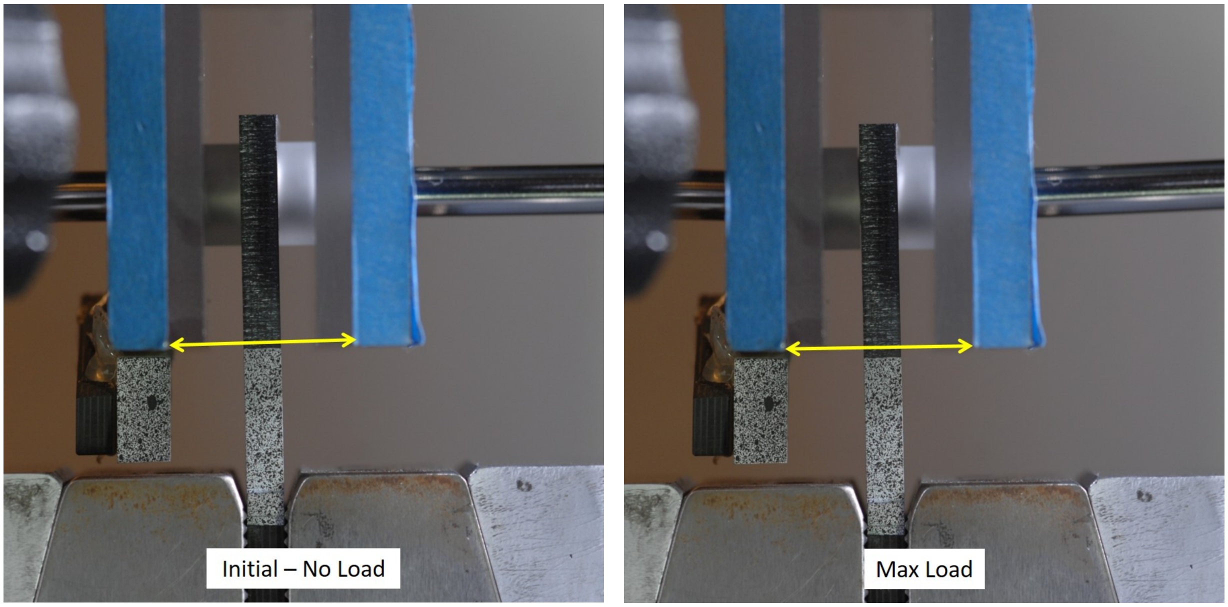

Figure 4.8: Measurement of the deflection of the fixture's outer steel window pieces as shown. An outward displacement at the lower edge of about 0.02 inches.

4.2 E = 1.5D

4.2.1 Test Results

Figure 4.9 shows the load vs. displacement curve for this test. The initial plateau at the peak of this curve resembles Crews' $T \approx 0$ curve, but then the load quickly drops. The biggest difference between Crews' experiment and this one is the eccentricity; this test is $E = 1.5D$, all of Crews' experiments were conducted at $E = 4.0D$. This lack of extra material between the hole and the edge of the specimen explains unstable behavior the quicker drop in load. Despite this significant difference in the post-peak, the pre-peak and failure events are very similar. Figure 4.10 shows the damage induced on the specimen after it has been unloaded and removed from the fixture. Comparing these images to Figure 4.11, we can see that they best resemble the combination of bearing and shearout failure modes.

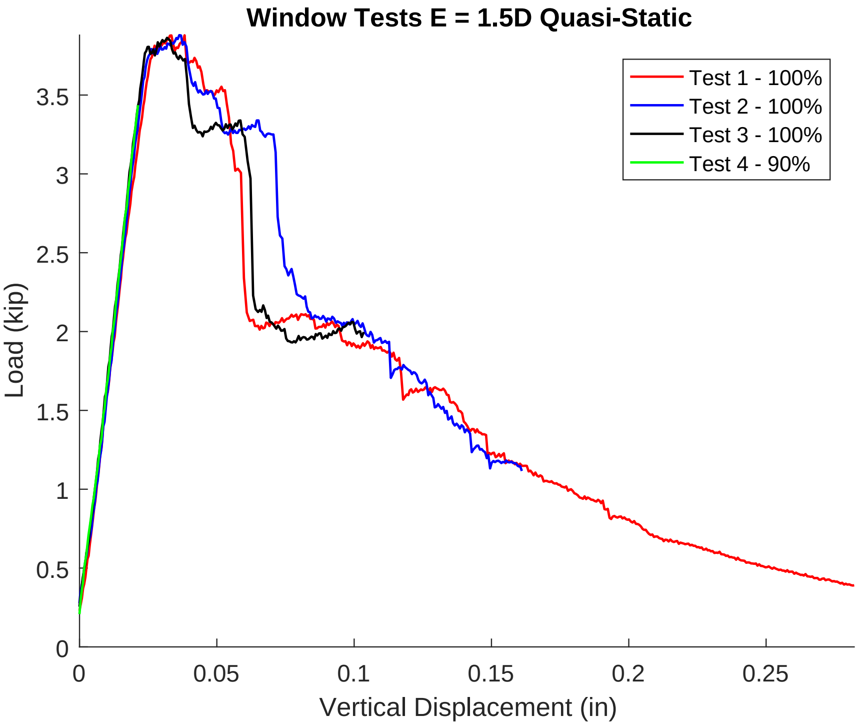

Figure 4.9: Window test, E = 1.5D.

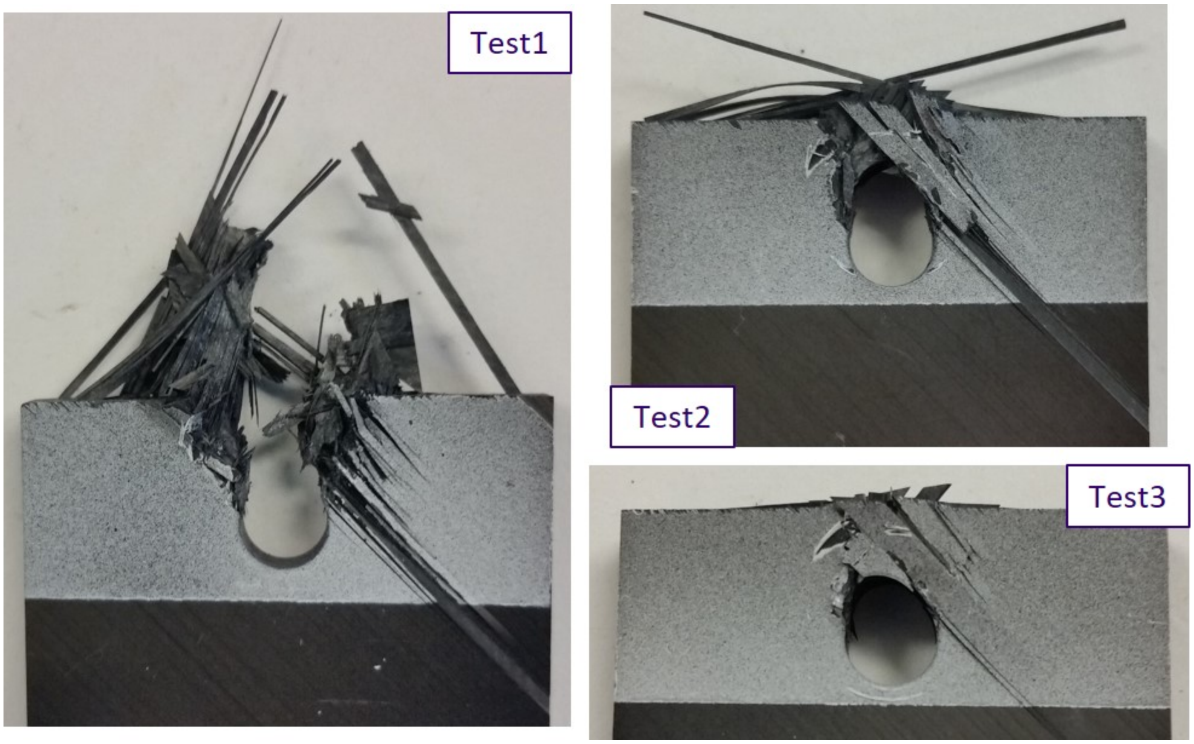

Figure 4.10: Post-test damage for the tests shown in Figure 4.9.

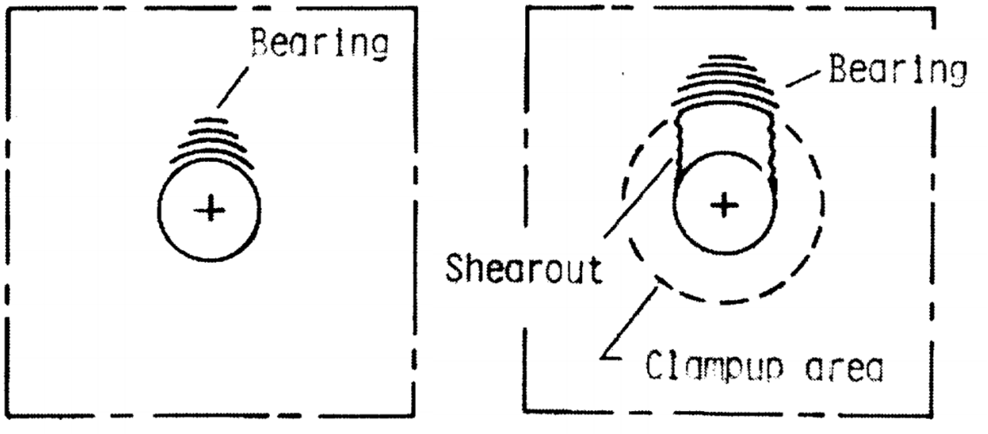

Figure 4.11: Figure 4(a) and (b) from Crews. Left: (a) Bearing failure mode. Right: (b) Combined bearing and shearout failure modes seen in a joint with clamp-up.

4.2.2 DIC

Figure 4.12 shows DIC strain plots for the normal strain in the loading direction, ε_{YY}, at distinct moments along with their locations on the load curve. At point A, just as the load begins its plateau region, there are very faint hot (tension) and cold (compression) spots along with one small, red, thin line to the left at a 45 degree angle, perpendicular to the hole. At point B, the strain has grown significantly. Directly above the hole the specimen has gone into compression as expected. The thin red line at 45 degrees has doubled to two instances and grown to the edge of the washer. To either side of the hole, the specimen is being pulled upwards with the pin, creating large hot spots. This is in contrast to the Simple Pin Loading where the pin is able to just peel the fibers out of its way. The out-of-plane displacement is causing a very clear shearout failure. This shearout mode becomes more apparent at point C with the left and right sides in tension and the center section, above the hole, in compression. When the load initially drops, at point D, we can see distinct breaks in the DIC strain fields caused by cracks in the surface. There are matrix cracks in the 45 degree direction, but also fiber failure perpendicular to these.

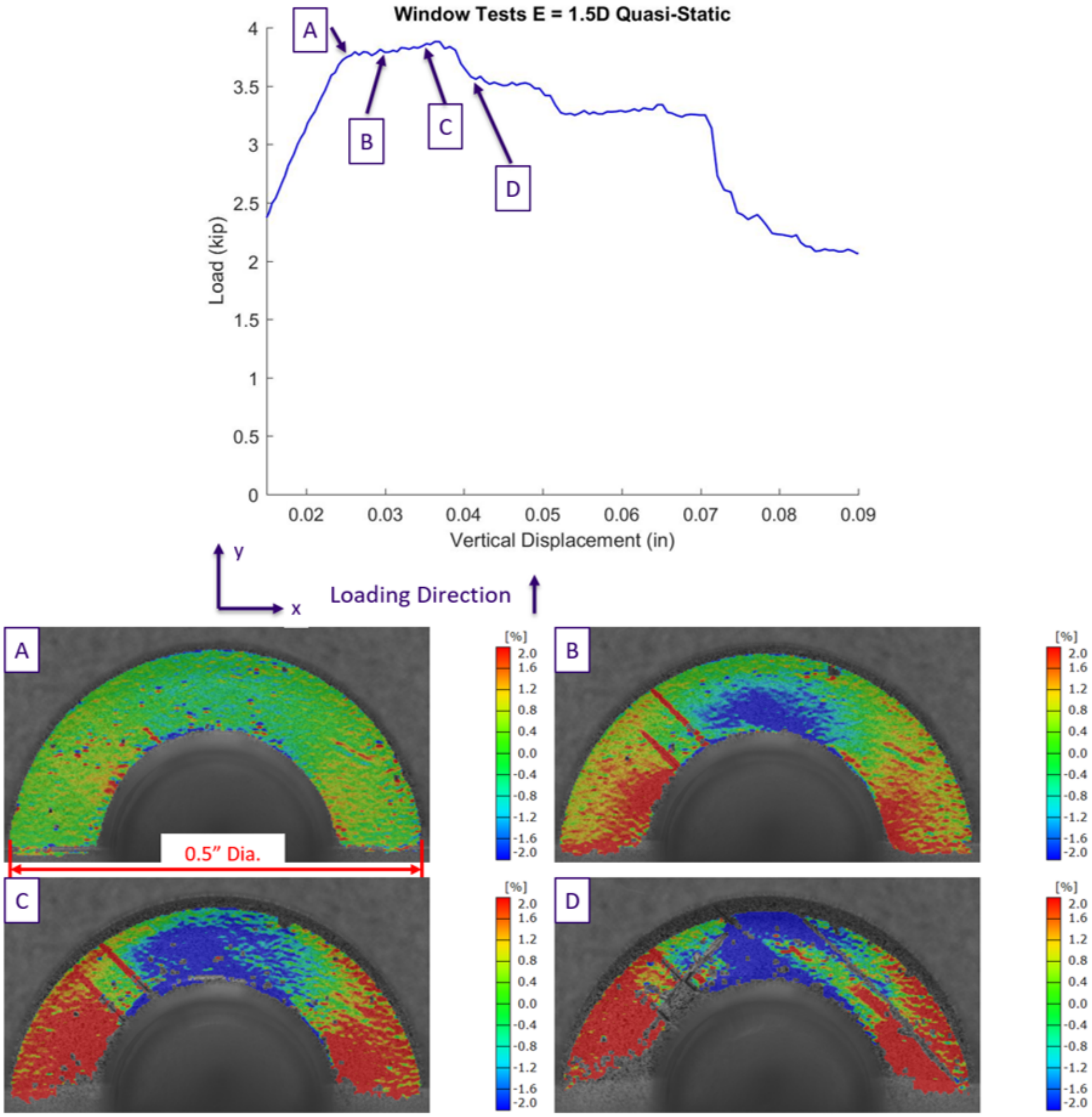

Figure 4.12: ε_{YY} DIC Strain Plots for Test 2. Peak region shown.

4.2.3 CT Scans

Figures 4.13 through 4.17 show CT images of test 3. Figure 4.13 shows a 3D rendering of three angles so that the extent of the damage can be seen. Figure 4.14 shows ply 7, -45 degrees. Figure 4.15 shows ply 10, 0 degrees. Figure 4.16 shows the center of the laminate, plies 12 and 13, 90 degrees. All three of these slices show clear signs of shearout failure. In ply 10, the matrix cracking presents a clear picture of a plug of material shearing out of the specimen. The center of the laminate has extensive fiber bridging and even fiber failure in the center. Figure 4.17 shows side slices, at the center and just inside the left and right edge of the hole. Extensive delamination can be seen at the specimen's top edge while brooming has been restricted by the washer.

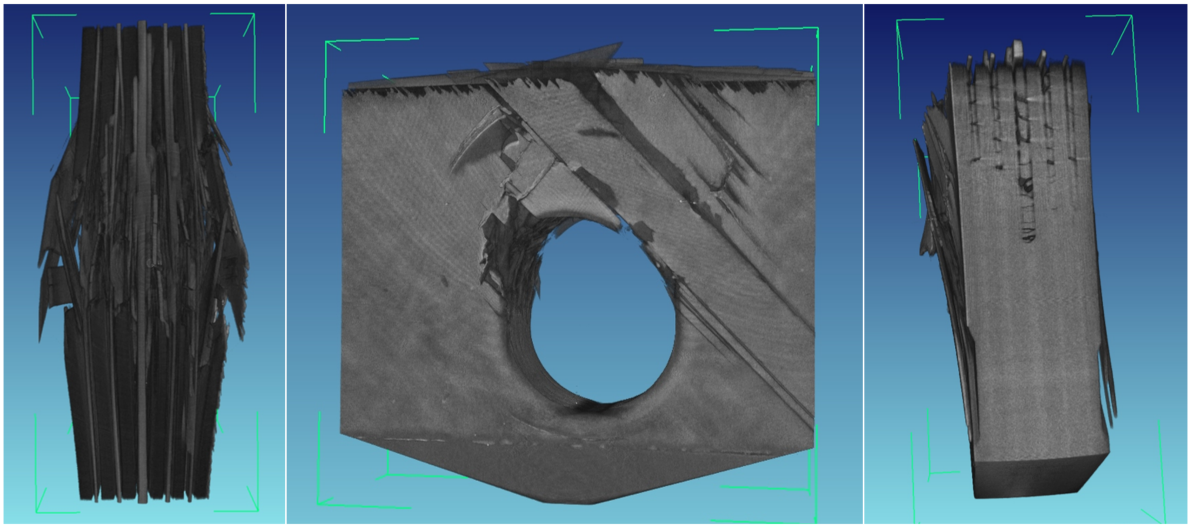

Figure 4.13: CT scan of Test 3. 3D rendering of scanned area. Top, Front, and Side views seen (L to R).

Ply	1	2	3	4	5	6	7	8	9	10	11	12	13	14	15	16	17	18	19	20	21	22	23	24
Orien.	45°	0°	-45°	90°	45°	0°	-45°	90°	45°	0°	-45°	90°	90°	-45°	0°	45°	90°	-45°	0°	45°	90°	-45°	0°	45°

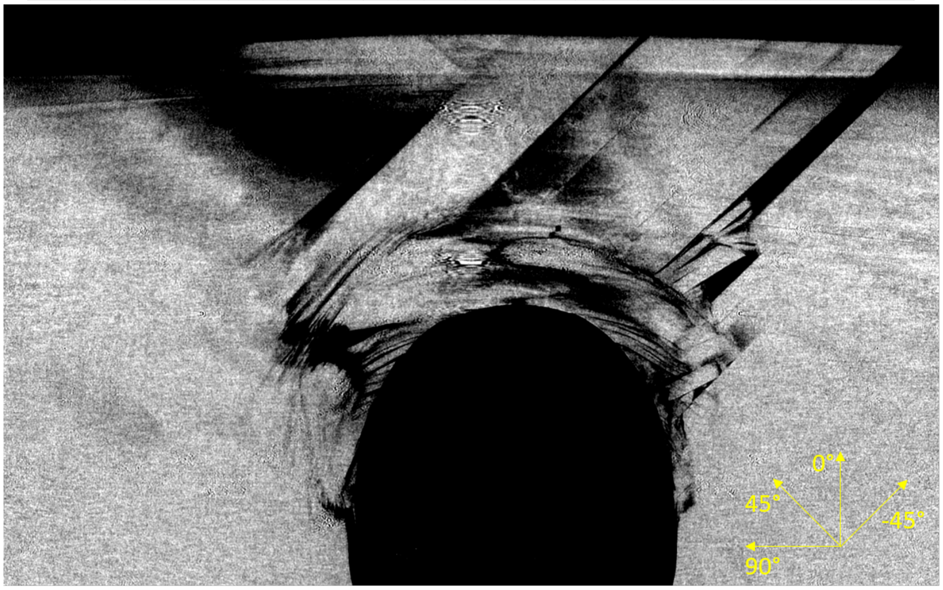

Figure 4.14: CT scan of Test 3, ply 7. Clear signs of shearout failure in -45.

Ply	1	2	3	4	5	6	7	8	9	10	11	12	13	14	15	16	17	18	19	20	21	22	23	24
Orien.	45°	0°	-45°	90°	45°	0°	-45°	90°	45°	0°	-45°	90°	90°	-45°	0°	45°	90°	-45°	0°	45°	90°	-45°	0°	45°

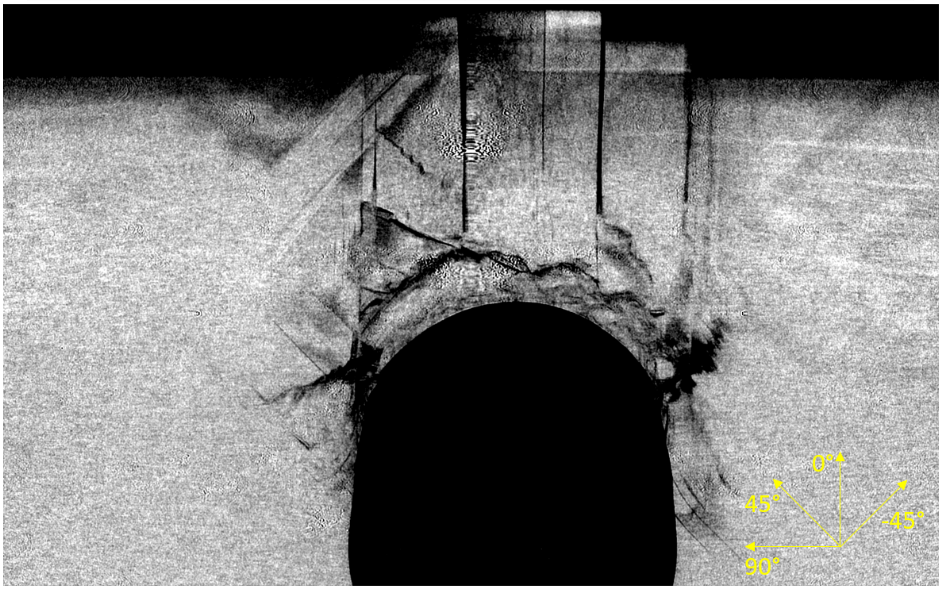

Figure 4.15: CT scan of Test 3, ply 10. Clear signs of shearout failure in 0.

Ply	1	2	3	4	5	6	7	8	9	10	11	12	13	14	15	16	17	18	19	20	21	22	23	24
Orien.	45°	0°	-45°	90°	45°	0°	-45°	90°	45°	0°	-45°	90°	90°	-45°	0°	45°	90°	-45°	0°	45°	90°	-45°	0°	45°

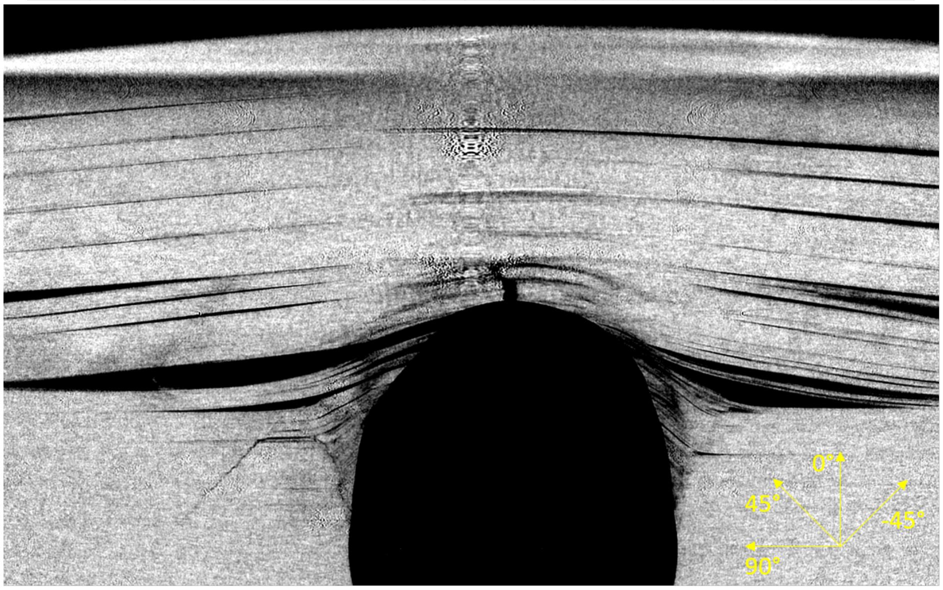

Figure 4.16: CT scan of Test 3, plies 12 and 13, center of the laminate. Clear signs of shearout failure in 90. Matrix and fiber failure.

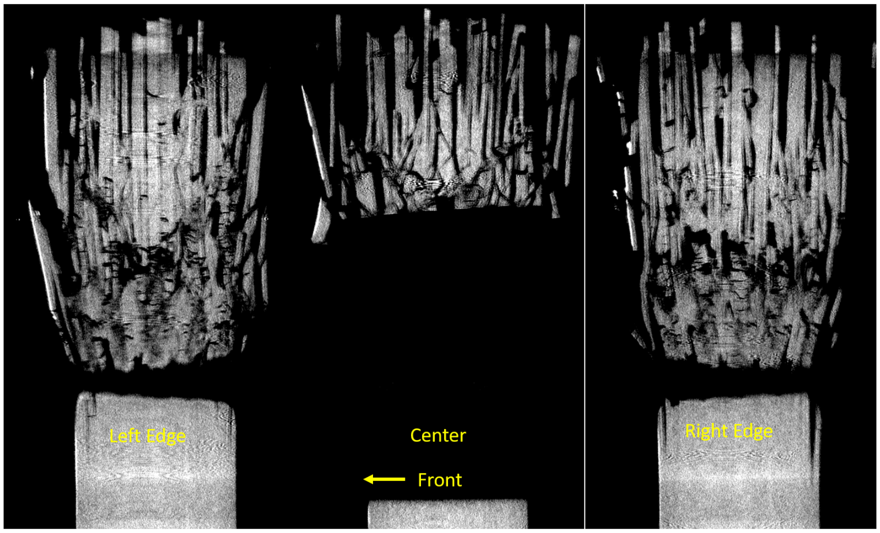

Figure 4.17: CT scan of Test 3. Side slices, loading direction: up. Significant delamination at specimen edge (top). Minimal brooming around hole as expected due to washer constraint.

Figure 4.18 shows the CT images of Test 4, the test taken to 90% of the peak load. Minor matrix cracking is seen only in the outer plies.

Ply	1	2	3	4	5	6	7	8	9	10	11	12	13	14	15	16	17	18	19	20	21	22	23	24
Orien.	45°	0°	-45°	90°	45°	0°	-45°	90°	45°	0°	-45°	90°	90°	-45°	0°	45°	90°	-45°	0°	45°	90°	-45°	0°	45°

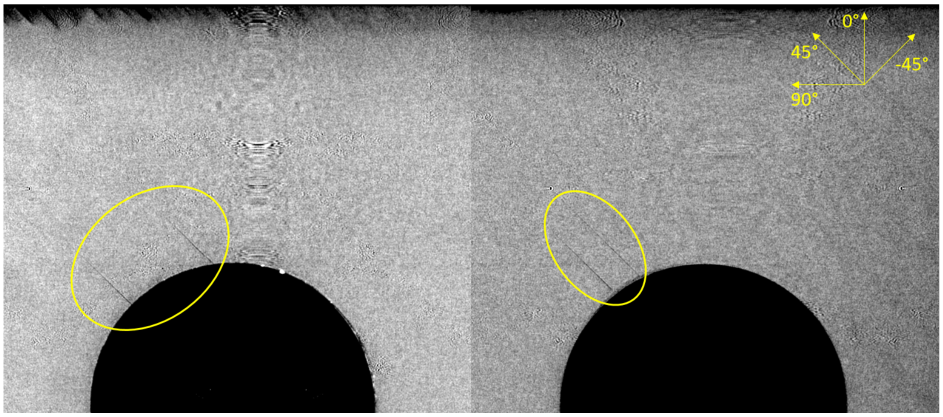

Figure 4.18: CT scan of Test 4, Left: Ply 1. Right: Ply 24. Both plies exhibit minor matrix cracking along fiber direction, perpendicular to hole.

4.3 E = 3.0D

4.3.1 Test Results

Figure 4.19 shows the load vs. displacement curve for this test. The entirety of this curve resembles Crews' $T \approx 0$ curve very closely. The additional eccentricity added in this case is much more similar to Crews' $E = 4.0D$. Figures 4.20 and 4.21 show the damage induced on the specimen after it has been unloaded and removed from the fixture. In the Test 1 case, because the load continued to increase after the initial failure, the HSS pin failed. In Test 2, the combination of the bearing and shearout failure modes is very clear. The area previously under the washer exhibits shearout characteristics while further out, bearing failure can be clearly seen with the fibers pushing out-of-plane. In both Test 2 and 3, there is a slight bulge above the hole due to the failing specimen being resisted by the softer washer.

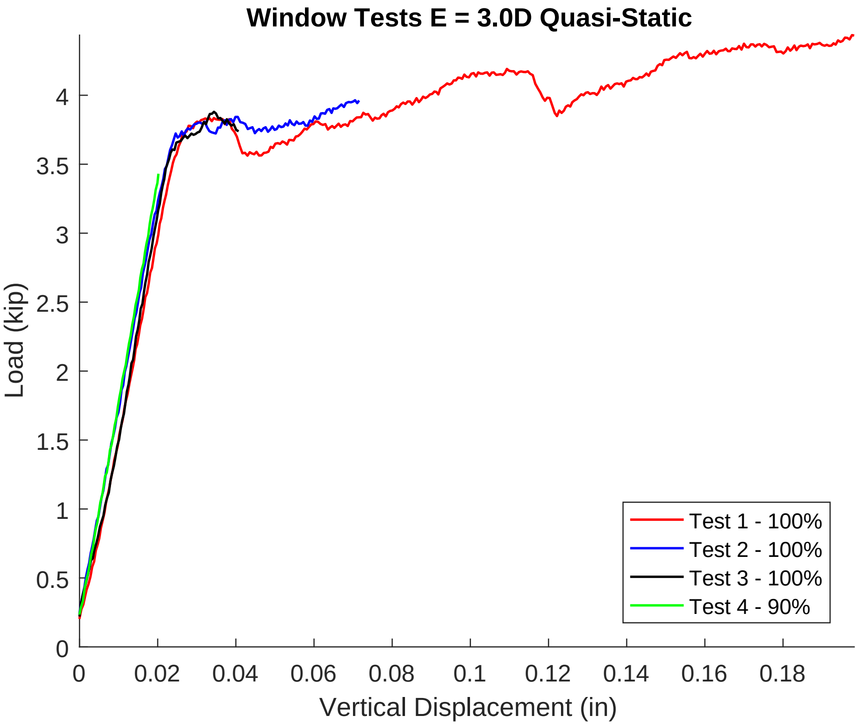

Figure 4.19: Window test, E = 3.0D.

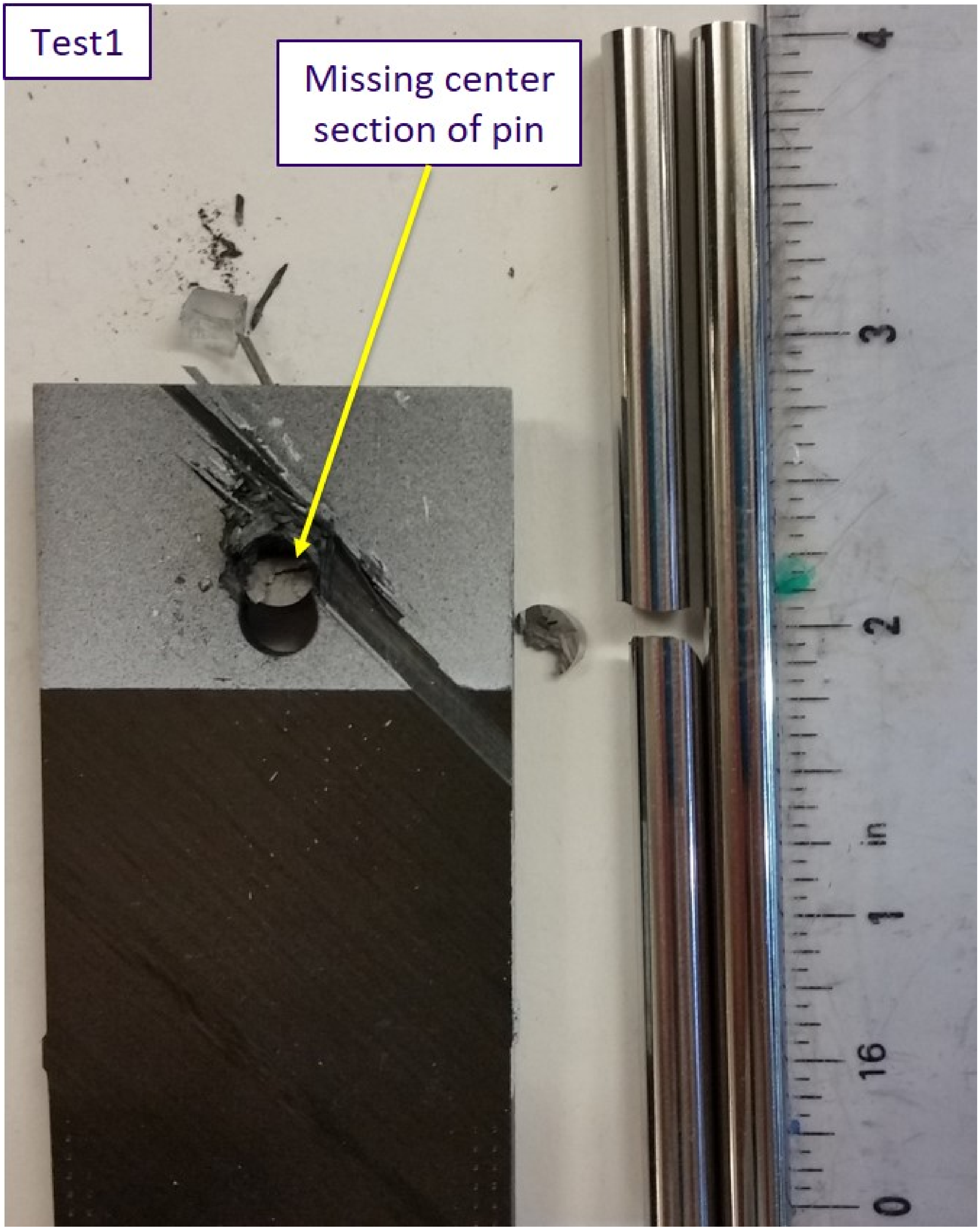

Figure 4.20: Post-test damage for Test 1 shown in Figure 4.19.

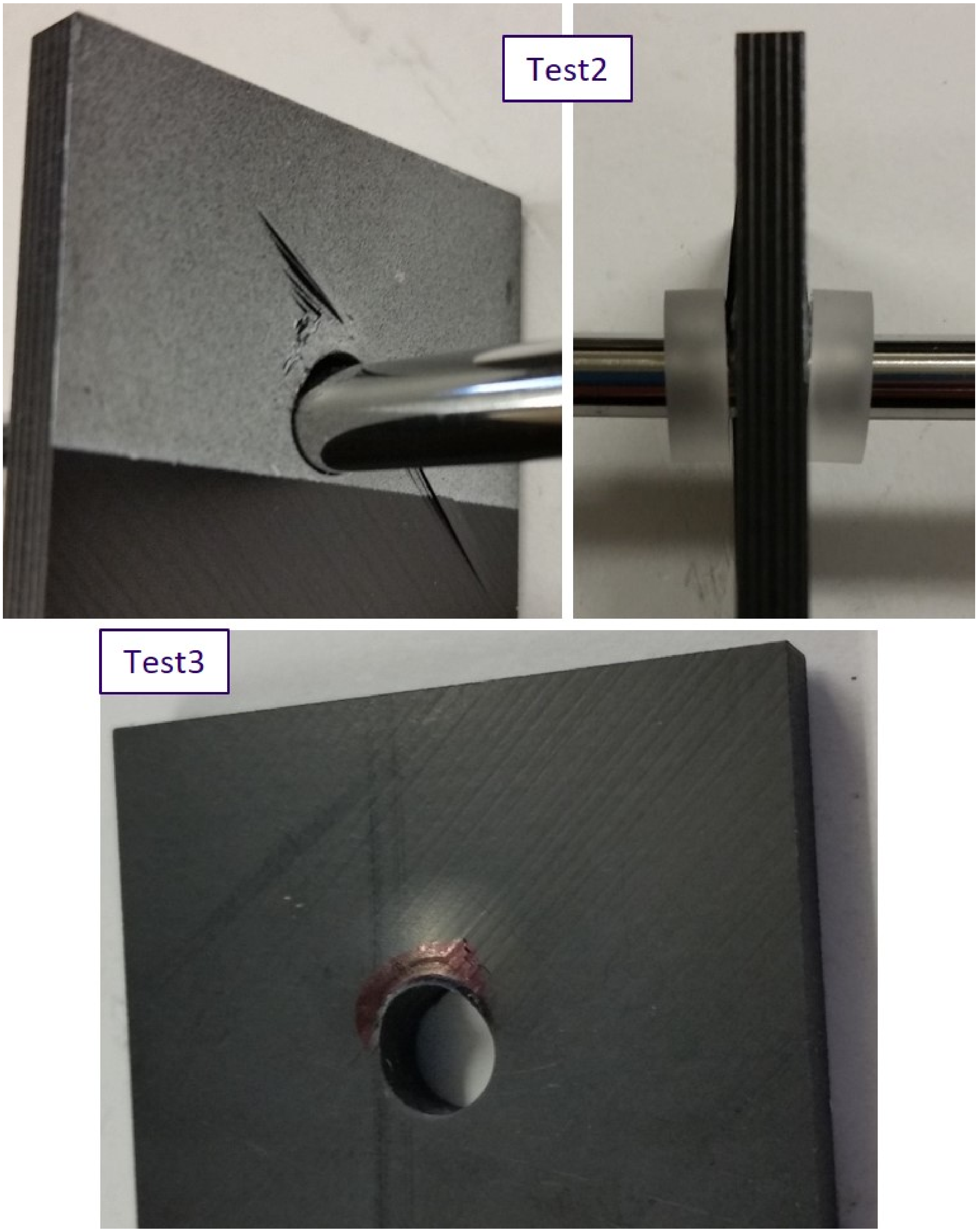

Figure 4.21: Post-test damage for Tests 2 and 3 shown in Figure 4.19.

4.3.2 DIC

Figure 4.22 shows DIC strain plots for the normal strain in the loading direction, ε_{YY}, at distinct moments along with their locations on the load curve. The behaviors seen in these images are nearly identical to those seen in the $E = 1.5D$ case. It is interesting to note at point D, the load drop that occurs is very insignificant compared to the one experienced in the previous case. This difference between the eccentricities can be explained simply by the difference in material supporting the joint. The shorter eccentricity resembles more of a beam in bending; a scenario with less stiffness than the $E = 3.0D$ case.

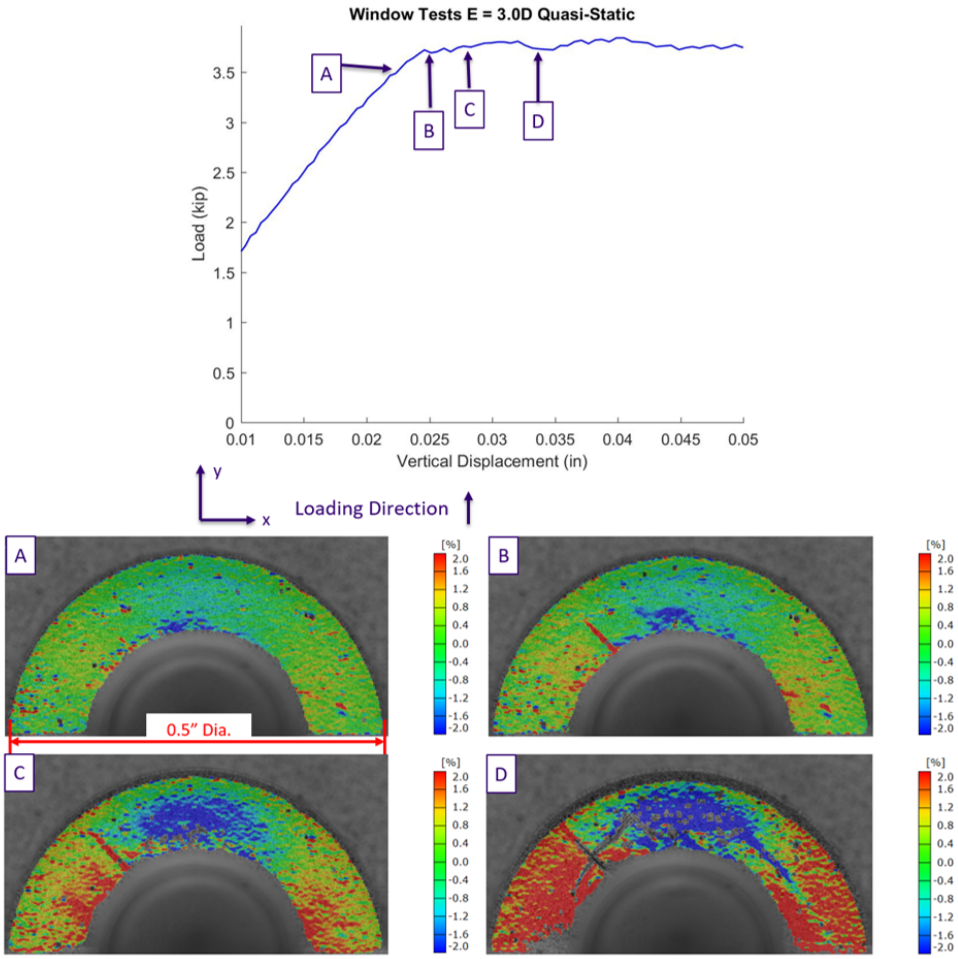

Figure 4.22: ε_{YY} DIC Strain Plots for Test 2. Peak region shown.

4.3.3 CT Scans

Figures 4.23 through 4.25 show CT images of test 3. Figure 4.23 shows, on the left, ply 13, and on the right, plies 16 and 17. Ply 13 (90), at the top of the hole, and Ply 16 (45), at the top right of the hole, both exhibit fiber cracking. Ply 17 (90) exhibits minor matrix cracking to the left of the hole. Figure 4.24 shows, on the left, plies 20 and 21, and on the right, plies 23 and 24. Matrix cracking can be seen to the left of the hole in both ply 20 (45) and ply 21 (90). Fiber cracking is seen to the top right in ply 20. In both plies 23 and 24, matrix cracking is present. Figure 4.25 shows side slices, at the center and just inside the left and right edge of the hole. Slight brooming can be seen in the center of the hole and delamination as a whole is rather minimal primarily due to this specimen still being in the plateau region when unloaded.

Ply	1	2	3	4	5	6	7	8	9	10	11	12	13	14	15	16	17	18	19	20	21	22	23	24
Orien.	45°	0°	-45°	90°	45°	0°	-45°	90°	45°	0°	-45°	90°	90°	-45°	0°	45°	90°	-45°	0°	45°	90°	-45°	0°	45°

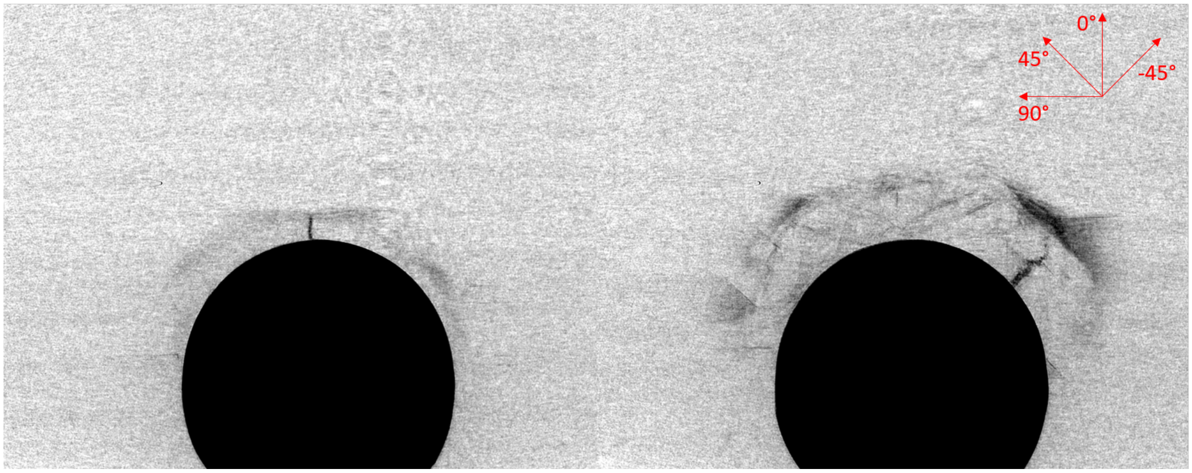

Figure 4.23: CT scan of Test 3. Left: Ply 13. Fiber cracking at the top of the hole. Right: Plies 16 and 17. Fiber cracking in ply 16 (45) to top right of hole. Minor matrix cracking in ply 17 (90) to left of hole.

Ply	1	2	3	4	5	6	7	8	9	10	11	12	13	14	15	16	17	18	19	20	21	22	23	24
Orien.	45°	0°	-45°	90°	45°	0°	-45°	90°	45°	0°	-45°	90°	90°	-45°	0°	45°	90°	-45°	0°	45°	90°	-45°	0°	45°

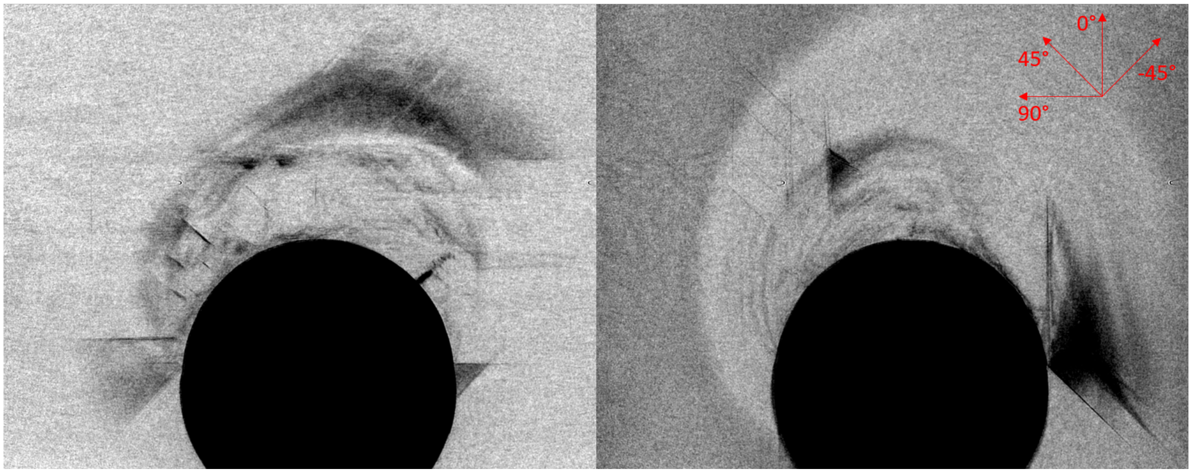

Figure 4.24: CT scan of Test 3. Left: Plies 20 and 21. Matrix cracking to top left and fiber cracking to top right of hole seen in ply 20 (45). Matrix cracking to left in ply 21 (90). Right: Plies 23 and 24. Matrix cracking seen in both plies.

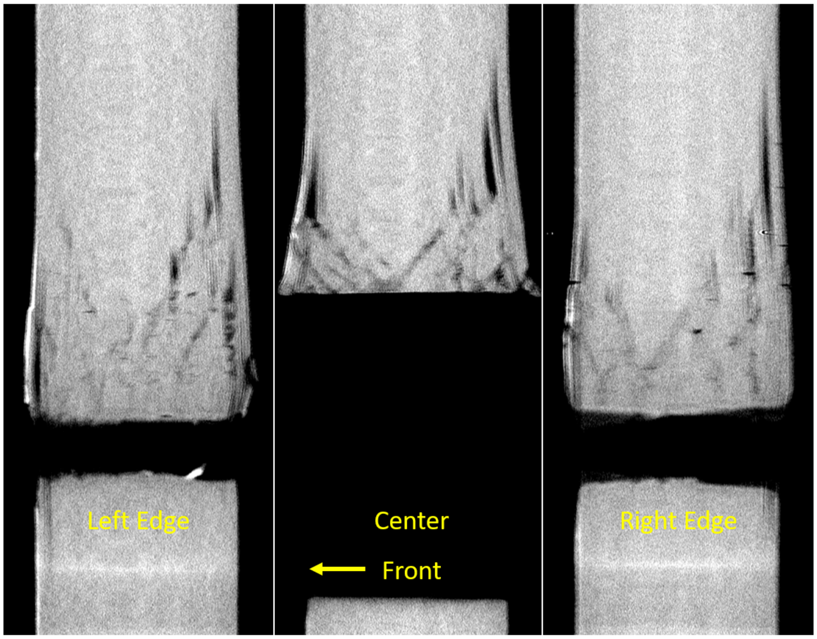

Figure 4.25: CT scan of Test 3. Side slices, loading direction: up. Slight brooming seen in the center of the hole.

4.4 Comparison of Eccentricities

Figure 4.26 clearly shows that the effect of eccentricity in this test is seen solely after the joint fails. The load vs. displacement curves are identical until a vertical displacement of approximately 0.04 in. At this point, the $E = 1.5D$ case becomes unstable and the load-carrying ability drops off in a staircase-type manner. For the $E = 3.0D$ case, however, the joint slowly continues to increase load. Figure 4.27 shows the load vs. displacement curve focused at the peak; the divergence in behaviors is very clear.

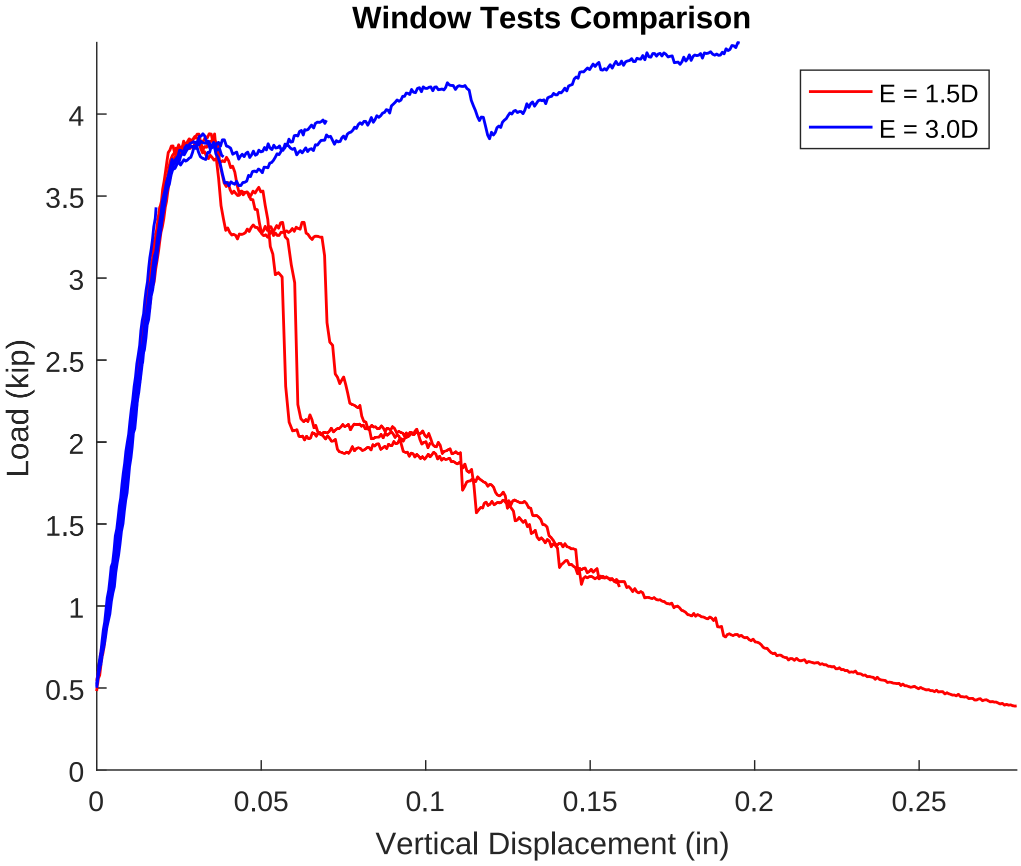

Figure 4.26: Comparison of eccentricity in Window tests. Full extent of data shown.

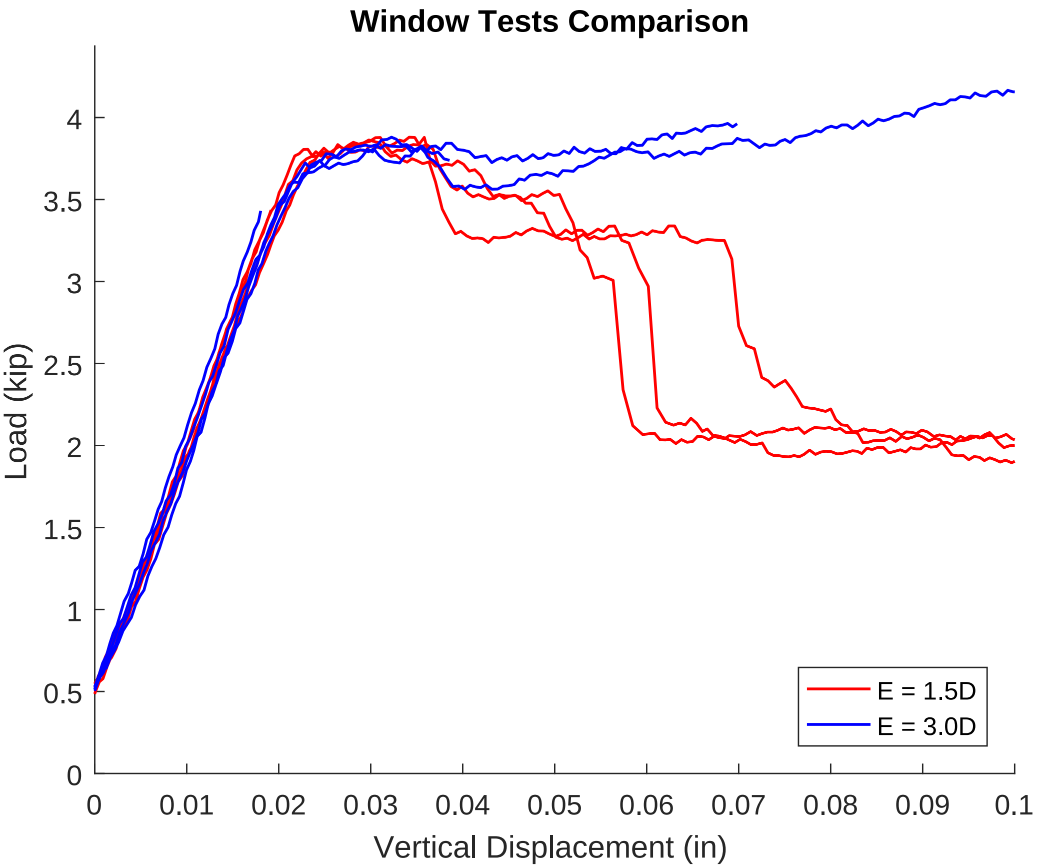

Figure 4.27: Comparison of eccentricity in Window tests. Peak region shown.

4.5 Comparison to Pin Loading

The noticeable difference in the initial slope of the load vs. displacement curve seen in Figure 4.28 can be explained by the increase in effective length of the pin. This increase is due to the addition of the transparent windows; their added thickness shifts the removable, steel plates of the fixture outward. Comparing Figures 3.4 and 4.4 helps to see this. The total increase in effective pin length is 0.344 in.

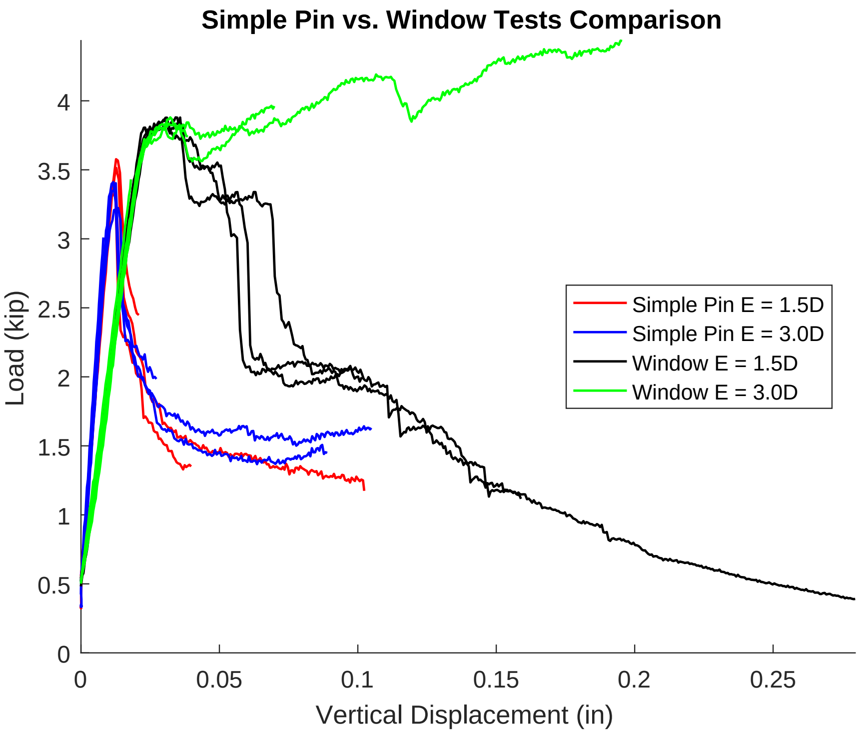

Figure 4.28: Comparison of Simple Pin Loading and Window tests and their varying eccentricities.

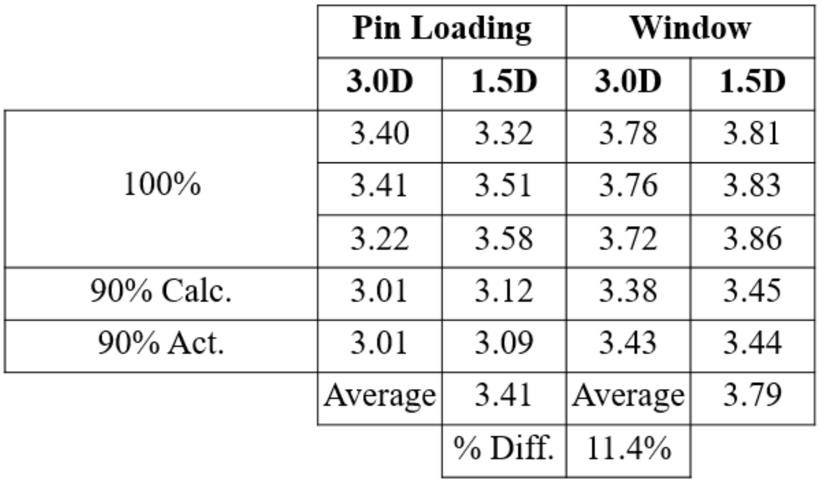

	Pin Loading		**Window**	
	3.0D	**1.5D**	**3.0D**	**1.5D**
100%	3.40	3.32	3.78	3.81
	3.41	3.51	3.76	3.83
	3.22	3.58	3.72	3.86
90% Calc.	3.01	3.12	3.38	3.45
90% Act.	3.01	3.09	3.43	3.44
	Average	3.41	Average	3.79
		% Diff.	11.4%	

Table 4.1: Comparison table of maximum loads for Simple Pin Loading tests vs. Window tests. Averages are of 100% values only.

Chapter 5

DOUBLE SHEAR BOLTED JOINT

5.1 *Fixture Design and Test Setup*

5.1.1 ASTM D5961M Fixture Design

The fixture used for these Double Shear Bolted Joint tests is a simplified version of the fixture described in ASTM D5961M. It consists of two steel reaction skins and one aluminum spacer. A diagram of this fixture can be seen in Figure 5.1. The spacer is shimmed as necessary to match the thickness of the specimen and two washers; this ensures the loading is purely vertical. All bolts are tightened to a torque of ≈ 7 ft-lbs.

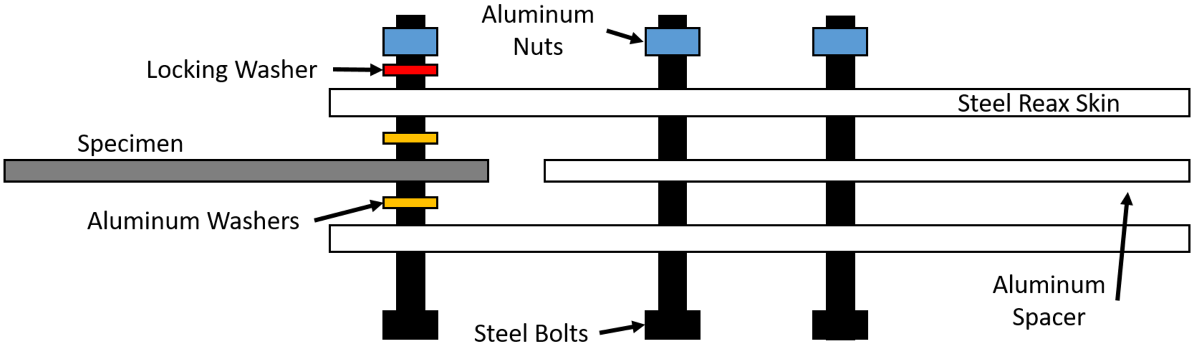

Figure 5.1: Double Shear Bolted Joint fixture.

5.1.2 Test Setup

The setup for these tests is the simplest of the three. A single camera is used to capture only the displacement. As in the previous setups, the displacement is gathered off of the side using a mirror reflection as seen in Figure 5.2.

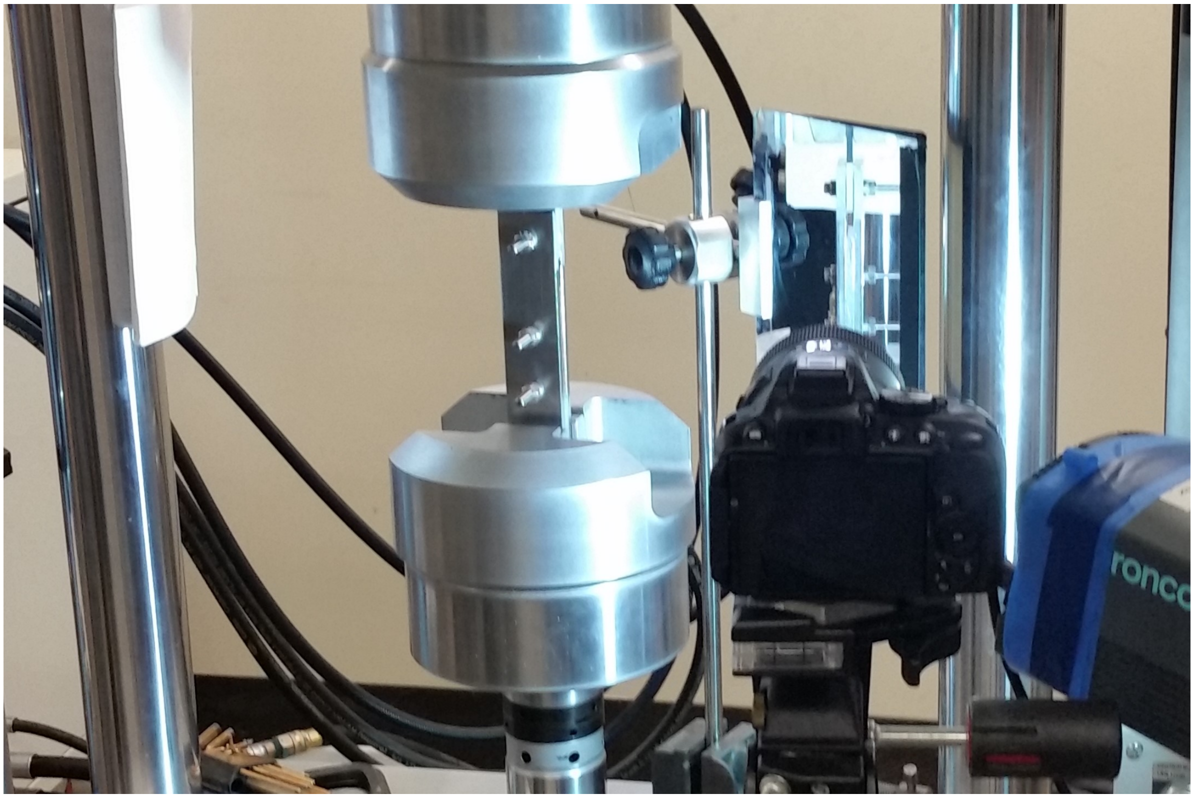

Figure 5.2: Setup of the DSBJ tests.

5.1.3 Displacement Measurement

Similar to the previous test setups, a coarse speckle pattern is painted on the side of the specimen. However, in this case, the painted region encompasses the bolt axis. It was decided that this displacement measure would be the best representation of hole elongation. Both sides of the steel fixture are painted to ensure even loading; the camera's view of these patterns can be seen in Figure 5.3 (Note: Picture has been rotated for this document). To determine the appropriate point of measurement, three axes were chose to focus on, labeled "A-C" and compared to one another. The results of that comparison are shown in Figure 5.4. Even when focused on the peak of the plot, the difference between measurement locations is negligible. For consistency, the displacement measurement for all tests is taken from the left point on axis A.

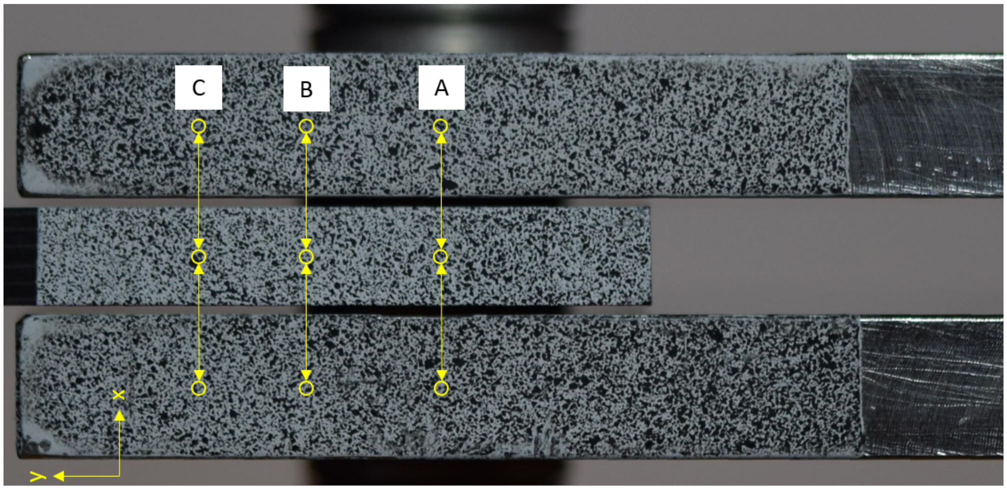

Figure 5.3: Locations utilized for displacement/hole elongation measurements. Note: Picture is rotated for this document.

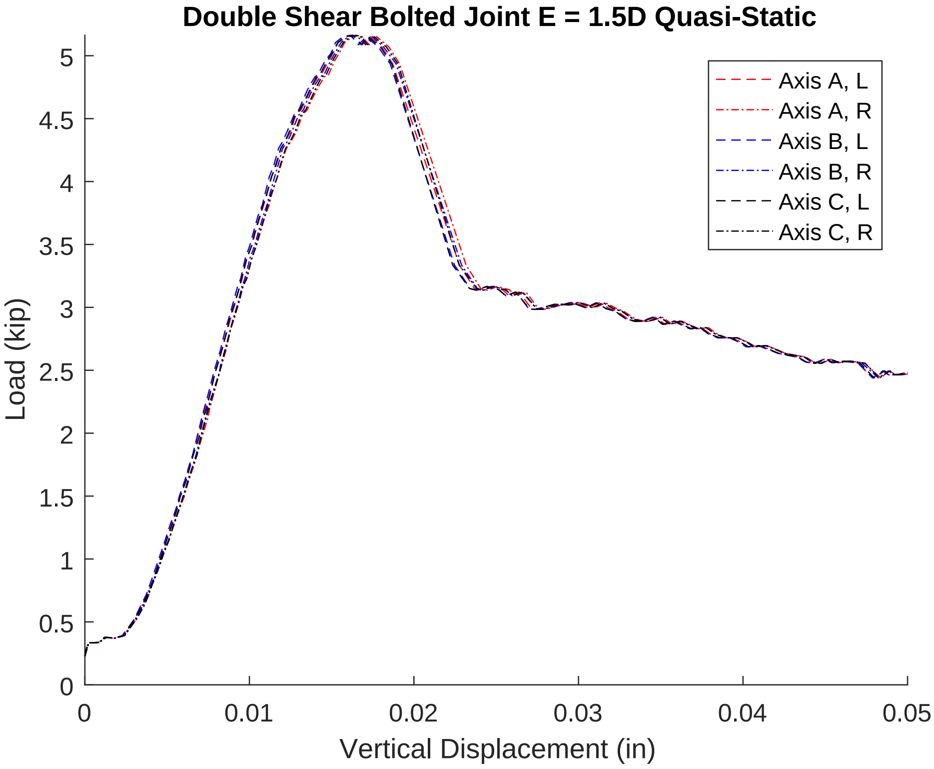

Figure 5.4: Comparison of load vs. displacement curves based on measuring location.

5.2 E = 1.5D

5.2.1 Test Results

These test results strongly resemble those from the Window tests; the load peaks in a slight plateau region before falling off. The primary difference between these tests is the peak value achieved is much higher in the Double Shear Bolted Joint tests. This can be attributed to the bolt and joint being in pure shear with a stiffer out-of-plane displacement as opposed to a pin undergoing bending with a soft out-of-plane displacement.

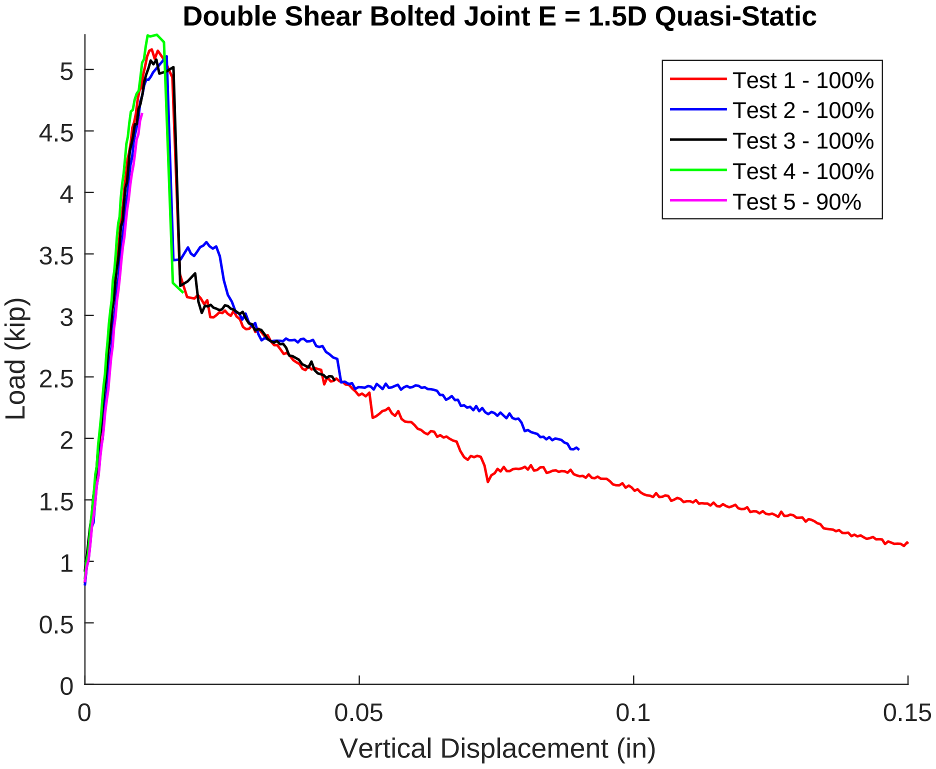

Figure 5.5: Double Shear Bolted Joint, E = 1.5D.

5.2.2 CT Scans

Figures 5.6 through 5.8 show CT images of test 4. Figure 5.6 shows, on the left, plies 2 and 3 together, and on the right, ply 3 alone. This left image shows matrix cracking in ply 2 (0) running tangent to the hole and in ply 3 (-45) at the very top of the image. The right image shows fiber cracking to the top left of the hole along with a slight amount of matrix failure and fiber bridging in ply 4 to the right side of the image. Figure 5.7 shows, on the left, ply 5, and on the right, plies 12 and 13, the center of the laminate. Fiber cracking is very prominent in ply 5 (45) with some matrix cracking towards the top of the image. Fiber bridging and matrix failure is seen in the center of the laminate. Figure 5.8 shows side slices, at the center and just inside the left and right edge of the hole. Significant delamination occurs towards the specimen edge at the top of the images.

Ply	1	2	3	4	5	6	7	8	9	10	11	12	13	14	15	16	17	18	19	20	21	22	23	24
Orien.	45°	0°	-45°	90°	45°	0°	-45°	90°	45°	0°	-45°	90°	90°	-45°	0°	45°	90°	-45°	0°	45°	90°	-45°	0°	45°

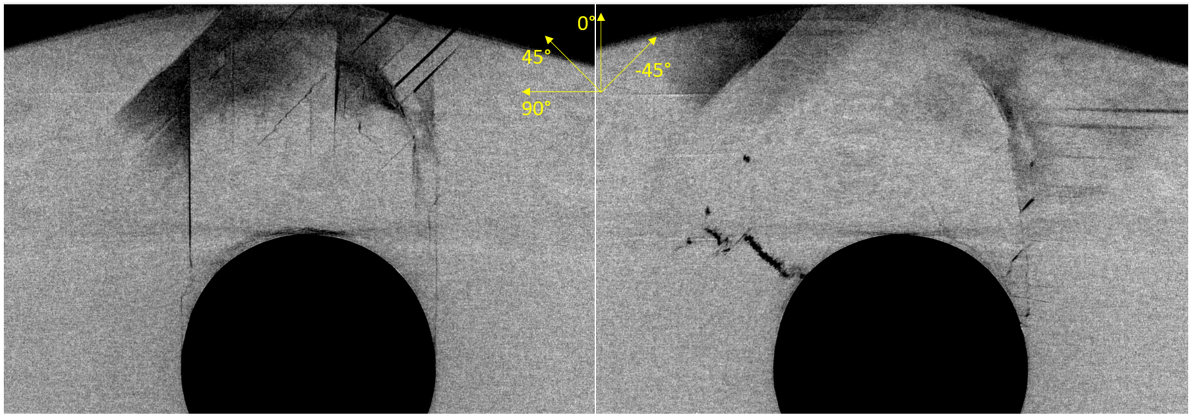

Figure 5.6: CT scan of Test 4. Left: Plies 2 and 3. Matrix cracking. Right: Ply 3. Fiber cracking top left of hole.

Ply	1	2	3	4	5	6	7	8	9	10	11	12	13	14	15	16	17	18	19	20	21	22	23	24
Orien.	45°	0°	-45°	90°	45°	0°	-45°	90°	45°	0°	-45°	90°	90°	-45°	0°	45°	90°	-45°	0°	45°	90°	-45°	0°	45°

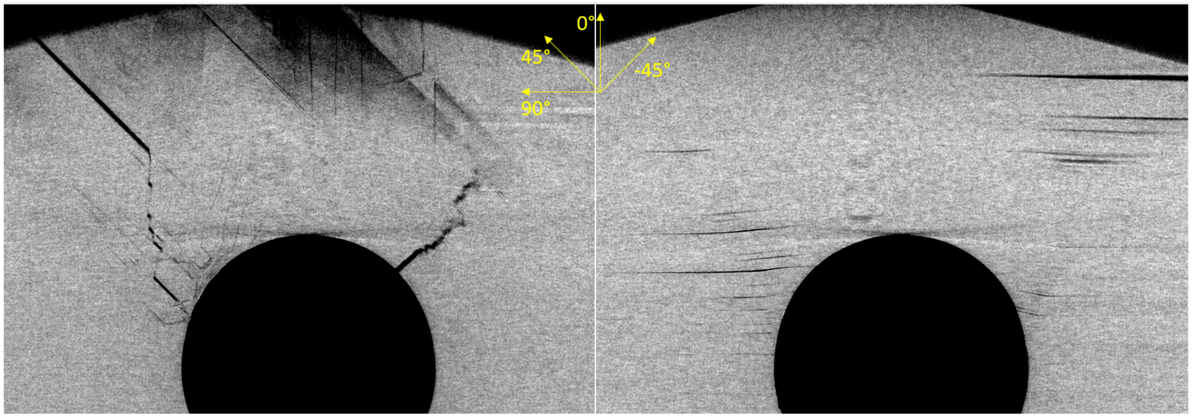

Figure 5.7: CT scan of Test 4. Left: Ply 5. Fiber and matrix cracking. Right: Plies 12 and 13, center of the laminate. Fiber bridging and matrix cracking.

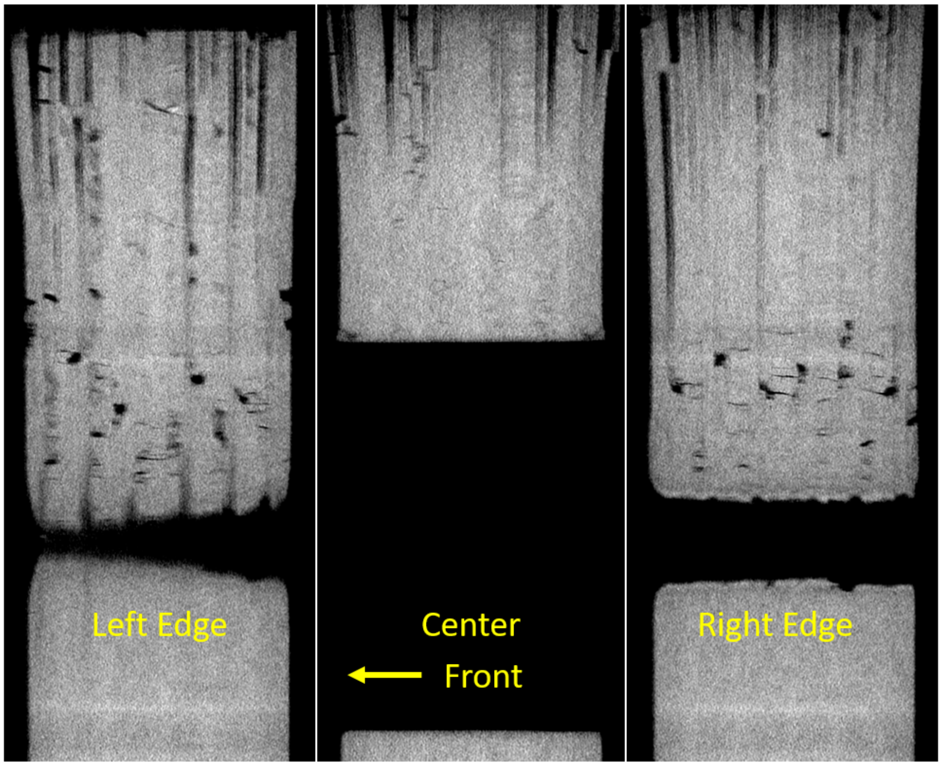

Figure 5.8: CT scan of Test 4. Side slices, loading direction: up. Clear delamination at specimen edge (top).

In Figure 5.9, CT images for Test 5, the test taken to 90% of the peak load are shown. The outer plies are shown in this Figure and a single line of matrix cracking is shown along the fiber direction, perpendicular to the hole in each image.

Ply	1	2	3	4	5	6	7	8	9	10	11	12	13	14	15	16	17	18	19	20	21	22	23	24
Orien.	45°	0°	-45°	90°	45°	0°	-45°	90°	45°	0°	-45°	90°	90°	-45°	0°	45°	90°	-45°	0°	45°	90°	-45°	0°	45°

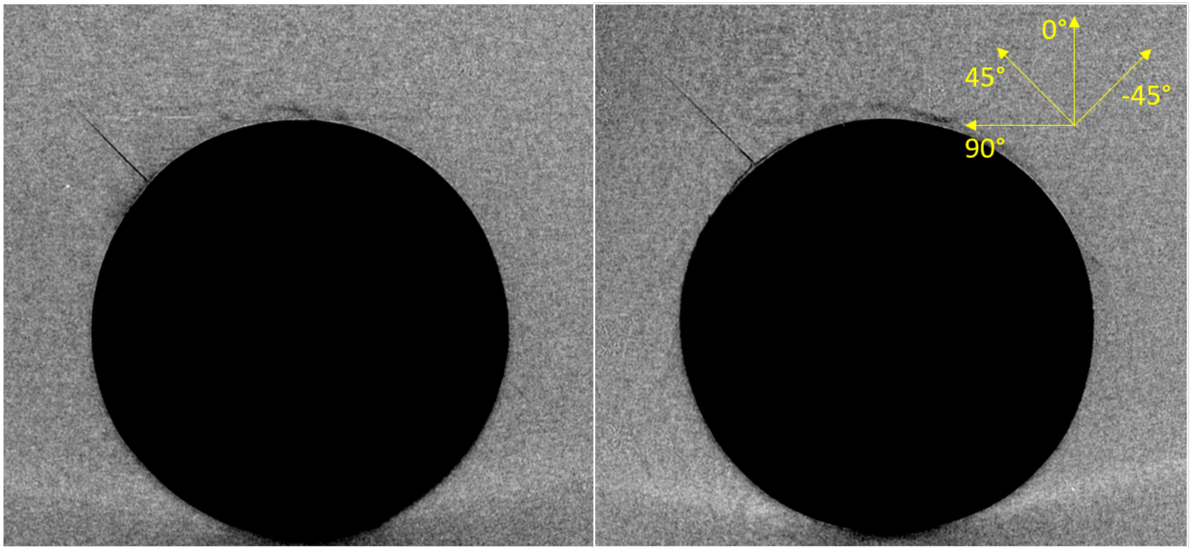

Figure 5.9: CT scan of Test 5. Left: Ply 1. Right: Plies 24. Both plies exhibit matrix cracking along the fiber direction, perpendicular to the hole.

5.3 $E = 2.0D$

5.3.1 Test Results

The test results for this eccentricity case are similar to the $E = 1.5D$ case in that there is a small plateau region at the peak of the load vs. displacement curve. However, in this sets of tests, the average peak load has risen from ≈ 5 kips to over 6 kips.

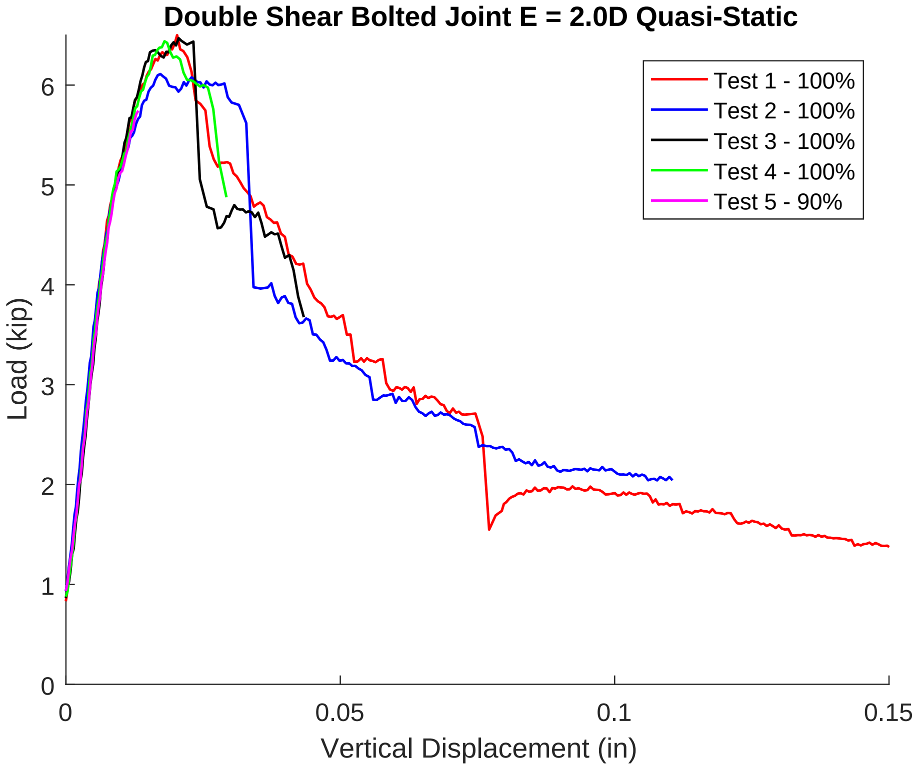

Figure 5.10: Double Shear Bolted Joint, E = 2.0D.

5.3.2 CT Scans

Figures 5.11 through 5.13 show CT images of test 4. Figure 5.11 shows, on the left, ply 1, and on the right, ply 2. Ply 1 (45) has widespread matrix cracking and fiber cracking running tangent to the hole on the left and perpendicular to the hole on the right. Ply 2 (0) has matrix cracking running tangent to the hole on both sides and fiber crushing above the hole, just past the washer footprint. Figure 5.12 shows, on the left, ply 4, and on the right, ply 5. The left image shows matrix cracking and, to the top left of the hole, fiber bridging in this 90 degree ply. In the right image, matrix cracking, fiber crushing aboe the washer footprint, and fiber cracking running perpendicular to the top right of the hole are present. Figure 5.13 shows side slices, at the center and just inside the left and right edge of the hole. Delamination is primarily seen in the back half of the specimen, towards the edge (top of images).

Ply	1	2	3	4	5	6	7	8	9	10	11	12	13	14	15	16	17	18	19	20	21	22	23	24
Orien.	45°	0°	-45°	90°	45°	0°	-45°	90°	45°	0°	-45°	90°	90°	-45°	0°	45°	90°	-45°	0°	45°	90°	-45°	0°	45°

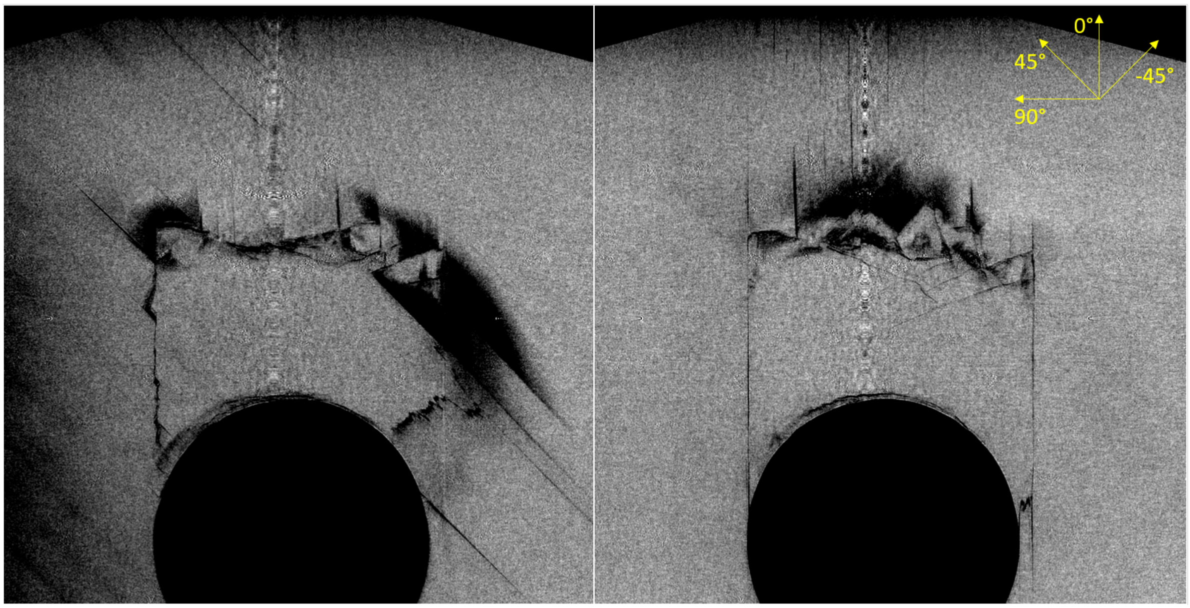

Figure 5.11: CT scan of Test 4. Left: Ply 1. Matrix cracking widespread and fiber cracking to top left and top right of hole. Right: Ply 2. Matrix cracking tangent to hole and fiber crushing above washer footprint.

Ply	1	2	3	4	5	6	7	8	9	10	11	12	13	14	15	16	17	18	19	20	21	22	23	24
Orien.	45°	0°	-45°	90°	45°	0°	-45°	90°	45°	0°	-45°	90°	90°	-45°	0°	45°	90°	-45°	0°	45°	90°	-45°	0°	45°

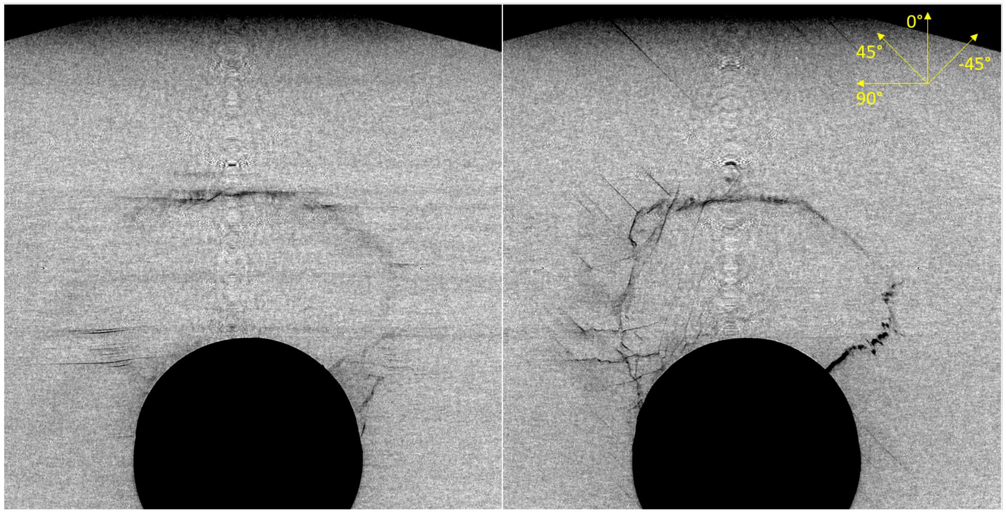

Figure 5.12: CT scan of Test 4. Left: Ply 4. Matrix cracking and fiber bridging (top left). Right: Ply 5. Matrix cracking, fiber crushing above washer footprint,and fiber cracking top right of hole.

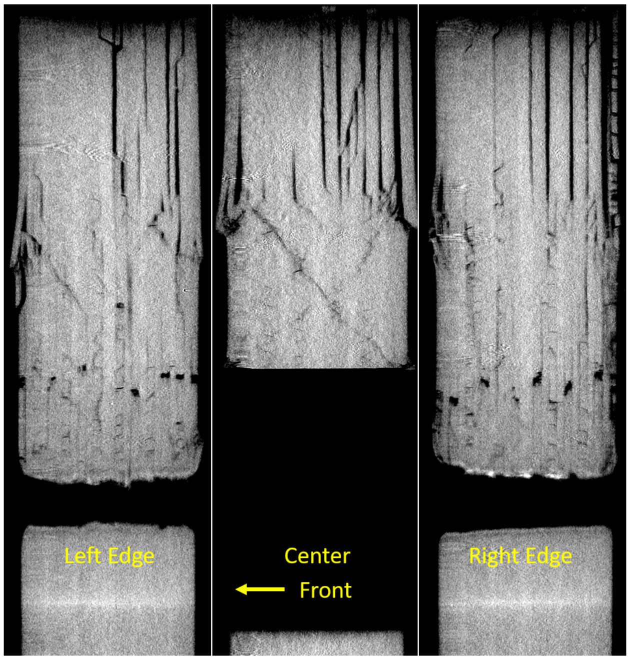

Figure 5.13: CT scan of Test 4. Side slices, loading direction: up. Clear delamination at specimen edge (top).

5.4 $E = 2.5D$

5.4.1 Test Results

The load vs. displacement curve for this test case resembles a behavior in between the $E = 1.5D$ and $E = 3.0D$ Window test cases. The load, again, peaks in a plateau region, drops slightly, and then appears to begin increasing its load-carrying ability. However, unlike the $E = 3.0D$ case, the post-peak load never exceeds the initial, peak failure load.

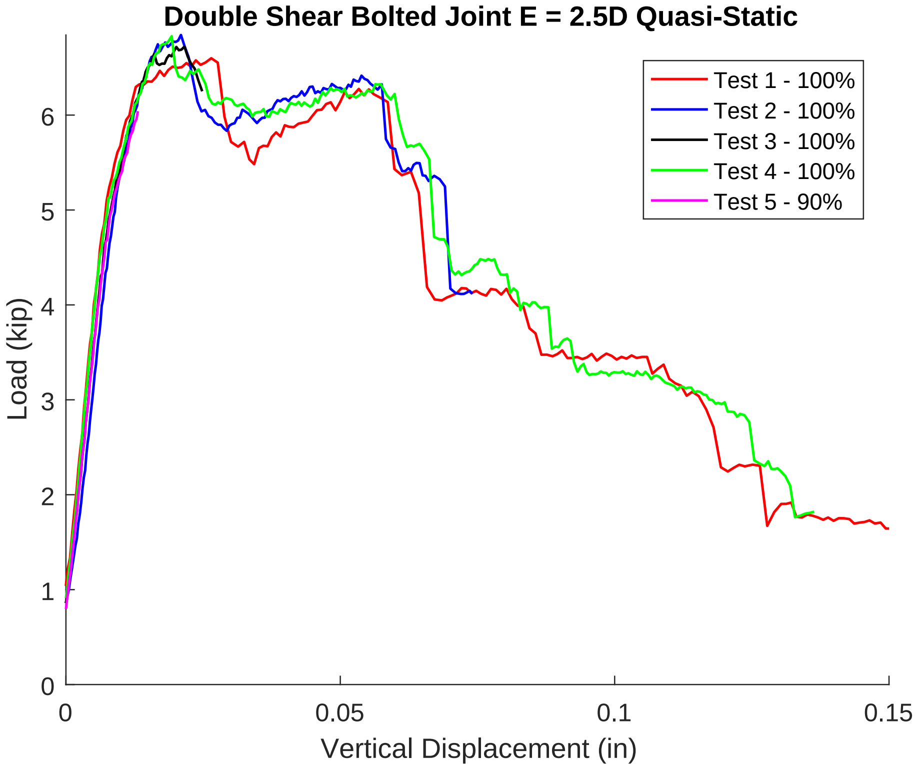

Figure 5.14: Double Shear Bolted Joint, E = 2.5D.

5.4.2 CT Scans

Figures 5.15 through 5.17 show CT images of test 3. Figure 5.15 shows, on the left, ply 1, and on the right, ply 2. Both images exhibit matrix cracking and fiber crushing above the washer footprint while the ply 1 contains significant fiber cracking. Figure 5.16 shows, on the left, ply 7, and on the right, plies 12 and 13, the center of the laminate. In ply 7 (-45), fiber cracking is clear, running perpendicular to the hole with some fiber crushing above washer footprint. In the right image, at the center of the laminate, matrix cracking and minor fiber bridging can be seen to either side of the hole. Figure 5.17 shows side slices, at the center and just inside the left and right edge of the hole. Delaminations can be seen occurring outside of the washer footprint.

Ply	1	2	3	4	5	6	7	8	9	10	11	12	13	14	15	16	17	18	19	20	21	22	23	24
Orien.	45°	0°	-45°	90°	45°	0°	-45°	90°	45°	0°	-45°	90°	90°	-45°	0°	45°	90°	-45°	0°	45°	90°	-45°	0°	45°

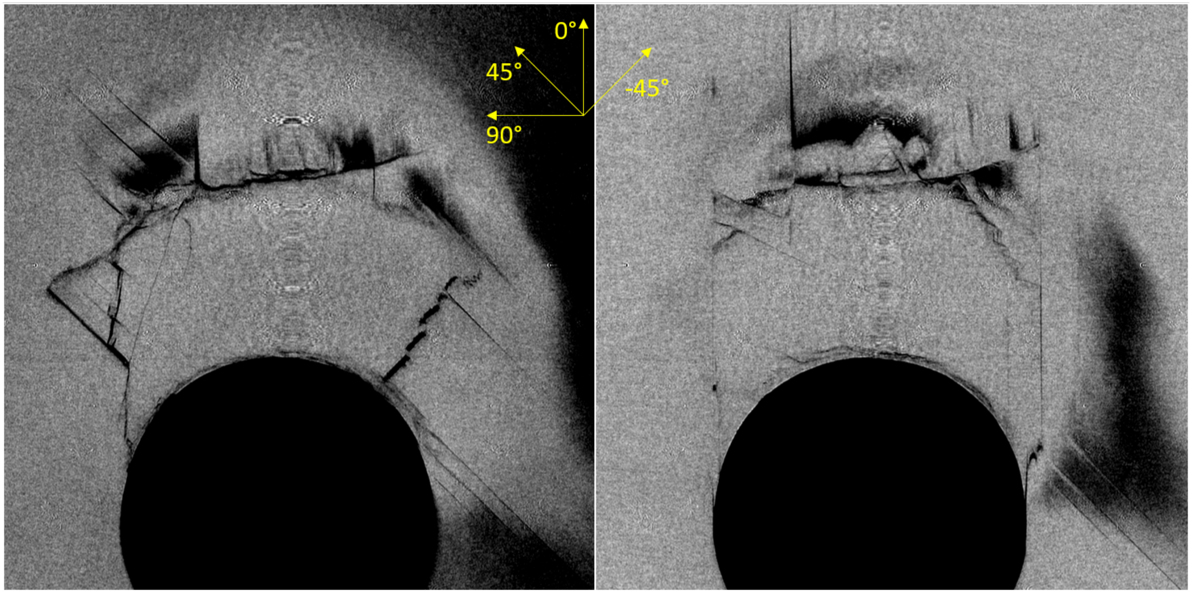

Figure 5.15: CT scan of Test 3. Left: Ply 1. Matrix cracking, fiber crushing above washer footprint,and fiber cracking top right of hole. Right: Ply 2. Matrix cracking tangent to hole and fiber crushing above washer footprint.

Ply	1	2	3	4	5	6	7	8	9	10	11	12	13	14	15	16	17	18	19	20	21	22	23	24
Orien.	45°	0°	-45°	90°	45°	0°	-45°	90°	45°	0°	-45°	90°	90°	-45°	0°	45°	90°	-45°	0°	45°	90°	-45°	0°	45°

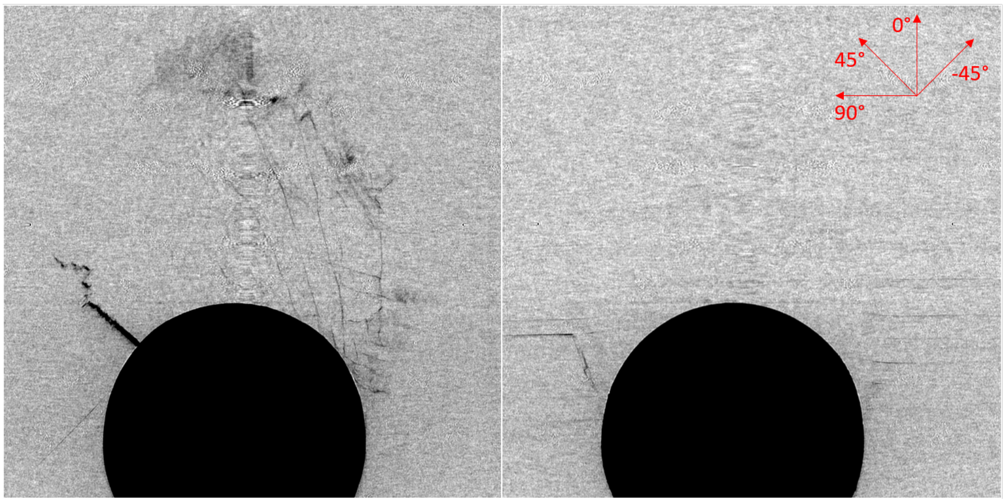

Figure 5.16: CT scan of Test 3. Left: Ply 7. Fiber cracking (top left). Right: Plies 12 and 13, center of laminate. Matrix cracking to left and right of hole.

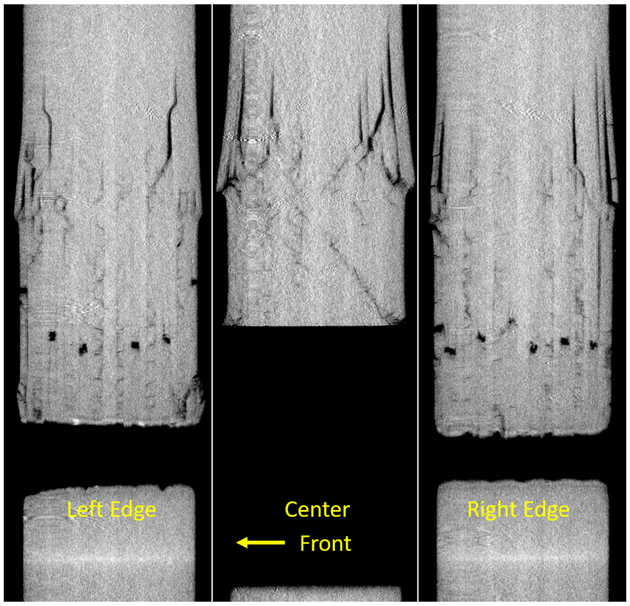

Figure 5.17: CT scan of Test 3. Side slices, loading direction: up. Delamination occurring outside of washer footprint.

5.5 $E = 3.0D$

5.5.1 Test Results

As with the $E = 1.5D$ case shown earlier, this test case strongly resembles the Window test of the same eccentricity. Again, the higher loads seen can be attributed the bolt being in pure shear and a stiffer out-of-plane constraint. The first peak of this test case also has a good resemblance to Crews' experiments shown in Figure 3 of his document. After this peak, however, the tests presented here are able to continue bearing load, whereas Crews' plot abruptly terminates. Further testing of higher eccentricity values, including the value Crews used ($E = 4.0D$), would need to be completed to explore a potential cause of this. [2]

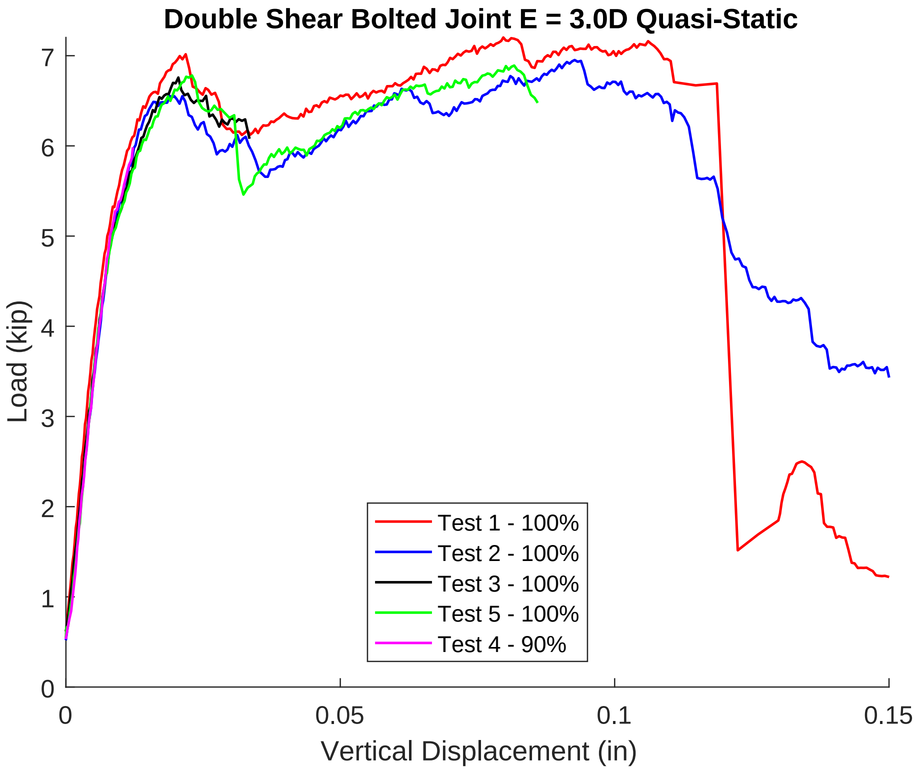

Figure 5.18: Double Shear Bolted Joint, E = 3.0D.

The peak region of the $E = 3.0D$ data and Figure 3 from Xiao's paper are shown below in Figure 5.19 and 5.20, respectively, for ease of comparison. The curves have some similarities, but the difference in displacement measuring techniques, bolt diameter, and specimen thickness is likely having an effect on the different behaviors. Xiao's work clearly shows several distinct steps as the load approaches ultimate bearing strength, whereas my work has a smoother climb to the initial peak. This is possibly due to the displacement measurement techniques; Xiao used an electro-optical extensometer with a, presumably, higher data collection frequency. [5]

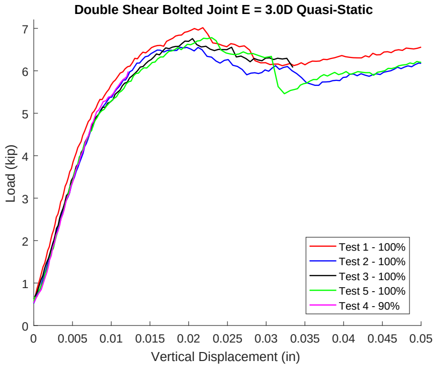

Figure 5.19: Double Shear Bolted Joint, E = 3.0D, peak region.

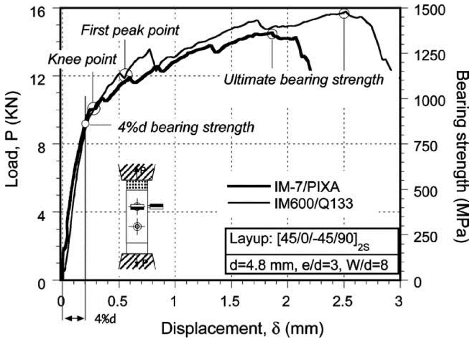

Fig. 3. Typical load–displacement curves for IM-7/PIXA and IM600/Q133 specimens.

Figure 5.20: Figure 3 from Xiao's paper. Load vs. displacement for two material systems.

5.5.2 CT Scans

Figures 5.21 through 5.23 show CT images of test 3. Figure 5.21 shows, on the left, ply 2, and on the right, ply 3. Matrix cracking tangent to the hole and fiber crushing above the washer footprint are present in the left image. A small amount of fiber cracking can also be seen either side of the hole. In ply 2 (-45), matrix cracking, fiber crushing, and fiber cracking can all be seen clearly. Figure 5.22 shows two 90 degree plies - on the left, ply 4, and on the right ply 8. Both plies exhibit fiber bridging to either side of the hole and fiber cracking in the center. These features are more prominent in the ply closer to the outside of the laminate. Figure 5.23 shows side slices, at the center and just inside the left and right edge of the hole. Delaminations can be seen occurring outside of the washer footprint. Good correlation is seen when comparing the center image in the side slices to Xiao's work seen in Figures 5.24 and 5.25. The X-pattern of through-thickness shear occurring under the washer footprint can be seen quite clearly in the center image of Figure 5.23.

Ply	1	2	3	4	5	6	7	8	9	10	11	12	13	14	15	16	17	18	19	20	21	22	23	24
Orien.	45°	0°	-45°	90°	45°	0°	-45°	90°	45°	0°	-45°	90°	90°	-45°	0°	45°	90°	-45°	0°	45°	90°	-45°	0°	45°

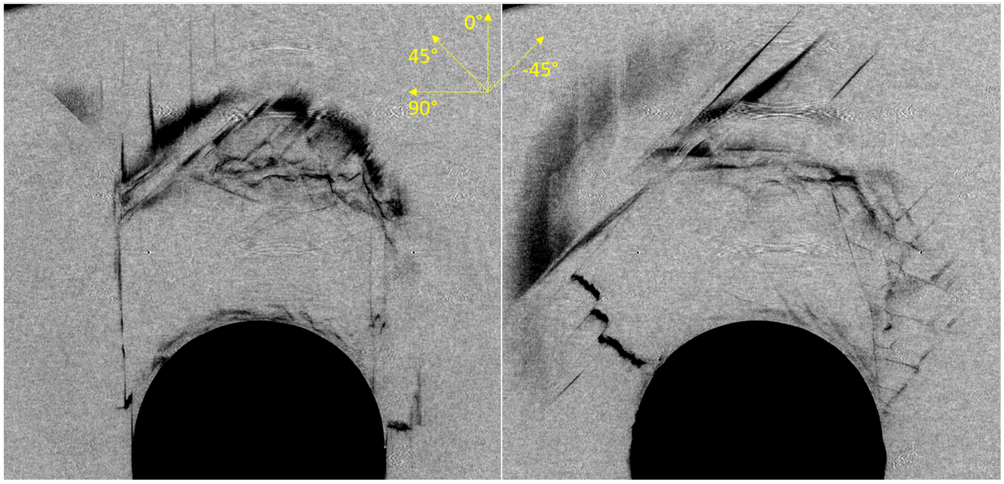

Figure 5.21: CT scan of Test 3. Left: Ply 2. Matrix cracking tangent to hole and fiber crushing above washer footprint. Small amount of fiber cracking to right of hole. Right: Ply 3. Matrix cracking, fiber crushing above washer footprint, fiber cracking to top left of hole.

Ply	1	2	3	4	5	6	7	8	9	10	11	12	13	14	15	16	17	18	19	20	21	22	23	24
Orien.	45°	0°	-45°	90°	45°	0°	-45°	90°	45°	0°	-45°	90°	90°	-45°	0°	45°	90°	-45°	0°	45°	90°	-45°	0°	45°

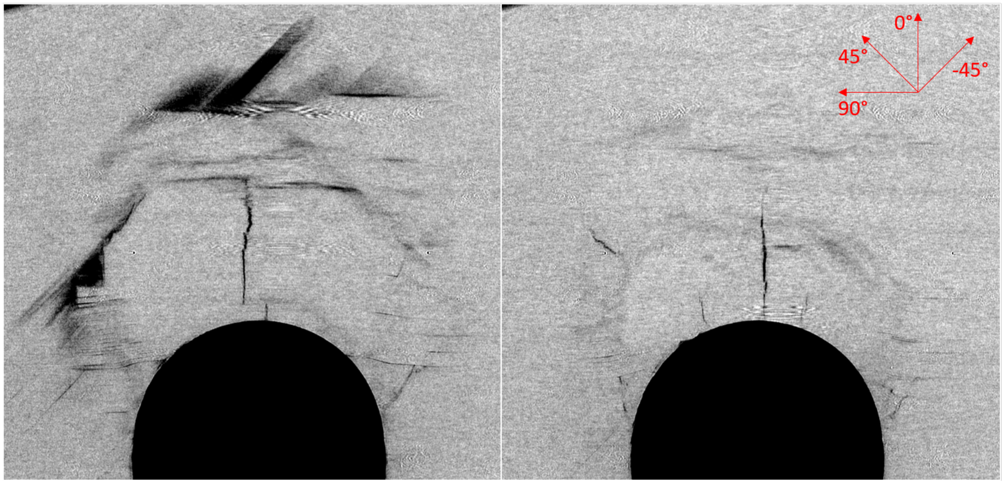

Figure 5.22: CT scan of Test 3. Left: Ply 4. Right: Ply 8. Fiber bridging to left and right of hole, fiber cracking in center for both plies. Features more apparent in ply 4.

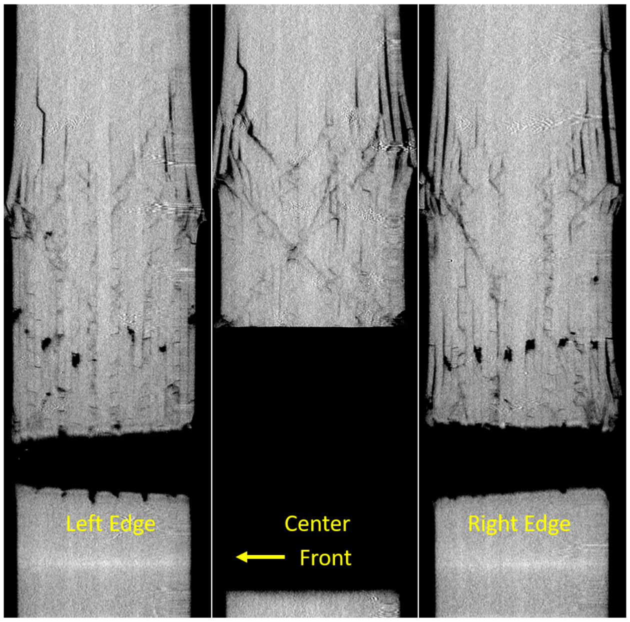

Figure 5.23: CT scan of Test 3. Side slices, loading direction: up. Delamination occurring outside of washer footprint.

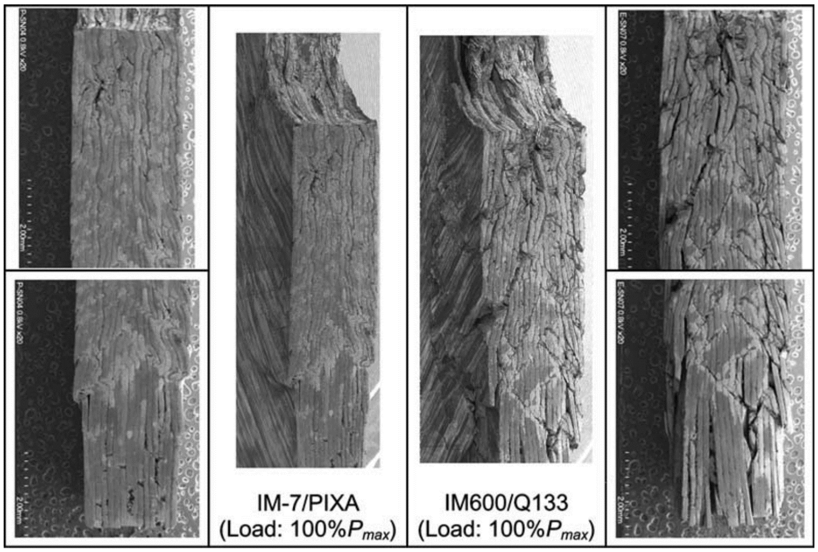

Fig. 10. SEM photographs of through-thickness bearing damage, tested at 100% of maximum load.

Figure 5.24: Figure 10 from Xiao. SEM photographs to compare to side slices seen in Figure 5.23. Note: loading direction: down.

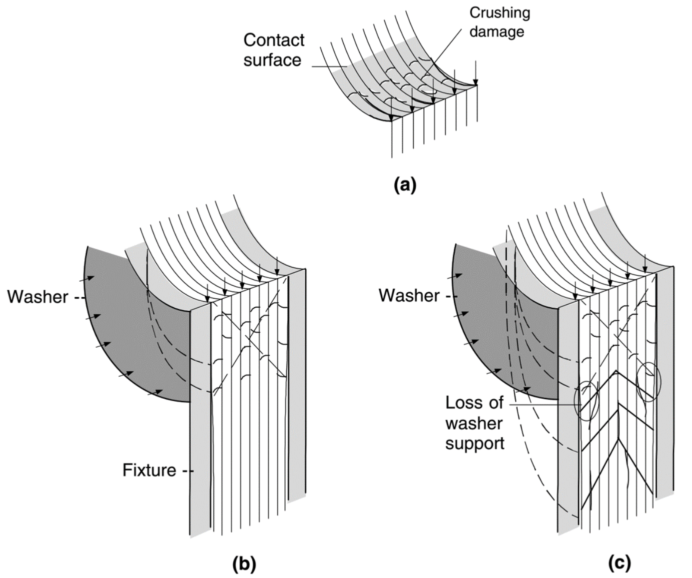

Fig. 11. Schematic descriptions of the bearing failure mechanisms: (a) crushing damage; (b) damage within lateral constraint (inside-washer region); (c) damage without lateral constraint (outside-washer region).

Figure 5.25: Figure 11 from Xiao. Schematic of failure mechanisms to compare to side slices seen in Figure 5.23. Note: loading direction: down.

5.6 *Comparison of Eccentricities*

Figures 5.26 and 5.27 show a comparison of all Double Shear Bolted Joint tests conducted organized by eccentricity. All of the cases except for the $E = 1.5D$ case reach a similar peak load value before the initial failure occurs. The reason for this appears to be answered in the CT scan images shown previously. The side slices for $E = 1.5D$ show significant amounts of delamination spreading to the very top of the specimen, even causing the top edge to flare outwards slightly. The $E = 2.0D$ case also exhibits delamination reaching the top of specimen, but it is not as widespread as the $E = 1.5D$ case. The remaining two cases exhibit much more contained delamination. By way of inspection of all CT images presented, it is clear that all eccentricity cases experience the combination of shearout and bearing failures seen in Crews' experiments.

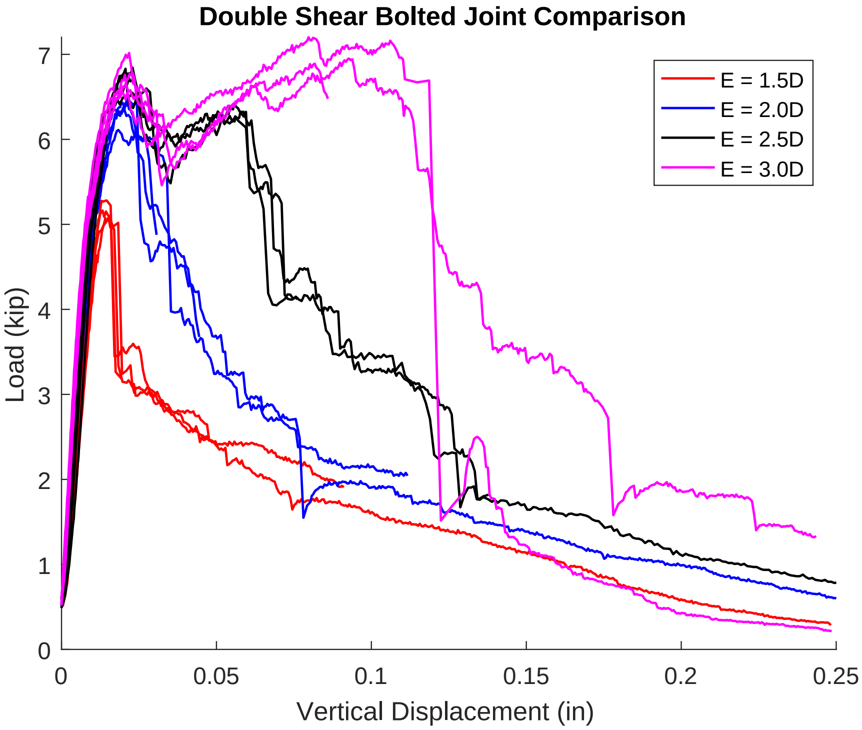

Figure 5.26: Comparison of eccentricity in Double Shear Bolted Joint tests. Full extent of data shown.

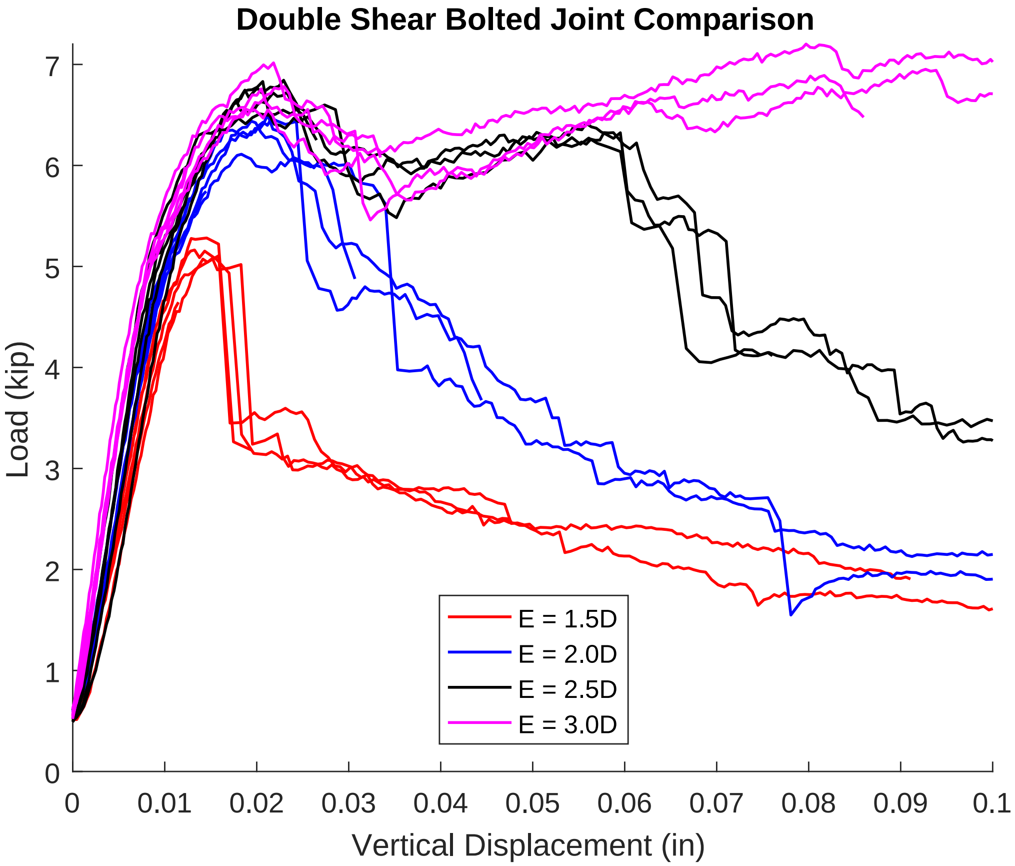

Figure 5.27: Comparison of eccentricity in Double Shear Bolted Joint tests. Peak region shown.

Chapter 6

COMPARISON OF THREE TEST SETUPS

This chapter simply presents three plots containing data from all three test setups. First, all data; second, data for $E = 1.5D$ only; and third, data for $E = 3.0D$ only.

6.1 Test Results - All Cases

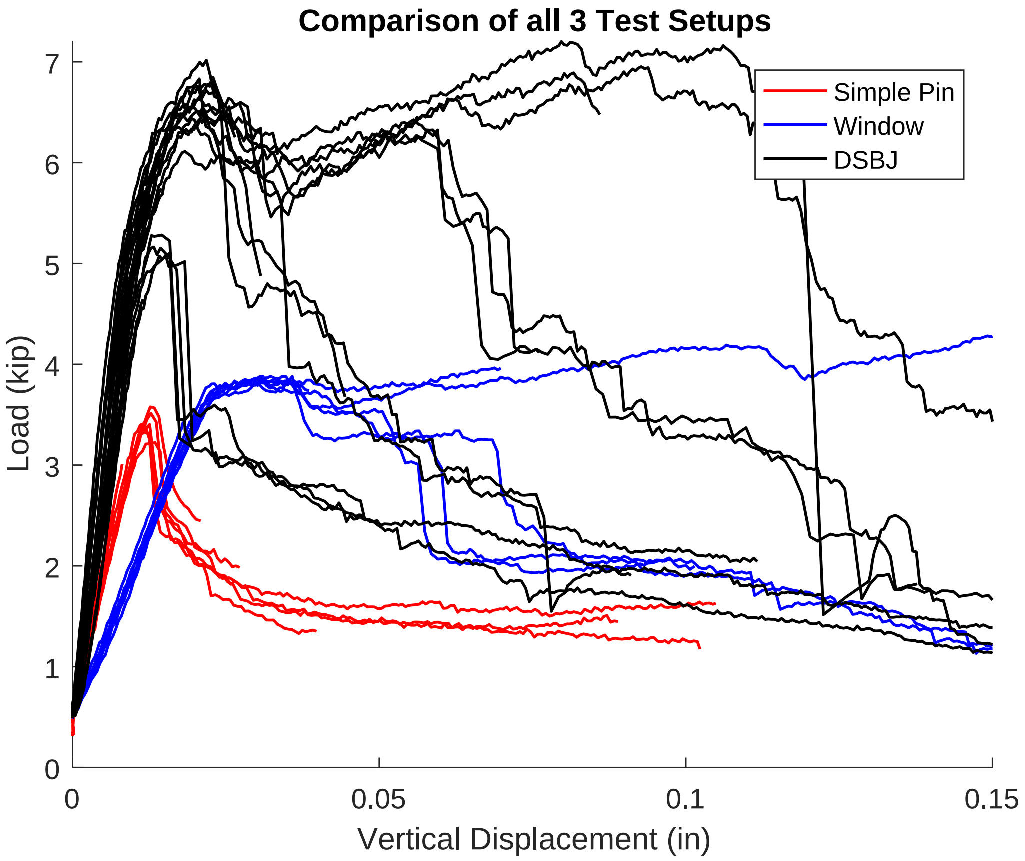

Figure 6.1: All test data. Organized by test setup.

6.2 Test Results - E = 1.5D Only

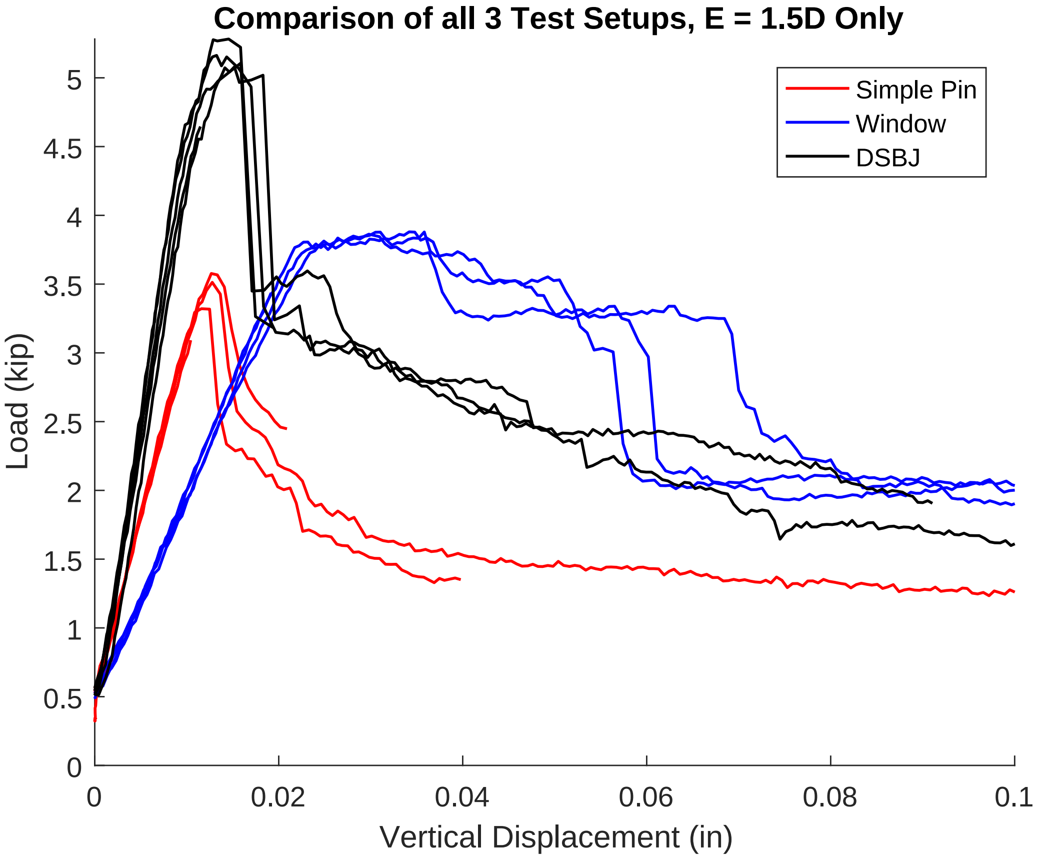

Figure 6.2: All test data for $E = 1.5D$. Organized by test setup.

6.3 Test Results - E = 3.0D Only

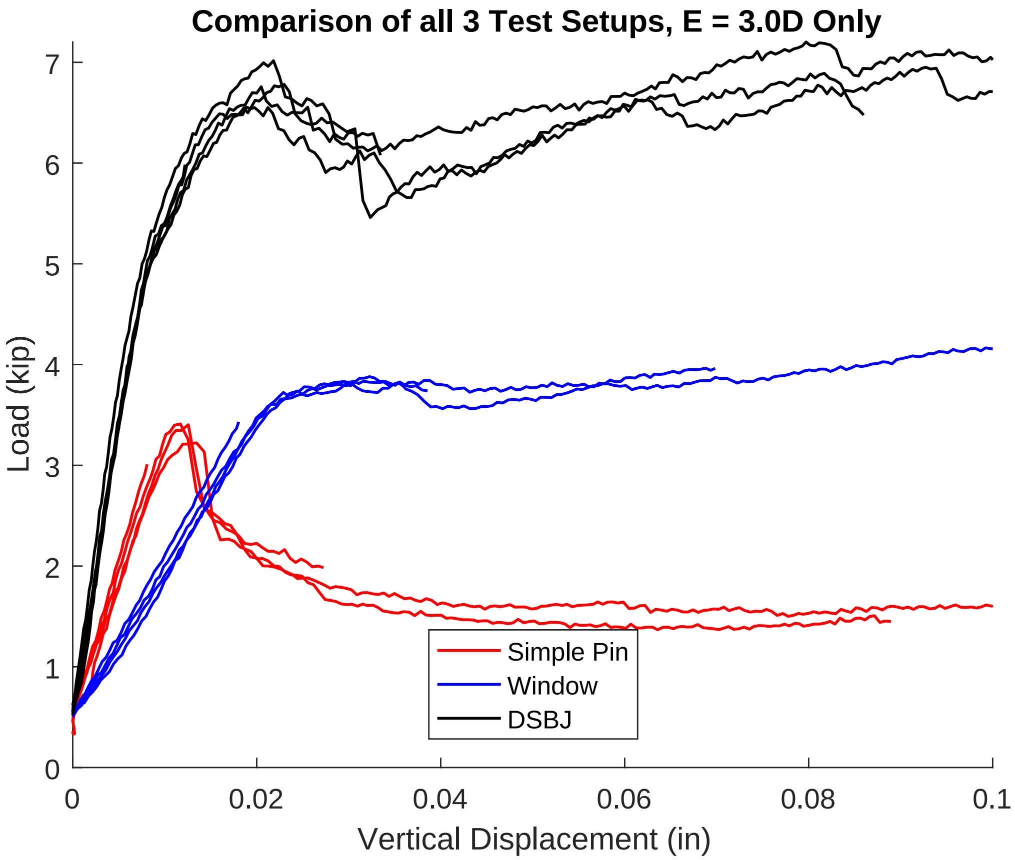

Figure 6.3: All test data for $E = 3.0D$. Organized by test setup.

Chapter 7

CONCLUSION

For this Masters thesis, pinned and bolted joint experiments were performed on a composite laminate for a single material system in order to gather data and examine the failure mechanisms using two novel test setups and one standard fixture. The data collected consists of load vs. displacement plots, far-field strain plots using DIC, and X-ray micro CT scans. All of these methods aided in the characterization of the failures seen. Upon completion of this work, the following conclusions are made:

1. A simply pinned joint, with no out-of-plane constraint/clamp-up, will fail at the same average load regardless of eccentricity.

2. Even a relatively soft out-of-plane constraint/clamp-up will change the failure mode from simple pin bearing to a combination of shearout and pin bearing while also increasing the initial failure load.

3. In agreement with Crews, increasing the clamp-up pressure through the bolt's torque can increase the joint's initial failure load significantly.

4. The eccentricity of the joint primarily impacts the post-peak behavior. The larger the eccentricity, the longer the joint retains the ability to carry load.

5. In the Double Shear Bolted Joint case of $E = 1.5D$, the eccentricity also plays a part in the maximum failure load. This lesser amount of material between the hole and the specimen edge compared to the other cases allows delaminations to spread more easily to the edge of the specimen, resulting in an earlier failure.

6. For the safest joints, clamp-up and an eccentricity of $E = 3.0D$ is paramount. In both the Window and DSBJ tests, this case exhibited a clear ability to continue holding a high load after the initial joint failure.

Chapter 8

FUTURE WORK

Several ideas for improving this experimental work arose while performing the tests and analyzing the data. Unfortunately, these ideas were unable to be incorporated due to time and material constraints. These ideas will be detailed here.

The first idea came to me when comparing the Simple Pin Loading tests to the Window tests. The different slopes in the load vs. displacement curves was initially very galling. The primary function of this work was to expand on Crews' findings, particularly Figure 3 in his report, and have my own, similar comparisons. While the curves can still be compared, along with the DIC and CT scans, in the future it would make more sense to keep the pin supports a fixed distance for both the Simple Pin Loading and the Window tests. This way, the part the pin plays in the stiffness of the joint would be equivalent for both setups.

The next idea was triggered twice during testing. The first time was during the initial Window test using the 17-4PH Stainless Steel pin when it bent excessively. The second instance was during Test 1 of the $E = 3.0D$ Window test. After the initial failure, the load slowly continued to increase resulting in a catastrophic failure of the Hardened Steel Pin. While I was able to get some useful data, it would be interesting to see the full extent of this test and how it compared to the Double Shear Bolted Joint tests of the same eccentricity. The solutions are obvious in both cases: decrease the effective pin length and, therefore, the bending stress seen in the pin. The only way of doing this is to decrease the thickness of the transparent washers and windows, thus bringing the steel support windows closer together. Unfortunately, due to time constraints, I elected to use the available Plexiglas material we had in our lab and, subsequently, designed my fixture to fit that. In the future, I would research and acquire thinner sheets of transparent, strong material in order to decrease the effective pin length without giving up the out-of-plane constraint.

The location of the side speckle pattern used for the displacement DIC calculations is the subject of my next idea. In the Simple Pin Loading and Window tests I chose to place this speckle pattern lower on the specimen such that it was below the fixture. This was done to ensure that there was enough light and that the image was not too dark to be useful. The problem with this method is that the displacement measured is not of the pin/hole, but of an arbitrary point lower on the specimen, thus the strain of the composite in between is not taken into account. In future tests I would paint this speckle pattern identical to the Double Shear Bolted Joint tests and add lighting and adjust the camera settings to get an usable image.

Finally, my last idea for future work is to add the $E = 2.0D$ and $E = 2.5D$ eccentricity cases to the Window tests to see if they mimic the behavior seen in the Double Shear Bolted Joint tests. Because there was no distinct difference in failure for the eccentricities used in the Simple Pin Loading tests, I do not believe it is necessary to add these cases in this setup.

BIBLIOGRAPHY

[1] T.C. Chu, W.F. Ranson, M.A. Sutton, and W.H. Peters. Applications of digital-image-correlation techniques to experimental mechanics. *Experimental Mechanics*, September 1985.

[2] John H. Jr. Crews. Bolt-bearing fatigue of a graphite/epoxy laminate. Technical Memorandum 81851, NASA, July 1980.

[3] Samantha H. Daly. Digital image correlation in experimental mechanics for aerospace materials and structures. In *Encyclopedia of Aerospace Engineering*. John Wiley and Sons, 2010.

[4] Hseng-Ji Huang and Anthony M. Waas. Improved speckle method for measuring in-plane displacement and strain fields. *Optical Engineering*, 46, May 2007.

[5] Yi Xiao and Takashi Ishikawa. Bearing strength and failure behavior of bolted composite joints (part i: Experimental investigation). *Composites Science and Technology*, 2005.

Appendix A

DIGITAL IMAGE CORRELATION

Digital Image Correlation (DIC) is a non-contact method of measuring full-field displacement. Using optics and either cross-correlation or a least-squares function, a random pattern on the surface of a specimen can be tracked in order to determine the surface deformation. This method compares the grayscale values of two images - the undeformed, reference, and the deformed - to calculate a mapping of the surface deformation [3]. As seen in this document the random pattern on the surface is a black and white speckle pattern. A thin coat of white paint is sprayed on the area of interest followed by a misting of black paint. Depending on the size of the specimen and the desired fidelity of the measurements, the black mist can be done with general spray paint (coarse) or an airbrush (fine).

An improved method was proposed by Huang and Waas using the fast Fourier transform. Their method deals with the speckle information in the frequency domain. Provided the peak of the Fourier spectrum is located with good accuracy, this method can measure displacements with an accuracy up to 2 μm [4]. DIC methods can accurately track and measure the movement of objects in many applications. The publication by Chu et al. presents several examples of experiments utilizing DIC. These include uniform translation, rigid-body rotation, constant angular velocity, and uniform finite strain. In the uniform finite strain tests presented, the error in calculating the deformation gradient was less than 10 percent; this value would likely be improved with the use of higher resolution images. [1]

Appendix B

LOAD VS. DISPLACEMENT DATA PROCESSING

The load vs. displacement data used to generate the plots in this thesis are comprised of two sources of data. First, the load data is outputted to a text file by the load frame's control software. This file contains three columns: Time, load, and actuator displacement. The data is written at a frequency of 1000 points per second. Second, the displacement data is gathered from the side-facing camera images via DIC. The camera is set to take a picture once per second and is simply synchronized with the start of the test. Prior to the DIC calculations, the images are cropped and every other image is used; this results in a displacement data point for every other second of the test. This is done primarily to speed up the DIC calculations; some tests run for over 10 minutes and the resulting large collection of images can crash the DIC software.

With these two files - the load file and the displacement file - a simple Matlab script (CompileData.m) loads in the data and creates a simple, two-column matrix of the load and data measured at a frequency of one point for every two seconds. This matrix is output to its own data file.

As the tests are completed, the data files are gathered and plotted together to form the various load vs. displacement plots shown in this document. Minimal processing is done and can be seen in the second Matlab script (PlotData.m). The primary adjustment done to the data is to shift the curves to the left so they lie on top of one another. This only eliminates any settling in the fixture that occurs at the beginning of a test. No change to the stiffness is done. The secondary adjustment is utilizing the smooth function on the displacement data. Figure B.1 shows a plot that has been adjusted, while Figure B.2 shows one without adjustment. Note the shifting in initial ramps.

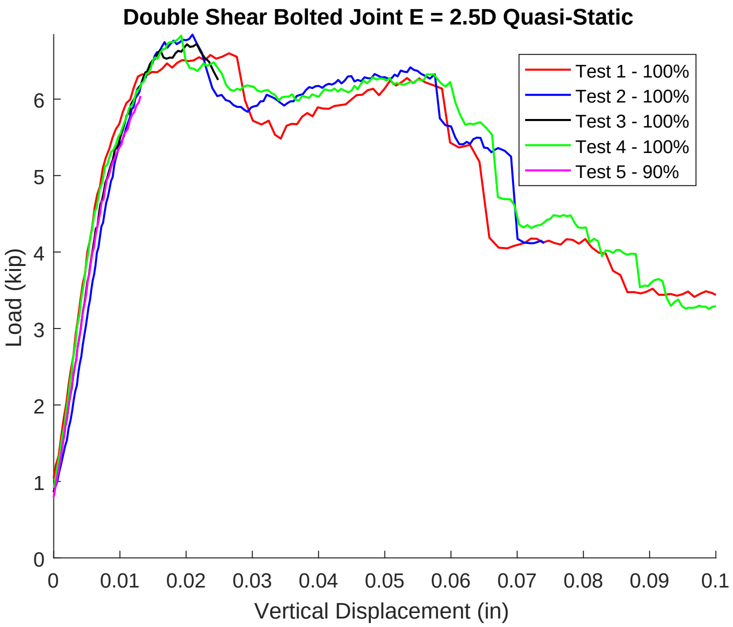

Figure B.1: Example of load vs. displacement curve with adjustments to data.

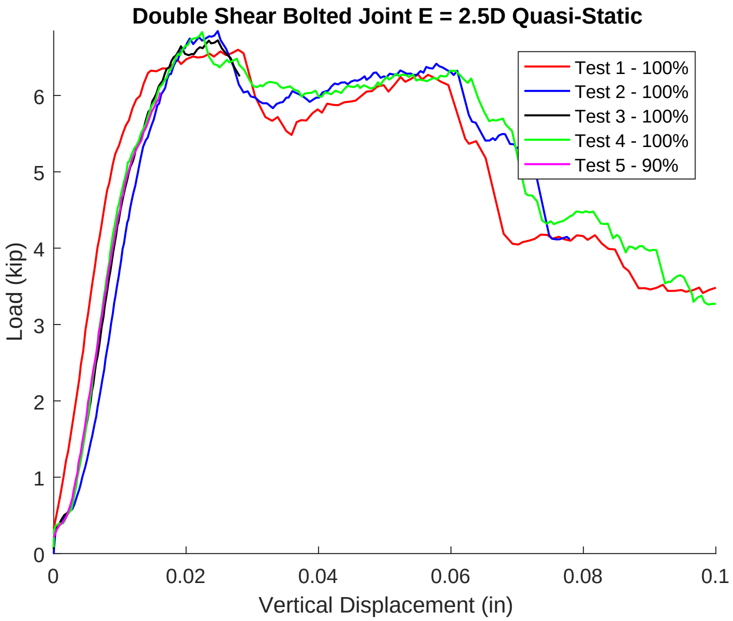

Figure B.2: Example of load vs. displacement curve with no adjustments to data.

```matlab
%%CompileData.m

%Test Inputs
Hz = 1000;    %Load frame data recording freq
int = 2;    %DIC camera interval
t_limit = 400; %Last time recorded in load data
N = floor(t_limit/int) + 1;

%Input Data Start Locations (0 = first row/col)
LoadR = 20;
LoadC = 1;
DispR = 3;
DispC = 1;

%Read in test data files
LoadRaw = dlmread('Test1_Load.dat','\t', LoadR, LoadC); %(kip)
LoadRaw = -1.*LoadRaw(:,1); %Change Load to positive
DispRaw = dlmread('Test1_SideDisp.dat',',', DispR, DispC); %From DIC (mm)
DispRaw = (1/25.4).*DispRaw; %(inch)

%Select Load Data corresponding to DIC Disp Data
Step = Hz*int;
Load = zeros(N,1);
for i = 1:N
    j = 1 + (i-1)*(Step);
    Load(i) = LoadRaw(j);
end
Disp = DispRaw(1:N,1);

%Write data to new file
Data = [Load, Disp];
dlmwrite('Test1_Data.dat', Data, 'delimiter', '\t', 'precision', 4)
```

```
%%PlotData.m

%Files to load
Files = {'Test1_Data.dat', 'Test2_Data.dat', 'Test3_Data.dat',...
    'Test4_Data.dat', 'Test5_Data.dat'};

N = length(Files);

figure(1)
hold on
colors = {'r','b','k','g','m','m','y'};

for i = 1:N

    %Read in test data files
    data = dlmread(Files{i},'\t');
    load = data(:,1);
    disp = data(:,2);

    %Find adjustment point
    zero_pt = find(load > 0.8,1);
    adj = disp(zero_pt);

    %Apply adjustment
    disp = disp - adj;

    disp = smooth(disp);

    plot(disp, load,'LineWidth',1, 'Color', colors{i})
end
```

Appendix C

CT SCANNER SETTINGS

The X-ray micro CT scanner used for the images shown in this document is a NSI X5000. The X5000 is a fully-enclosed system with a movable source (up/down), detector (all 3 translation axes), and turntable (5 axes). Figures C.1 and C.2 show the inside and outside of the machine.

Figure C.1: Outside the NSI X5000.

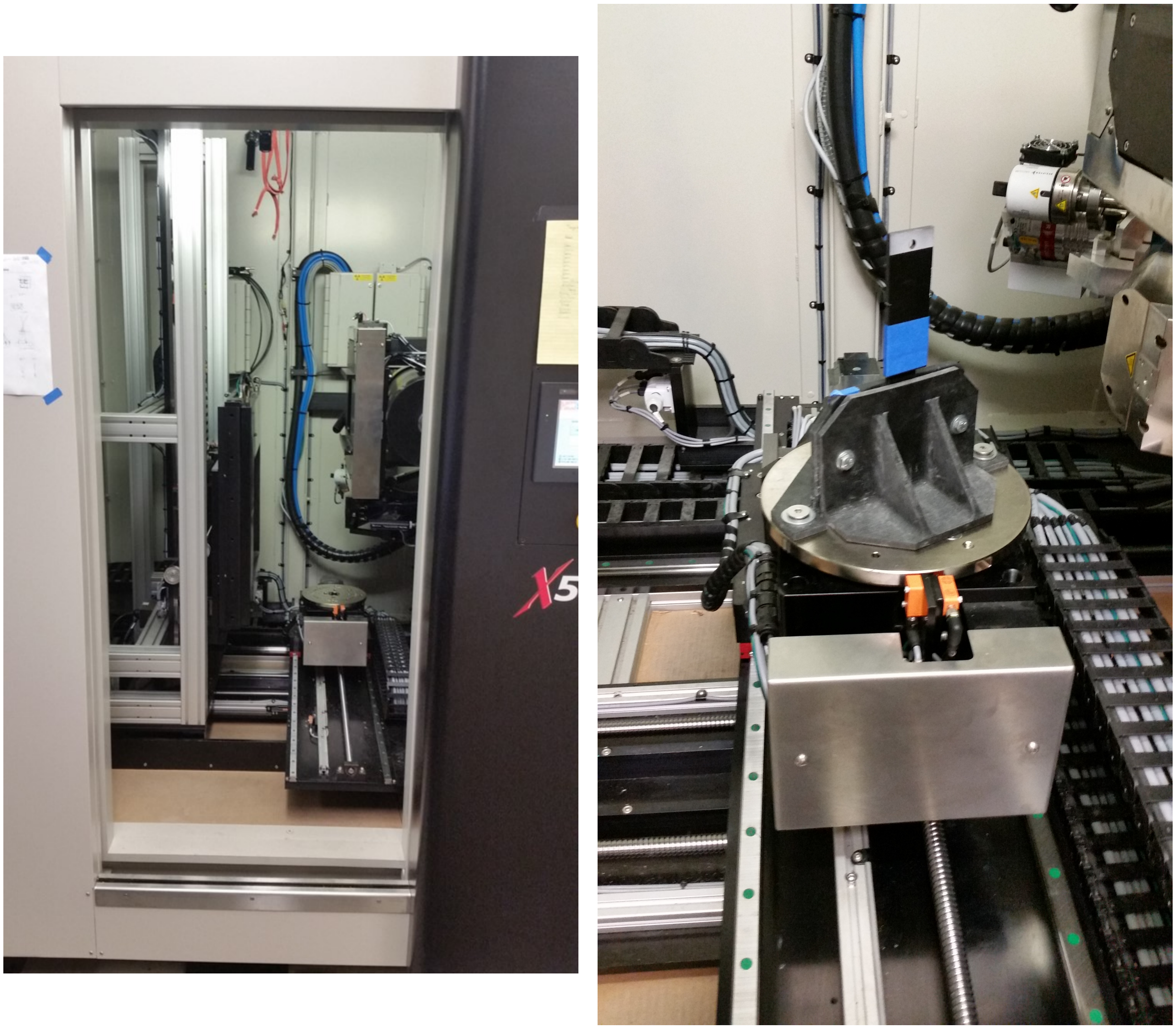

Figure C.2: Left: Detector panel and turntable in position. Right: Specimen clamped in fixture mounted to turntable.

This machine collects radiographs as the specimen rotates a full 360 degrees. The NSI software is then able to reconstruct a 3D solid from this collection of images. The user then has an option to export slices through the X, Y, and Z directions as seen in this document. The average resolution obtained was 10 microns. Figure C.3 shows a couple of sample radiographs.

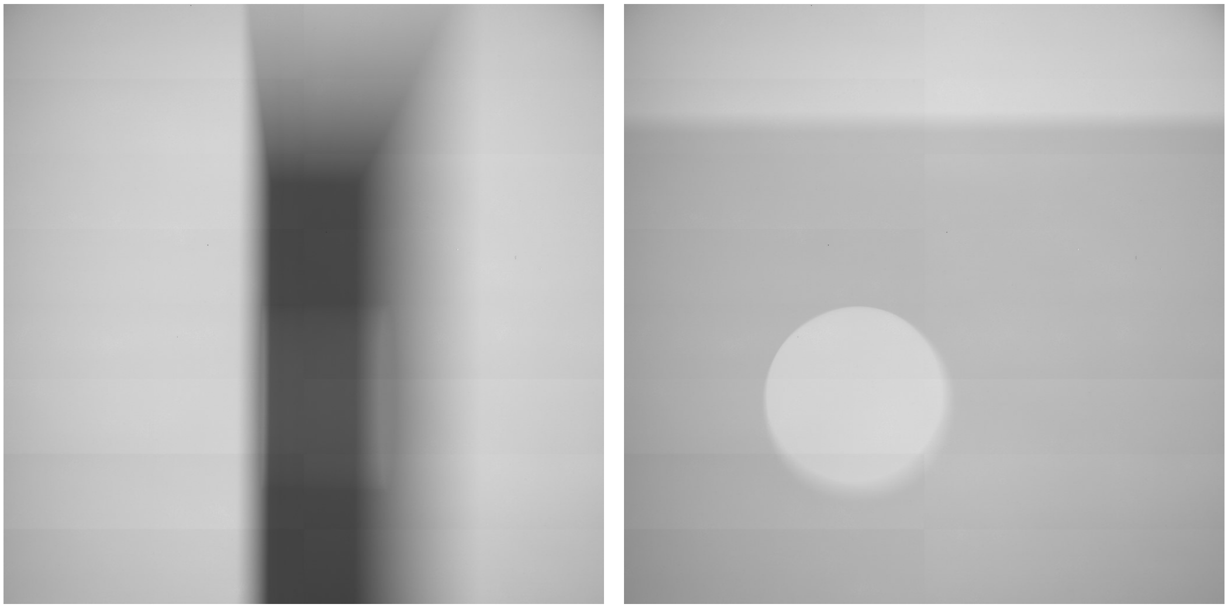

Figure C.3: Sample radiographs.